Title
Enhanced Seismic Resiliency for Buildings via Base Isolation

Author
Chen, Michelle Carolyn

Publication Date
2018

UNIVERSITY OF CALIFORNIA, SAN DIEGO

Enhanced Seismic Resiliency for Buildings via Base Isolation

A Dissertation submitted in partial satisfaction

of the requirements for the degree

Doctor of Philosophy

in

Structural Engineering

by

Michelle Carolyn Chen

Committee in charge:

José I. Restrepo, Chair
Gianmario Benzoni
Joel P. Conte
David T. Sandwell
Michael D. Todd
Chia-Ming Uang

2018

The dissertation of Michelle Carolyn Chen is approved, and it is acceptable in quality and form for publication on microfilm and electronically:

Chair

University of California, San Diego

2018

DEDICATION

To my family, Alexander and Meadow;

and to my parents and brother, Ann, Kwan-Shei and Christopher Chen.

EPIGRAPH

Nothing in life is to be feared, it is only to be understood.

Now is the time to understand more, so that we may fear less.

Marie Curie

TABLE OF CONTENTS

LIST OF TABLES

LIST OF FIGURES

ACKNOWLEDGEMENTS

I would like to thank everyone who has supported and encouraged me throughout this journey; those who have selflessly shared their time and knowledge and who always had my best interests in mind. My teachers and colleagues who went above and beyond to collaborate with me and offer their expertise: Professor Conte and Gianmario Benzoni, thank you for your valuable insight throughout my Ph.D. process. My dissertation committee: Dr. Benzoni, Professor Conte, Professor Sandwell, Professor Todd, and Dr. Uang - I appreciate your time and help through this final stage. My colleagues who collaborated with me for research and in teaching assistance, especially Rodrigo Astroza, Elide Pantoli, Xiang Wang, Carlos Blandon, Rodrigo Carreño, Arpit Nema and Koorosh Lotfizadeh - I am grateful to have had you all as coworkers and as friends.

I would like to acknowledge the staff at ESEC, Powell Labs and SRMD for your hard work and help on my experiments; I was always able to count on you guys. Thank you to the SE department staff for helping me over the years, who will forever be some of Meadow's favorite people, and especially for Lindsay, Yvonne, Julie and Natalie, who always brighten my day. I would like to thank the organizations that provided financial support for me during my Ph.D., especially IGERT and the ARCS foundation, through which I have gained many relationships throughout the years. I'm grateful for those who have been sources of support over the years: Meadow, Cybelle, Amie, Anna, Genaro, Elan, Lynsay, my grandma Louise, Philippe and Alicemarie, Richard, Michelle and Aaron, Maya, Louise and Chris, Susy and Maurizio, Val, the Chen uncles, aunts and cousins, Becky and Rick, Lauren and Adam, Taylor, Georgia, Paula and Tom, Patrick and Kyra.

I would like to extend my deepest note of thanks and gratitude to my Ph.D. advisor, José Restrepo. Working with you and learning from you has been a more rewarding experience than I could have imagined. Your patience, dedication and guidance inspired me to reach my full potential. And thanks to you I am now clued up on how to make bets.

I am eternally grateful for my parents, Ann and Kwan, and my older brother, Chris, who motivated me and gave me the opportunity to pursue my goals with their unconditional love and support.

Finally, to my best friend and partner, Alexander - your unwavering encouragement and support at every step are what got me through this journey, and I'm excited for what will come next.

Parts of the dissertation have been published in peer reviewed journals. The author of the dissertation is the principal researcher and author of all published papers and papers submitted/prepared for submission included in the dissertation.

Chapter 2, with the exception of Appendix A, is published in:

- **Chen, M.**, Pantoli, E., Wang, X., Astroza, R., Ebrahimian, H., Hutchinson, T., Conte, J., Restrepo, J., Marin, C., Walsh, K., Bachman, R., Hoehler, M., Englekirk, R., & Faghihi, M. (2016). Full-scale structural and nonstructural building system performance during earthquakes: part I – specimen description, test protocol and structural response. *Earthquake Spectra, 32*(2), 737-770.

Chapter 3, with the exception of Appendix B, is published in:

- **Chen, M.**, Astroza, R., Restrepo, J. I., Conte, J. P., Hutchinson, T., & Bock, Y. (2017). Predominant period and equivalent viscous damping ratio identification for a full-scale building shake table test. *Earthquake Engineering and Structural Dynamics, 46*(14), 2459-2477.

Chapter 4 is being prepared for submission for publication:

- **Chen, M.**, Restrepo, J. I., and Benzoni, G. Response of a high damping rubber bearing to multiaxial excitation.

Chapter 5 is being prepared for submission for publication:

- **Chen, M.**, Restrepo, J. I., and Blandon, C. Seismic design framework for inertia-sensitive nonstructural components in base isolated buildings.

VITA

2008	Bachelor of Science, University of California, San Diego
2009	Master of Science, University of California, Berkeley
2018	Doctor of Philosophy, University of California, San Diego

PUBLICATIONS

Chen, M. C., Pantoli, E., Wang, X., Espino, E., Mintz, S., Conte, J., Hutchinson, T., Marin, C., Meacham, B., Restrepo, J., Walsh, K., Englekirk, R., Faghihi, M., & Hoehler, M. (2012). Design and construction of a full-scale 5-story base isolated building outfitted with nonstructural components for earthquake testing at the UCSD-NEES facility. *Proceedings, ASCE Structures Congress*, 1349-1360.

Chen, M. C., Astroza, R., Pantoli, E., Hutchinson, T., Restrepo J. I., Conte, J. P., & Bachman, R.E. (2013). Seismic performance of a full-scale five-story building shake table tested in a base-isolated and fixed-base configuration. *Proceedings, Vienna Congress on Recent Advances in Earthquake Engineering and Structural Dynamics (VEESD).*

Chen, M. C., Pantoli, E., Astroza, R., Ebrahimian, H., Mintz, S., Wang, X., Hutchinson, T., Conte, J., Restrepo, J., Meacham, B., Kim, J. & Park, H. (2013). BNCS report #1: full-scale structural and nonstructural building system performance during earthquakes and post-earthquake fire - specimen design, construction and test protocol. *Structural Systems Research Project Report Series, SSRP 13/9*. University of California San Diego, La Jolla, CA.

Chen, M. C., Pantoli, E., Wang, X., Mintz, S., Hutchinson, T., & Restrepo, J. (2013). BNCS Report #4: Full-scale structural and nonstructural building system performance during earthquakes and post-earthquake fire – construction details and technical specifications of specific subsystems. *Structural Systems Research Project Report Series, SSRP 13/12*. University of California San Diego, La Jolla, CA.

Chen, M., Restrepo, J. I., & Benzoni, G. (2015). Performance of a high damping rubber bearing to multiaxial excitation. Proceedings, 14th World Conference on Seismic Isolation, Energy Dissipation and Active Vibration Control of Structures (14WCSI).

Chen, M., Pantoli, E., Wang, X., Astroza, R., Ebrahimian, H., Hutchinson, T., Conte, J., Restrepo, J., Marin, C., Walsh, K., Bachman, R., Hoehler, M., Englekirk, R., & Faghihi, M. (2016). Full-scale structural and nonstructural building system performance during earthquakes: part I – specimen description, test protocol and structural response. *Earthquake Spectra*, *32*(2), 737-770.

Chen, M., Restrepo, J. I., & Benzoni, G. (2017). Impact of dynamic multiaxial excitation on the performance of a high damping rubber bearing. *Proceedings, 16th World Conference on Earthquake Engineering (16WCEE).*

Chen, M., Astroza, R., Restrepo, J. I., Conte, J. P., Hutchinson, T., & Bock, Y. (2017). Predominant period and equivalent viscous damping ratio identification for a full-scale building shake table test. *Earthquake Engineering and Structural Dynamics, 46*(14), 2459-2477.

Pantoli, E., **Chen, M. C.**, Wang, X., Astroza, R., Ebrahimian, H., Hutchinson, T. C., Conte, J. P., Restrepo, J. I., Marin, C., Walsh, K. D., & Bachman, R. E. (2016). Full-scale structural and nonstructural building system performance during earthquakes: Part II-NCS damage states. *Earthquake Spectra*, *32*(2), 771-794.

Pantoli, E., **Chen, M. C.**, Astroza, R., Ebrahimian, H., Mintz, S., Wang, X., Hutchinson, T., Conte, J., Restrepo, J., Meacham, B., Kim, J., & Park, H. (2013). BNCS Report #2: Full-scale structural and nonstructural building system performance during earthquakes and post-earthquake fire - test results. *Structural Systems Research Project Report Series, SSRP 13/10.* University of California San Diego, La Jolla, CA.

Pantoli, E., **Chen, M. C.**, Hutchinson, T., & Restrepo, J. (2013). BNCS Report #3: Full-scale structural and nonstructural building system performance during earthquakes and post-earthquake fire – camera and analog sensor details. *Structural Systems Research Project Report Series, SSRP 13/11.* University of California San Diego, La Jolla, CA.

Pantoli, E., **Chen, M.**, Hutchinson, T., Underwood, G. A., & Hildebrand M. (2013). Shake table testing of a full-scale five-story building: seismic performance of precast concrete cladding panels. *Proceedings, Compdyn*.

Pantoli, E., Wang, X., **Chen, M**., Hutchinson, T., Meacham, B., & Park, H. J. (2013). Shake table testing of a full-scale five-story building: performance of the major nonstructural components-egress and façades. *Proceedings, Structures Congress*, 1447-1459.

Pantoli, E., **Chen, M. C.**, Hutchinson, T. C., Astroza, R., Conte, J. P., Ebrahimian, H., Restrepo, J. I. & Wang, X. (2016). Landmark data set from the building nonstructural components and systems (BNCS) project. *Earthquake Spectra*, *32*(2),1239-1259.

ABSTRACT OF THE DISSERTATION

Enhanced Seismic Resiliency for Buildings via Base Isolation

by

Michelle Chen

Doctor of Philosophy in Structural Engineering

University of California, San Diego, 2018

Professor José I. Restrepo, Chair

Base isolation is an effective technology for reducing seismic damage to both structural and nonstructural components, as well as to building contents, allowing buildings to remain functional during and in the aftermath of a rare and strong intensity earthquake. This makes it an ideal seismic response modification system for hospitals and buildings of high importance. Despite the enhanced seismic resiliency of buildings incorporating base isolation, many countries have been slow to adopt it in building designs prior to experiencing the devastating effects of a major earthquake, often embracing the technology as an outcome. The goal of the research in this dissertation is to advance the understanding of base isolation, in order to diminish some of the barriers that impede its widespread use.

This dissertation uses data collected from a shake table experiment of a full-scale five-story building outfitted with nonstructural components and systems to analyze the structural response of the building in both base isolated and fixed base configurations. By simulating a realistic environment, this project documents the destructive effects of an earthquake with and without base isolation, ultimately demonstrating the technology's effectiveness in minimizing structural demands.

Another test that was conducted addressed the specific response of an isolator in realistic earthquake conditions. One of the barriers that prevents the use of base isolation in certain scenarios is because of gaps in knowledge due to lack of testing. To address this, a comprehensive multiaxial testing program of a high damping rubber bearing was performed, fully characterizing the bearing in six degrees of freedom, to understand the impact of realistic loading conditions on the isolator response.

Finally, base isolation is often implemented in buildings specifically to protect nonstructural components and ensure functionality of the building after an earthquake. Despite this, current design codes do not specifically address nonstructural components within base isolated buildings. This dissertation proposes a framework for designing inertia-sensitive nonstructural components within base isolated buildings. The framework is demonstrated through a case study using experimental structural response data in conjunction with simulated nonstructural responses generated by relative displacement floor response spectra for inelastic response.

Chapter 1

INTRODUCTION

Intense earthquake ground motions can be devastating to communities and even to countries. Regions that have suffered major seismic damage from earthquakes can take years and even decades to recover. The goal of current building codes is to preserve life safety, and to a lesser extent prevent damage to structural and nonstructural components. Nonstructural components and systems are those elements that facilitate the operation of a building, which include, among others: architectural façades, mechanical, electrical and plumbing systems, partition walls, and stairs. Nonstructural components and systems make up a large part of a building's cost; therefore, damage to these components can lead to significant costs for repair, replacement, and downtime. Damage to nonstructural components can also pose a threat to safety for people in the building. Recent earthquakes repeatedly demonstrate that nonstructural components are vulnerable to seismic damage. To minimize the recovery time after an earthquake and thereby enhance the resiliency of a community at large, these components and systems should be protected from damage. The future of seismic design should be to design buildings that are in line with a newer mindset of resiliency, one that features a comprehensive accounting of structural and nonstructural components, so that buildings experience minimal damage or no damage at all. The ultimate goal is to design buildings that remain functional during and in the aftermath of a major earthquake.

The technology at the forefront of addressing this mindset is base isolation. Base isolation effectively protects both structural and nonstructural components of a building by decoupling the building response in its entirety from the potentially damaging effects of earthquake input ground motions. Many areas of the world that have experienced intense earthquakes in the recent past have significantly increased the use of base isolation in response to societal demands and in an effort to enhance the resiliency of the building. Despite the benefits of using base isolation in seismic regions, some countries, including the United States, have been slow to embrace this technology. Many factors are thought to contribute to this discrepancy, including: initial cost, gaps in knowledge of the isolator behavior in realistic conditions, setbacks due to code requirements, and lack of motivation because there have not been recent major earthquakes in these regions. The goal of the author’s research is to advance the understanding of base isolation, and diminish some of the barriers that impede the widespread use of the technology worldwide.

Chapter 2 details a shake table experiment, in which a full-scale five-story building outfitted with nonstructural components was subjected to a range of input ground motions while first in a base isolated configuration, then in a fixed base configuration. The response of the structural and nonstructural components were monitored with over 500 sensors and over 80 video cameras. This experiment simulating realistic conditions generated a valuable set of data that can be used to further research in seismic design and motivate changes in the field where necessary, before the next major earthquake. The data is used in this chapter to analyze the structural response in both scenarios, ultimately highlighting the effectiveness of base isolation in minimizing structural demands.

Chapter 3 further investigates the building response using data from the shake table experiments. The chapter describes simplified system identification methods which use strong motion data to characterize the predominant period and the associated equivalent viscous damping ratio of the building during the earthquake ground motions. For the fixed base building, the change in effective stiffness is tracked and classified as “degraded” or “recoverable stiffness”. For the base isolated building, a predominant period of the building-isolation system is established for a variety of peak isolator shear strains, which is then compared to results from traditional quasi-static prototype testing.

While quasi-static unidirectional or bidirectional prototype testing of isolators is required, there is a lack of experimental data on base isolators that reflects realistic loading conditions, which includes dynamic input in all six degrees of freedom. To gain an understanding of the response of an individual isolator in realistic loading conditions, Chapter 4 discusses an extensive experimental testing program of a high damping rubber isolator used in the shake table test introduced in Chapter 2. The isolator was subjected to coupled and uncoupled dynamic inputs in six degrees of freedom. Performance parameters often used in the design of base isolated buildings are analyzed and compared in the different loading conditions to understand how input in each degree of freedom impacts this isolator. The final test in this experiment took the bearing to dynamic failure.

Base isolation is often implemented in buildings specifically to protect its contents and nonstructural components, as well as to ensure functionality of the building during and after a seismic event. Despite this, in the current design codes, there are no design requirements specific to nonstructural components in base isolated buildings. Chapter 5 uses the structural response from the base isolated shake table tests described in Chapter 2 along with simulated nonstructural responses using relative displacement floor response spectra for nonlinear oscillators, to propose a seismic design framework for inertia-sensitive components in base isolated buildings.

1.1 Original Contributions

The experimental test program described in Chapter 2 is the first and largest full-scale shake table test program that was fully outfitted with nonstructural components in the U.S. The unique test collected data for the structural and nonstructural response in a base isolated configuration and a fixed base configuration as well as data on the interaction between structural and nonstructural components.

The test program was a collaboration between professors from four universities, and over 40 industry and government partners. The author was responsible for the base isolation test configuration of the full-scale five-story experiment described in Chapter 2. This included: analysis for the base isolation design; the analysis, design and detailing of the foundation; coordination with the isolator manufacturers and designers; planning and designing a system for the installation of the base isolators, as well as planning for the removal of the base isolators following the base isolated testing phase. During construction, the author was also responsible for coordinating the construction of the building on site. The author also coordinated with the industry partners for the installation of many of the nonstructural systems. The author was responsible for the layout and installation of the camera system and videos. Following the experimental phase, the author's research focused on analyzing the structural response of the building.

Chapter 3 utilizes data collected from the base isolated configuration and fixed base configuration from the experimental test program described in Chapter 2. This chapter presents three simplified methods for determining the predominant period of the building during strong ground motions, one of which is an existing method used for soil and other applications, and has been expanded to buildings for this study, and one of which is a novel method derived from an existing method. This method can easily be implemented in a design office. One of the system identification methods utilizes GPS data, which is not typically used for system identification purposes, during earthquake test motions to determine the predominant period and associated equivalent viscous damping ratio of the building. The building's stiffness reduction due to the progressive structural and nonstructural damage is tracked and disaggregated into recoverable and degraded stiffness.

Next, the author developed a research program, presented in Chapter 4, to test a high damping rubber bearing with dynamic coupled and uncoupled loading in six degrees of freedom and to take the bearing to dynamic failure. This testing program is the first of its kind and offers important information on characterizing the impact of realistic loading conditions on a high damping rubber bearing.

Finally, since there are currently no code provisions specifically for designing nonstructural components in base isolated buildings, the author developed a framework for designing inertia-sensitive nonstructural components for use in base isolated buildings. The framework is described in Chapter 5 and is illustrated through a case study with experimental structural data and simulated nonstructural responses of nonlinear oscillators using floor relative displacement response spectra for inelastic response.

Chapter 2

FULL-SCALE STRUCTURAL AND NONSTRUCTURAL BUILDING SYSTEM PERFORMANCE DURING EARTHQUAKES: SPECIMEN DESCRIPTION, TEST PROTOCOL AND STRUCTURAL RESPONSE

2.1 Abstract

A landmark experimental program was conducted to advance the understanding of nonstructural system performance during earthquakes. The centerpiece of this effort involved shake table testing a full-scale five-story reinforced concrete building furnished with a broad variety of nonstructural components and systems (NCSs) including complete and operable egress, mechanical and electrical systems, façades, and architectural layouts. The building-NCS system was subjected to a suite of earthquake motions of increasing intensity, while base isolated and then fixed at its base. In this chapter, the major components of the test specimen, including the structure and its NCSs, the monitoring systems, and the seismic test protocol are described in detail. Important response and damage characteristics of the structure are also presented.

2.2 Introduction

Nonstructural components and systems (NCSs), generally categorized as architectural, mechanical, electrical and plumbing, or building contents, are the elements that facilitate operation of a building. NCSs typically comprise 75-85% of the construction cost of commercial buildings (FEMA E-74, 2012). Therefore, it is not surprising that damage to NCSs during past earthquakes has resulted in significant economic losses due to repair, downtime, or loss of functionality of the NCS or building. In addition, they can endanger people during an earthquake. These losses have often occurred at seismic demands much lower than those that would result in damage to the structure (e.g., Ayres et al., 1973; Steinbrugge & Schader, 1973; FEMA E-74, 2012; Filiatrault et al., 2001; Meneses et al., 2010; Miranda et al., 2012).

The response of an NCS to an earthquake excitation depends not only on its dynamic characteristics and boundary conditions, but also on its interaction with the structure and with other NCSs. Although it is reasonably well understood that certain nonstructural components are more sensitive to accelerations, while others may be sensitive to damage induced by differential movements, the dynamic interaction that an NCS has with the structure is difficult to investigate without system-level experiments or simulations. Current experimental data on the behavior of NCSs has been largely collected through individual component testing. While these tests have provided a wealth of information, they have not addressed structure-NCS interactions or NCS-NCS interactions, both of which may significantly affect a component's behavior. An effort to capture the interactions of various nonstructural systems was attempted in a series of seismic tests, ranging from individual components to building segments (CUREE, 2013).

In these tests, however, the NCSs were focused solely on the ceiling-piping-partition systems.

To date only a handful of full-scale building experiments have been conducted. Of these, only a few were able to incorporate NCSs in their scope, and in most cases they were secondary to investigating the primary structural components performance. In general, only a limited amount of NCSs were implemented into the test at one time. For example, a number of full-scale building tests were conducted on the E-Defense shake table in Japan and a few incorporated NCSs (e.g., Matsuoka et al., 2008; Dao et al., 2011; Sato et al., 2011). One of these experiments tested the building in several base isolated configurations in addition to a fixed base configuration (Dao et al., 2011; Sato et al., 2011). Another example is a full-scale seven-story reinforced concrete wall building shake table tested to investigate the behavior of lightly reinforced wall systems (Panagiotou et al., 2011a, b). Within this test program, a suspended pipe system was included (Hoehler et al. 2009) and its interaction with the structural system was observed. While these and other prior large-scale building test programs integrated perhaps one or a few NCSs, a comprehensive experimental program, in which a broad variety of the essential NCSs needed to support a building's functionality are incorporated, has yet to be undertaken.

2.2.1 Scope of this Project

A unique collaboration between academia, government, and industry, coined the *Building Nonstructural Components and Systems* [*BNCS*] project, was formed to contribute to understanding the earthquake and post-earthquake fire resiliency of nonstructural components and systems (Hutchinson et al., 2013; BNCS, 2014). Technical oversight to the project was provided by three different committees consisting of experts in design, construction and regulatory practice; university faculty and researchers active in structural, nonstructural, and earthquake research; and material/product suppliers of NCSs. The centerpiece of this effort involved shake table and live fire testing of a full-scale five-story reinforced concrete building outfitted with a large variety of essential NCSs. These tests, which were completed in 2012, contribute a wealth of high-resolution physical data to the earthquake and fire engineering communities and will provide direct input to modeling tools, future design codes, and construction practices.

This landmark experimental program was conducted at the George E. Brown, Jr. Network for Earthquake Engineering Simulation outdoor shake table at the University of California, San Diego (NEES@UCSD) unidirectional Large High-Performance Outdoor Shake Table (LHPOST) (Van den Einde et al., 2004; Ozcelik et al., 2008). The project involved three physical phases of testing: (i) earthquake shaking while the building was isolated at its base (BI phase), (ii) earthquake shaking while the building was fixed at its base to the shake table (FB phase), and (iii) post-earthquake live fire tests within select earthquake damaged compartments. Within the test building, more than 40 industry partners collaborated to assist the research team in the design and installation of operable egress systems (elevator and metal stairs), a complete façade, and a broad array of architectural layouts, including two floors of the building designed as medical facilities. Additional details of the experimental program, seismic testing phases, and findings may be found in papers and a series of technical reports (Hutchinson et al., 2013; Chen et al., 2012, 2013a, b; Pantoli et al., 2013a-c, 2016a-b). In addition, findings of the post-earthquake fire-testing phase may be found in Meacham et al. (2013), Kim et al. (2013), and Park et al. (2014).

In this chapter, the design and construction of the test building and its various NCSs is described. Subsequently, the selection of seismic motions is discussed. The chapter concludes by summarizing global building (primary structure) system responses.

2.3 Building Design and Construction

A cast-in-place reinforced concrete special moment frame was selected to carry the building's gravity and lateral loads in its longitudinal (east-west) direction, parallel to the direction of shaking. This type of design is common in mid to high-rise buildings in areas of high seismic hazard. In the transverse direction, two concrete shear walls and steel rods, configured as tension cross bracing members, were oriented perpendicular to the direction of input motion. The building was supported on a stiff post-tensioned foundation designed to accommodate both its isolated and fixed base configurations (Figure 2.1a). It is noted that the design and construction documents for the building were primarily prepared in English units; however, SI units are adopted for this chapter.

2.3.1 Foundation Design

The foundation of the building was constructed directly on top of the shake table platen and designed to remain uncracked throughout the different construction and testing stages. It incorporated perimeter and interior beams geometrically placed to support the six framing columns, a first-floor slab, transverse shear walls, and an elevator pit for the building. To accommodate the elevator pit and allow for sufficient reinforcement to support the anticipated loading conditions, the top of the foundation was 1.5 m above the shake table platen. The north and south foundation beams were designed with pockets for the base isolators, resulting in varying depths along the beam

(1.5 m at the full depth of the foundation beams and 1.2 m above the isolator pockets) (Figure 2.1b).

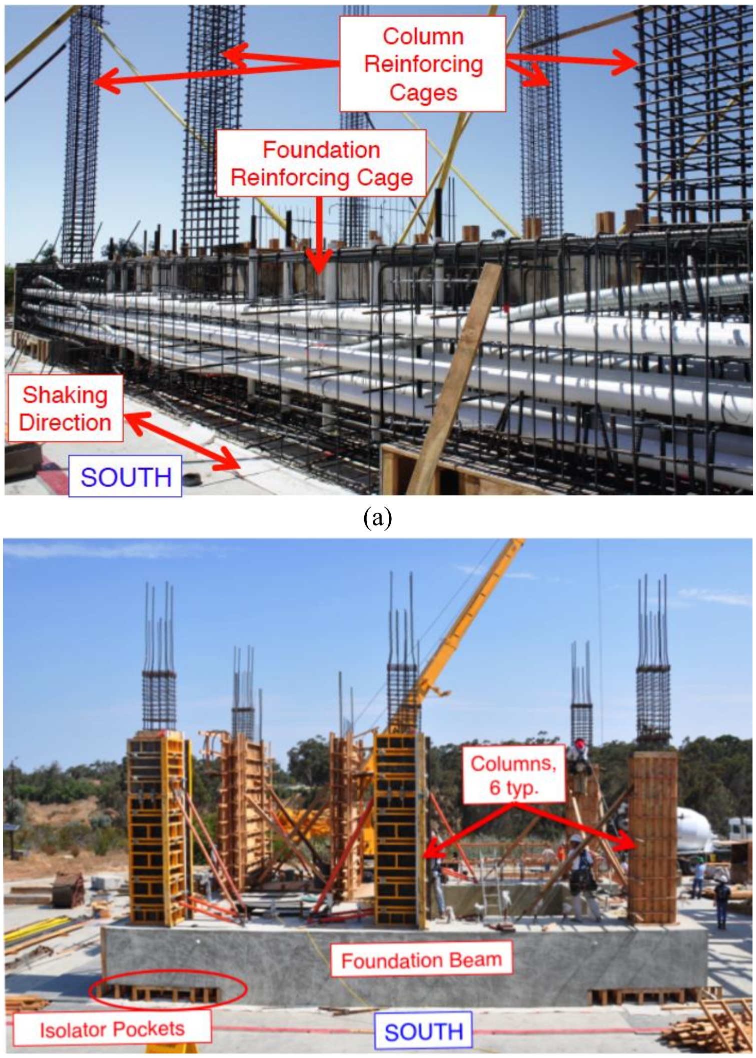

(a)

(b)

Figure 2.1: Foundation during construction: (a) steel cage prior to concrete pour, showing ducts for post-tensioning rods and tendons and (b) after concrete pour (view of south foundation beam).

2.3.2 Superstructure Design and Detailing

The test building was designed for a location in Southern California where site-specific ground motions were available. The available site-specific maximum considered earthquake ground motion spectrum was developed for a Site Class D (stiff) soil conditions and had a short-period spectral acceleration S_{MS} = 2.10 g and a one-second spectral acceleration S_{M1} = 1.43 g. A displacement-based design methodology was utilized for the design of the structure, with performance targets of 2.5% peak interstory drift ratio (PIDR) and maximum peak floor acceleration (PFA) between 0.7 g - 0.8 g selected during the conceptual design phase.

To optimize the available footprint of the NEES@UCSD shake table, the test building had a plan dimension of 6.6 m by 11.0 m at its base. It was composed of two open bays in the shaking direction (longitudinal) and one in the non-shaking direction (Figure 2.2). The floor-to-floor height was 4.3 m resulting in a total height of the bare structure 22.9 m above the shake table platen (~27 m including the roof mounted equipment). At the east end of each floor of the building, there were two special moment resisting frames aligned with the primary axis of shaking. The beams in these frames were 300 mm wide by 700 mm deep. While different beam detailing was adopted at each floor level of the building (Figure 2.2a), beam column connections were designed with equivalent beam moment capacities of about 390 kN-m at the column faces for all levels. The second and third floor beams utilized high strength reinforcement (f_y = 827 MPa) to achieve the desired moment capacity. The fourth and fifth floor beams both used ductile rods at beam-column joints. In addition, the fourth-floor beams incorporated hybrid frame details (ACI T1.2-03/T1.2R-03, 2003; Chen et al., 2013a). Frame beam and column joint details adopted on floors two through five exhibited stable ductile performance in previous component test programs (Warcholik & Priestley, 1998a, b; Chang et al., 2008; Chang et al., 2013) and have since been used in practice. For comparison, at the roof, where the lowest seismic forces were anticipated, special moment frame detailing followed the prescriptive requirements in ACI 318-08 (ACI, 2008). Although the longitudinal reinforcing was varied within the beams on each floor, confining steel within the frame beam was consistently provided by 13M (#4) ties at 102 mm on center at the column faces and 152 mm along the remaining beam. A 200 mm thick cast-in-place slab provided the floor support for each level. The 460×660 mm columns were detailed with transverse reinforcing steel prefabricated into grids and spaced at 102 mm on center, with a longitudinal reinforcement ratio ρ_l = 1.42%. The axial load due to self-weight of the building and its NCSs varied between 1.8% - 5.3% × $A_g f'_c$ (where A_g = gross cross-sectional area and f'_c = unconfined compressive strength of the column) at the base of the columns. All structural components of the building and foundation were cast-in-place concrete, with a specified 28-day f'_c of 40 MPa for the columns and elevator shear walls and 35 MPa for the beams and slabs. A summary of achieved f'_c values from compression testing of cylinders from each concrete truck and measured modulus of elasticity values E_c from a select number of cylinders is presented in Table 2.1.

Table 2.1: Summary of results for compressive concrete cylinder tests.

Component	Average f'_c at 28 days (MPa)	Average f'_c at start of seismic testing (MPa)	Average E_c at start of seismic testing (GPa)
Columns and walls	44.1	57.2	32.6
Slabs and beams	39.3	51.7	33.1

Openings of 2.3×4.2 m and 2.1×2.6 m were provided in the floor diaphragm to accommodate full-height stairs and an elevator, respectively (Figure 2.2b). In addition, 100 mm - 250 mm nominal diameter penetrations in the floor slab were provided to allow passage of building services (plumbing, fire sprinklers, and electrical) and sensor/camera cables. Most of the smaller openings were located along the north and west sides of the elevator opening. Concrete shear walls, with a thickness of 150 mm, were constructed on either side of the elevator opening and ran transversely in the building to connect the brackets that provided stability for the elevator guiderails as well as to provide transverse stability of the building during the seismic tests. These walls were detailed with 10M (#3) rebar spaced at 152 mm on center in both directions with two 29M (#9) longitudinal bars at each end. It is noted that two useful architectural spaces, namely the northeast and southwest rooms, shown in Figure 2.2b, were available on each floor. Occupancies designated for these spaces will be discussed later.

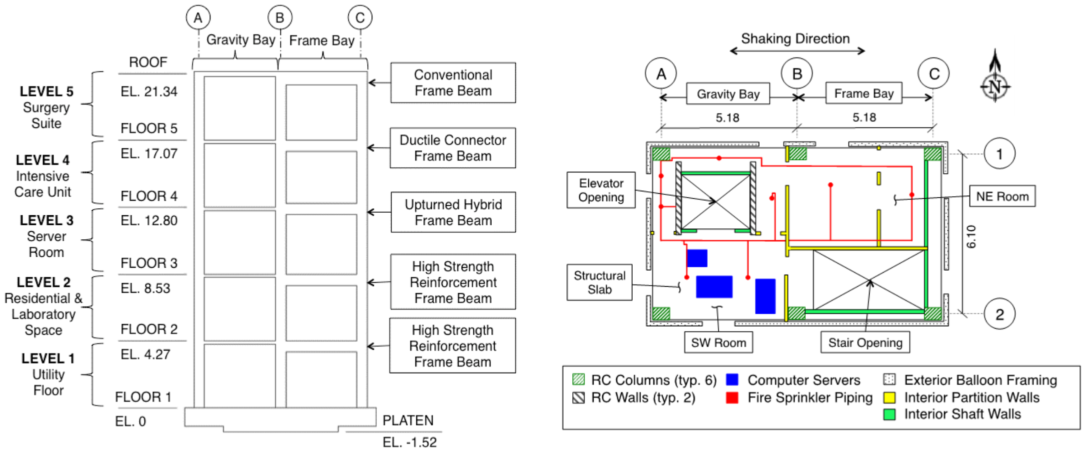

(a) (b)

Figure 2.2: Schematic overview of (a) building elevation (along shaking direction) indicating floor occupancy and frame beam type and (b) plan view of level three identifying primary structural components and typical fire sprinkler layout, exterior balloon framing, interior partition walls and computer servers.

2.3.2.1 Construction

Construction of the foundation began in May 2011 and was completed in June 2011. Subsequently, superstructure construction began at a rate of one level every two to three weeks. The dates of the concrete pour for each floor level are shown in Figure 2.3a and images of the building at different stages of construction are shown in Figure 2.3(b-c). Following completion of the superstructure construction, installation of nonstructural components began. Additional discussion of construction and scheduling may be found in Espino (2012).

(a) (b) (c)

Figure 2.3: (a) Dates of concrete pour for the slab at each level and images during construction – note that stairs were installed during the building skeleton erection, (b) image before construction of fourth floor slab, and (c) before construction fifth floor slab.

2.3.3 Isolator Specifications

For the first phase of testing, the foundation of the building was supported by four high damping rubber isolators placed nearly below the corner columns. These 650 mm diameter isolators consisted of 34 rubber layers with a steel layer placed between each to provide vertical stiffness. Each rubber layer was 6 mm thick, resulting in a total rubber thickness of 204 mm, while the 33 steel plate layers were each 3 mm thick; as a result, the total height of the isolator was 343 mm.

The manufacturer performed quality control tests on the base isolators consisting of six amplitude sequences of sinusoidal fully reversed shear deformation with amplitudes (based on the rubber height) ranging from 25% to 150% at 25% increments. It is noted that a shear deformation of 150% corresponds to an isolator displacement of 300 mm. Each sequence was composed of seven cycles to the prescribed amplitude. From these tests, the average secant stiffness at 150% shear strain was 730 kN/m and the average equivalent viscous damping ratio was 11%. Additional details of the isolators, including quality assurance test results, may be found in Chen et al. (2013b).

2.4 Nonstructural Components and Systems

The building was outfitted with a broad variety of NCSs following completion of the construction of its structural skeleton. Apart from the metal stairs, all NCSs were installed between September 2011 and April 2012. In what follows, a project-specific NCS design criteria, as well as the specific details of the various NCSs installed in the test building, are presented. It is noted that including the installed NCSs, the building weighed approximately 6290 kN; whereas its bare weight was 4880 kN, with the foundation contributing about 1870 kN of the total in each case.

2.4.1 NCS Design Criteria

Two nonlinear finite element models were developed independently prior to conducting shake table testing: (1) a model implemented in the OpenSees platform (Wang et al., 2013; Mazzoni et al., 2013), and (2) a model prepared using DIANA (Ebrahimian et al., 2013; TNO DIANA, 2010a, b). In addition to guiding the selection of test motions, nonlinear response history results obtained using these two finite element models, subjected to the input motion selected to achieve the design target drift ratio (FB-5), were utilized to develop recommended criteria for design of the NCSs and their anchorage or bracing to the test building. Values from Tables 2.2 and 2.3 were provided to the NCS designers and suppliers with the intent that they design their products based on the project specific values when possible. For acceleration-sensitive NCSs, a modified version of the formula currently prescribed by ASCE 7-10 (ASCE/SEI, 2010) was adopted:

$$F_p = \frac{0.4 a_p S_{DS}}{\left(\frac{R_p}{I_p}\right)} \left(1 + 2\frac{z}{h}\right) W_p \tag{2.1}$$

where F_p is the seismic design force, a_p is the component amplification factor, S_{DS} is the short (0.2 s) period spectral acceleration of the design motion, I_p is the component importance factor, W_p is the component operating weight, R_p is the component response modification factor, z is the height of the structure at the point of component attachment, and h is the average roof height of the structure relative to the base elevation. It is noted that per ASCE 7-10, F_p shall not be taken less than 0.3 S_{DS} I_p W_p, nor required to be greater than 1.6 S_{DS} I_p W_p.

For this project, the term $S_{DS}(1 + 2z/h)$ in Equation 2.1 was replaced with the values summarized in Table 2.2 to better capture the distribution of acceleration up the height of the building. The spectral accelerations in the second column of Table 2.2 are the mean plus one standard deviation of the values over the period range of interest (from 0.06 s to 0.6 s) of the average floor acceleration response spectra. It is noted that the average floor acceleration spectra were generated using the floor acceleration histories obtained from the two nonlinear finite element models. A period ranging from 0.06 s to 0.6 s was selected to encompass the current codified definition for rigid to assumed flexible nonstructural components. For comparison, values obtained using the code estimation with Equation 2.1 are shown in the third column of Table 2.2.

For drift sensitive components, the maximum interstory drift ratio that nonstructural components are required to accommodate depends on the type of structure, the number of stories, and the risk category (ASCE/SEI, 2010). To provide a more accurate estimation of drift demands anticipated for the NCSs installed in the test building, the maximum interstory drift ratios from both the two pre-test nonlinear finite element response simulations, were averaged (Table 2.3). It is noted that these values agree with codified values within ASCE 7-10 (about 2 - 2.5%) within the mid-height of the test building (levels 2 - 4), but are less than half that predicted for the upper most level 5.

Table 2.2: Recommended project specific design floor spectral acceleration values (intended to replace code value) and those suggested by ASCE 7-10, assuming an S_{DS} = 1.4.

Floor of attachment	Project-specific value (g)	Code value: S_{DS} (1 + 2 z/h) (g)
1	1.29	1.40
2	1.82	1.96
3	2.49	2.52
4	2.33	3.08
5	1.60	3.64
Roof	2.84	4.20

Table 2.3: Recommended project specific design interstory drift ratio.

Level	Interstory drift ratio (%)
1	1.8
2	2.6
3	2.5
4	2.0
5	1.1

2.4.2 Egress

The test building was equipped with two types of egress systems, namely (1) a steel stair assembly and (2) a functioning passenger elevator. The stairs provided access to all floors including the roof, whereas the elevator provided access to all floors except the roof.

2.4.2.1 Steel Stairs

The stairs were configured as a scissor assembly, with two flights reversed upon each other and one intermediate landing (Figure 2.4a). The steel stair flights, landing, and rails were manufactured off site and assembled in parallel with construction of the building superstructure. Attachment of the flights to the building was facilitated via field welding to steel embeds cast with the beams and slabs (Figure 2.4b,c). A plate with a reduced area at the upper flight to slab connection was intended to yield during relative floor-floor displacements. Flights were field-bolted to the landing joists on the opposing ends.

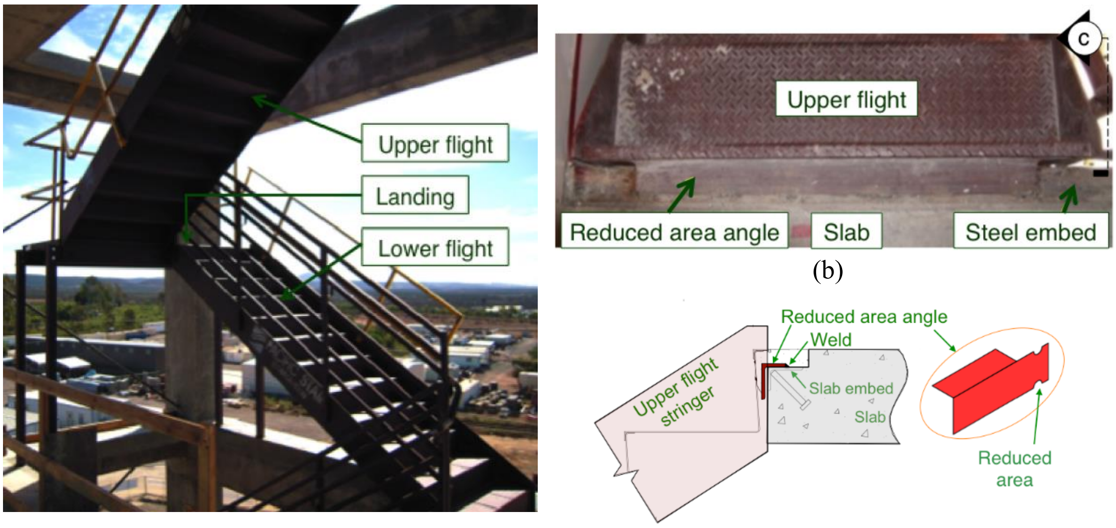

(b)

(a) (c)

Figure 2.4: (a) Image of the stair scissor assembly, (b) upper flight to slab connection and (c) detail from part b: section of slab embed to stair connection detail and isometric of reduced area plate.

2.4.2.2 Passenger Elevator

A fully functional passenger elevator was installed in a shaft extending from the ground floor to the fifth floor. The elevator, which had a total travel height of 17.1 m, consisted of a cabin, a counterweight, guide rails and brackets, pit equipment, and a machine drive. The machine drive and suspension supports were located at the top of the east side of the hoist way and were supported by guide rails. Select elevator components are shown in Figure 2.5.

The elevator cabin was 2.1 m wide by 1.7 m deep with a height of 2.4 m (interior dimensions) and a mass of 1013 kg (Figure 2.5a). Using sand bags, an additional mass of 635 kg, equivalent to 40% of the elevator's rated load capacity, was added in the cabin during all testing phases. During all seismic tests, except two - where the cabin was on level five, the cabin was located at the first level (design position) and the counterweight was located at level five. An elevator door opening (2.3×1.1 m) was located on each level (Figure 2.5b). The counterweight frame was 2.7×1.4×0.1 m and its total mass (including the steel counterweights themselves) was approximately 1650 kg (Figure 2.5c).


(a) (b) (c)

Figure 2.5: Major elevator components: (a) hoist way and top of cabin, (b) elevator doorway with sandbags inside cabin, and (c) counterweight and guiderails.

2.4.3 Architectural Façades

Two different types of architectural façades were installed on the building (Figure 2.6), namely: (1) balloon framed cold-formed steel (CFS) studs overlaid with a synthetic stucco (exterior) at the first three levels (levels 1 - 3) and (2) precast concrete cladding panels at the upper two levels (levels 4 and 5).

2.4.3.1 Levels 1-3: Cold-Formed Steel (CFS) Balloon Framing Overlaid with Synthetic Stucco

CFS studs were balloon framed, meaning the studs spanned continuously over multiple (three) floors, and placed between two layers of fire-rated gypsum boards - one on the interior and one on the exterior of the building. The exterior layer of gypsum was overlaid with a finishing system to create a lightweight architectural façade. The finishing system was comprised of a waterproof barrier made of mesh and a waterproof coating, a thermal insulation system made of expanded polystyrene, and an outer layer of synthetic stucco (Figure 2.6). CFS studs were placed vertically from the foundation to the fourth-floor slab at a spacing of 0.4 m on center. The studs were connected to the foundation with powder-actuated fasteners and to each floor slab with outrigger clips. Construction of the balloon framed façade spanning from levels 1 - 3 required nearly three months and the use of temporary scaffolding.

2.4.3.2 Levels 4–5: Precast Concrete Cladding Panels

On the fourth and fifth floors of the building, sixteen punch-out window style precast concrete cladding panels were installed (Figure 2.6c); eight panels were installed at each floor, with four in the longitudinal direction and four in the transverse direction (two on each side of the building) (Figure 2.6d). The panels spanned from floor to floor and each had a single window opening. The larger panels installed on the north and south ends of the building had masses between 4800 and 5900 kg, while the smaller panels on the east and west ends of the building had masses between 3700 and 4300 kg.

(a) (b) (c) (d)

Figure 2.6: Construction phases of the façade: (a) after installation of balloon framed CFS studs, (b) after installation of the exterior gypsum boards, (c) installation of the concrete cladding panels and (d) completed façade.

Individual panels were supported at their base with bearing connections and their top with push-pull connections designed to accommodate large levels of interstory drift. Several types of top connections were implemented:

- Push-pull connection with a ductile fuse: these connections were located at panels moving out-of-plane and designed to ensure a predictable behavior and well defined damage location.
- Sliding push-pull connections: drift in these connections was accommodated via a rod extending through a slotted plate. The slotted plate is intended to allow free movement of the rod as the panel displaces relative to the building. Three lengths of rods were tested in these connections: snug, medium = 89 mm, and long = 178 mm.
- Flexing rod push-pull connections: drift in these connections was accommodated via flexing of a rod connected to a clip, which attached to the building. Three rod

lengths were tested in these connections: short = 305 mm, medium = 405 mm, and long = 510 mm.

In addition to varying the top connection details, both butt and miter joints were implemented at the intersection between panels at the corners of the building. Mechanical installation of the panels onto the building spanned two days, and was followed by placement of caulking at all panel-panel and panel-balloon framing gaps.

2.4.4 Interior Architectural Components

Occupancy largely dictated the details and types of NCSs installed in the building. Level one was designated as a utility floor allowing sufficient space for placement of electrical services and installation of four large access doors (two steel rolling doors and two sectional garage doors) placed on the longitudinal faces of the building. Level two was detailed as both a laboratory and residential space, while level three was planned for live fire tests and therefore provided with the most complete detailing of partition walls, ceilings, plenum space and associated finish work. In addition, two large computer servers were anchored to the slab at level three. Levels four and five were detailed as hospital floors. The equipment installed on each of these floors is described in later sections.

2.4.4.1 Ceilings

Each room on every level of the building had a different ceiling type to allow for the investigation of the behavior of various common practices. To facilitate comparison, the ceiling system at level one was designed lacking seismic provisions, typical to ceilings used in the eastern regions of the United States. The second level’s ceiling systems were designed typical to areas of high seismic hazard and used compression posts with splay wires that were attached with post-installed anchors. At level three, the ceiling system used drywall supported on a grid. The fourth floor's ceiling was designed for high seismicity and to carry the large loads expected of hospital equipment placed within the plenum space or attached to the ceiling itself. The fifth level utilized an open steel structural framing system in the northeast room designed to support heavy surgical equipment, therefore no ceiling was provided in this space. The southwest room's ceiling was a drywall ceiling, commonly used for hospital occupancies in seismic regions. The penthouse ceiling was designed to represent a hospital corridor with the maximum spacing between vertical hanger wires to allow for the least congested plenum space, often a necessary attribute for hospital corridor plenum spaces.

2.4.4.2 Partition Walls

Interior partition walls constructed of CFS studs overlaid with gypsum board were installed on all levels of the test building, with their layout primarily dictated by the floor occupancy. The wall types can be divided into two categories: shaft walls, consistently found at the front (south) and back (north) sides of the elevator shaft and the east and south faces of the stair wells at each level, and regular partition walls with their locations varying by floor. Shaft walls were detailed as fire-rated with a layer of fire-rated gypsum board on each face, whereas regular partition walls had either one or two layers of gypsum board, depending on the finish required. The two types of walls, although different in detailing and installation procedure, both followed the current standards of practice. An example of the partition wall layout for level 3 is provided in Figure 2.2b.

2.4.4.3 Level 1: Access Doors

Two large openings in the balloon framing on both the north and south side of the building were provided to accommodate access doors that might commonly be found on the ground level of a building. Two 2.9×2.1 m sectional garage doors and two 2.9×2.1 m steel rolling doors were installed in these openings. The sectional garage doors were installed in the northeast and southwest openings, whereas the steel roll-up doors were installed in the northwest and southeast openings (Figure 2.6d). To increase the variability of testing conditions, both doors on the north side (one sectional and one roll-up door) remained open during seismic testing, while both doors on the south side remained closed during testing. Since the doors on the first level were located on the north and south sides of the building (parallel to the direction of input motion), they were each subjected primarily to in-plane motion.

2.4.5 Services

Services common to a building were installed to varying degrees of detail on each floor of the building. The details of these services are described in the following sections.

2.4.5.1 Heating, Ventilation and Air Conditioning (HVAC)

A terminal HVAC unit was installed on the fourth level of the building with its complete support ductwork installed in the plenum space of the third level. This system was not operational, though it was intended to replicate the typical congestion that might be encountered with an active service plenum space. In addition, three smoke dampers were installed in each of the two HVAC ducts on the third floor.

2.4.5.2 Electrical Distribution System

The electrical distribution system was fully functional and installed with a different configuration at every floor. By powering the building with an external gas generator, the building’s electrical distribution system provided live power during shake table testing to the elevator, a complete interior lighting system, the roof mounted equipment, and most medical equipment.

2.4.5.3 Fire Sprinkler System

A fire sprinkler system was installed throughout the building, with main and branch lines as well as sprinkler heads placed at every floor. Most layouts were similar to that shown in Figure 2b. The piping material varied on the different levels and included steel piping with threaded couplings and rigid sprinkler drops, steel piping with flexible hose sprinkler drops, and plastic piping. The pipes were filled with water and the hydrostatic head associated with each floor were monitored with a pressure gage to identify if water leaks occurred during the tests. The piping on levels one and four was supplemented with added weights attached to the main lines to simulate the water weight of a larger floor plan.

2.4.5.4 Gas Piping

A flexible and a rigid gas pipe were installed at every floor within the plenum space and along the interior partition walls. The gas was under pressure and the pressure could be checked for integrity following each test motion using a gauge installed at the first floor.

2.4.6 Equipment

2.4.6.1 Level 2: Residential and Laboratory

The second floor was designated as a residential space (Figure 7a) in the southwest room and a laboratory space (Figure 7b) in the northeast room. A variety of equipment and furniture typically found in these two types of environments were arranged within these spaces. Within the laboratory environment, storage racks with glassware, a cabinet for flammable material storage, lab freezers and a refrigerator, and storage cabinets were included. The home office was equipped with a bookcase, office equipment, a kitchen refrigerator, a vertical file cabinet, storage cabinets, and a table. The heaviest items on this floor were the freezers, with masses ranging from 30 to 275 kg. A variety of staging considerations were implemented during the motion sequence. In some cases, equipment was restrained, while during other motions, the equipment was unrestrained to allow for comparison of their behavior.

2.4.6.2 Level 3: Computer Servers

The southwest space of the third floor was designated as a server room, with two large computer servers (mass ~1350 kg) and one control unit (mass ~225 kg) (Figure 2.7c). One server unit was functioning, and its operability was monitored in real-time during all seismic motions. The functioning unit was installed such that its long direction was parallel to the direction of input motion, whereas the non-functioning unit was installed with its long direction perpendicular to the direction of input motion.

(a) (b) (c)

Figure 2.7: (a) Residential and (b) laboratory space on level two. (c) Computer server on level three. Arrows on slab indicate direction of input motion. Units: meters.

2.4.6.3 Levels 4-5: Medical

Level four was designed to simulate an intensive care unit (Figure 2.8a) and level five was designed to mimic a surgery suite (Figure 2.8b). To complete these layouts, medical equipment typically installed in an intensive care unit and surgery suite were installed on level four and level five, respectively, with a variety of equipment attachment configurations including wall mounted, ceiling mounted, floor mounted, and unattached equipment on wheels.

Equipment on the fourth floor included patient care beds, a patient lift, an operable nurse call system, breakout doors, headwalls, a medical gas column, ultrasounds imagers, and mobile workstations. In addition to the medical equipment, several realistically sized and weighted mannequins were placed in the beds and in the patient lift to simulate the effect of a patient on the equipment during an earthquake.

Medical equipment on level five included a hospital freezer (250 kg), wall and floor mounted storage cabinets and shelving, medical gas booms, surgical lights, patient care stretchers (mass loaded with 84 kg of steel plates), and a nurse call annunciator. The heavy surgical lights were hung from the stiff steel ceiling structure installed at the underside of the building's roof slab (upper right of Figure 2.8b).

(a) (b)

Figure 2.8: (a) Intensive care unit on level four and (b) surgery suite on level five.

2.4.6.4 Roof: Penthouse, Air Handling Unit, Cooling Tower

A penthouse was constructed at the roof level above the stairway opening to provide shelter (Figure 2.9a). The penthouse was constructed using CFS framing members and fire rated gypsum boards, similar in construction and installed by the same contractor that installed the balloon framing and interior partition walls. The exterior plan dimensions of the penthouse were approximately 6.0×3.0 m and it was 3.0 m in height, with a mass of 1600 kg. The penthouse design followed ASCE 7-10 and considered both wind and seismic loads using the building-specific design criteria discussed previously.

An air-handling unit was supported by a seismic curb, which was fixed to the roof slab using post-installed anchors on the southwest corner of the roof (Figure 2.9b). This unit was non-functional, and its dimensions were roughly 1.5×2.5 m and its height was 1.72 m. The unit's mass was approximately 680 kg.

A cooling tower was installed on the northeast side of the roof. The area of the tower was 2.14×2.73 m with a total height of 3.25 m (Figure 2.9a). The (empty) shipping mass of the cooling tower was 1590 kg. During seismic testing, the cooling tower was filled with water to its design operating level and therefore had a total mass of 2845 kg.

The cooling tower was supported by a steel frame that was attached to isolator/restraint systems at each of its four corners. Below the I/R systems, the frame was connected to five-channel load cells, which were fastened to the roof slab and measured the shear force in two directions, the moment in two directions, and the axial force. Additional details of the cooling tower, its isolator/restraint system, and its performance during seismic testing may be found in Astroza et al. (2013c).

(a) (b)

Figure 2.9: Roof mounted equipment: (a) cooling tower (left) and penthouse (right) and (b) air handling unit. Arrows on slab indicate direction of input motion. Units: meters.

2.5 Data Collection

Performance of the building-NCS test specimen was documented using a broad array of strategies. These strategies included conventional analog sensors, a specially developed digital video camera array, a global positioning system (GPS), as well as a detailed post-shake physical inspection strategy coordinated with industry partners. Data from this experiment is publicly available online within NEEShub (Hutchinson et al., 2014). The archiving and navigation of this data are presented in Pantoli et al. (2013b, 2016b). A brief overview of the various data collection strategies is described below.

2.5.1 Sensor Array

In total, 516 acquisition channels were used for the sensors installed on the building during the seismic test phases. These analog sensors included accelerometers, displacement sensors (linear and string potentiometers), strain gauges, and load cells. Roughly two thirds of the analog sensors were installed on the NCSs, while the remaining one third were installed on the primary structural skeleton and the shake table platen. It is noted that the distribution of sensor channels was modified as needed during different tests (Pantoli et al., 2013b). The accelerometers used on the structure had an amplitude range of ±4 g, frequency range of DC–200 Hz and a wide dynamic range of 155dB. Although the major focus of the test was the behavior of NCSs, the installation of sensors on the primary structure and its components was necessary not only for understanding the behavior of the structural skeleton itself, but also because the structural response is considered the input motion for all of the nonstructural systems.

2.5.2 Digital Sensors: Video Cameras

A large networked video camera system was developed to assist with monitoring both the interior and exterior of the building-nonstructural test specimen. During each earthquake test, more than 80 cameras and up to five different types of cameras were utilized to monitor the performance of different components of the building. About 2/3 of the video cameras used during testing were network-ready and therefore broadcasted real-time video online to project partners around the world. Other cameras used during testing included high definition GoPro Hero2 cameras and camcorders, providing high-resolution videos of interior structural damage and overall exterior views, respectively.

2.5.3 Global Positioning System (GPS)

Displacement data obtained from double integration of acceleration measurements can be unreliable at low frequencies, whereas GPS data is unreliable at high frequencies because of the limited sampling. By co-locating GPS and accelerometer sensors, an optimal combination can be achieved to produce accurate and broadband velocity and displacement waveforms (Bock et al., 2011). In this test program, a total of six GPS stations were deployed; three stations were installed on the roof at the southwest, northwest and northeast corners, two stations were installed on the foundation at the southwest and northwest corners, and one static reference was placed within 50 m to the west of the building (off of the shake table).

2.6 Dynamic Test Protocol

2.6.1 Types of Input to the Building-NCS Test Specimen

A sequence of dynamic tests, including white noise, pulse and earthquake motions were input at the base of the specimen in the horizontal (east-west) direction using the shake table. In addition, ambient and forced vibration tests were conducted throughout the construction of the test building and during the base excitation testing phases for the purposes of system identification (Astroza et al., 2013a, b). In total, 13 earthquake motion tests, 31 low amplitude white noise base excitation tests and 45 pulse-like base excitation tests were conducted using the NEES@UCSD shake table while the building was in base isolated (BI) and fixed base (FB) configurations. The earthquake motion tests, which are the focus of this chapter, were conducted from April 16, 2012 to May 15, 2012. Shown in chronological order, Tables 2.4 and 2.5 summarize the test date, details of the source earthquake motion, scale factor, and a motion short name adopted for convenience in presentation. It is noted that with the exception of motion BI-4 and BI-7, all motions in the BI test phase (BI-1, 2/3, 5 and 6) were also imposed while the building was fixed at its base (FB-1 through FB-4).

The Chile and Peru records are actual recordings that were not frequency scaled nor spectrally matched. The Denali test motion was scaled in both frequency and amplitude (spectrally matched) to a targeted response spectrum with Site Class D soil conditions for the selected site. A 100% scale factor of the Denali motion implies that the test motion's response spectra matches the maximum target response spectra with ground motion parameter values of SMS = 2.10 g and SM1 = 1.43 g, whereas 67% scale of the motion means that the test motion has a response spectrum that was intended to match the design event response spectrum and impose the performance targets set for the building. Similarly, all of the Northridge earthquake test motions were spectrally matched to achieve about 20% of the target maximum spectrum, which is equivalent to a spectrum with a 43-year return period and Site Class D soil conditions.

Table 2.4: Summary of earthquake motion tests performed in the base isolated (BI) configuration.

Date	Earthquake Event – Site – Scaling (%)	Type1	Name2
April 16, 2012	1994 Northridge – Canoga Park – 100%	SM	BI-1:CNP100
	1994 Northridge – LA City Terrace – 100%	SM	BI-2:LAC100
April 17, 2012	1994 Northridge – LA City Terrace – 100%	SM	BI-3:LAC100
	2010 Maule (Chile) – San Pedro – 100%	AM	BI-4:SP100
April 26, 2012	2007 Pisco (Peru) – Ica – 50%	AM	BI-5: ICA50
April 27, 2012	2007 Pisco (Peru) – Ica – 100%	AM	BI-6: ICA100
	2007 Pisco (Peru) – Ica – 140%	AM	BI-7:ICA140

Notes: 1) SM=Spectrum matched motion; AM=Actual motion; 2) It is noted that the full name of the motion is preserved within Tables and Figures throughout; however, for brevity within the text only the sequential numbering are used (e.g. BI-1, BI-2, etc.)

Table 2.5: Summary of earthquake motion tests performed in the fixed base (FB) configuration.

Date	Earthquake Event – Site – Scaling (%)	Type[1]	Name[2]
May 7, 2012	1994 Northridge – Canoga Park – 100%	SM	FB-1:CNP100
May 9, 2012	1994 Northridge – LA City Terrace – 100%	SM	FB-2:LAC100
	2007 Pisco (Peru) – Ica – 50%	AM	FB-3:ICA50
May 11, 2012	2007 Pisco (Peru) – Ica – 100%	AM	FB-4:ICA100
May 15, 2012	2002 Denali– TAPS Pump Station #9 – 67%	SM	FB-5:DEN67
	2002 Denali– TAPS Pump Station #9 – 100%	SM	FB-6:DEN100

Notes: 1) SM=Spectrum matched motion; AM=Actual motion; 2) It is noted that the full name of the motion is preserved within Tables and Figures throughout; however, for brevity within the text only the sequential numbering are used (e.g. FB-1, FB-2, etc.)

The earthquake motions were selected to cover a wide range of characteristics including different frequency content as well as varied strong motion durations and amplitudes. Actual motions from the subduction zone of South America and seed motions from the coast of California and the central area of Alaska were chosen to represent these characteristics. The seismic motions were designed and applied to the building with the intent to progressively increase the seismic demand on the structure and NCSs in both the base isolated and fixed base configurations, while at the same time minimizing the development of damage to the specimen during the lower intensity motions. It should be noted that the nature of shake table testing control with large specimens does not permit exact matching between intended and achieved test motions. In this chapter, the achieved test motions are provided.

2.6.1.1 Earthquake Motions: Base Isolated Configuration

While the test building was in a base isolated configuration, two spectrally matched motions (Canoga Park and LA City Terrace, both from the 1994 M_w = 6.7 Northridge earthquake) and four actual earthquake motions (San Pedro from the 2010 M_w = 8.8 Maule-Chile earthquake and Ica amplitude scaled to 50%, 100% and 140%

from the 2007 $M_w = 8.0$ Pisco-Peru earthquake) were applied to the specimen. These motions were intended to impose minimal damage to the specimen so that the structural systems would not be damaged prior to fixed base testing. In addition, it was desirable to not exceed the 150% shear strain design limit of the isolators. For this reason, scale factors were selected with the guidance of pre-test numerical simulations, so that the maximum interstory drift ratio remained less than about 0.5% while the building was base isolated.

Figure 2.10 shows the input acceleration, velocity and displacement time histories measured at the shake table platen and Table 2.6 summarizes the peak acceleration, velocity, displacement, and strong motion duration defined by the time interval between 5-95% of the Arias intensity (Arias, 1970) for each of these achieved input motions. It is noted that the motions from the 2010 Maule-Chile and 2007 Pisco-Peru earthquakes were of substantially long duration, with their 5-95% duration of strong shaking estimated at more 4-5 times that of the Northridge motions. Figure 2.11 shows the 5% damped elastic displacement and pseudo-acceleration response spectra for the achieved table motions. Using the range of spectral accelerations from the elastic response spectra for 5% damping (0.09 – 0.29 g) and considering a predominant period of 2.5 s and an equivalent damping ratio of 12% (although the period and damping vary for different values of shear strain) for the combined structure-isolation system, the expected design displacement of the isolators ranges from 0.11 – 0.36 m (ASCE/SEI, 2010).

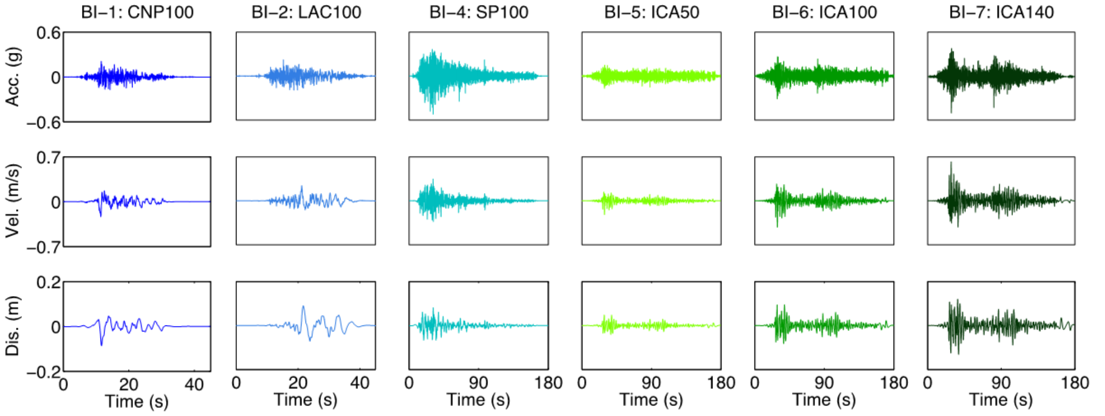

Figure 2.10: Time histories of achieved shake table motions applied to the base isolated building. Time axis for BI-1 to BI-2 formatted to 45 s and BI-4 to BI-7 formatted to 180 s. Note that positive displacement indicates eastward movement.

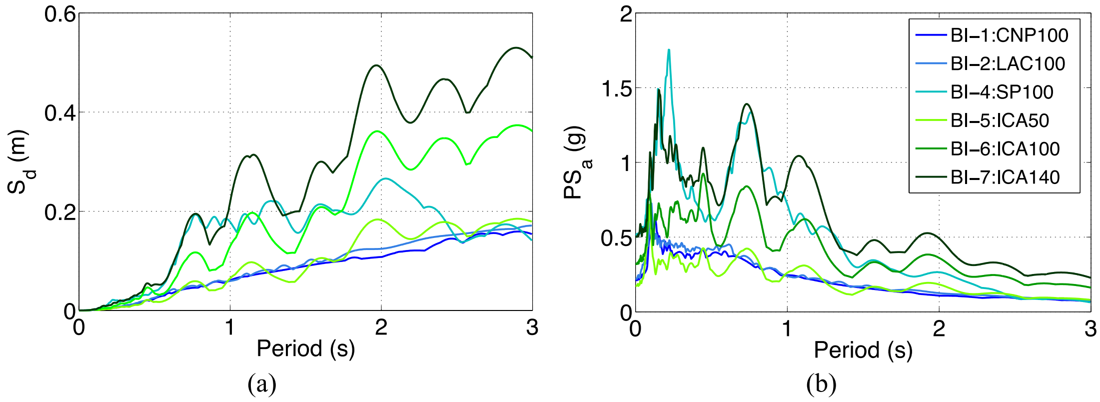

(a) (b)

Figure 2.11: (a) Overlaid displacement and (b) pseudo-acceleration elastic response spectra (ζ=5%) of shake table achieved motions applied to the base isolated building.

Table 2.6: Achieved peak input (ground) acceleration, velocity, displacements, duration of strong shaking and spectral acceleration at a period of 2.5 s of the motions applied while the building specimen was base isolated.

Motion	Peak input acceleration (g)	Peak input velocity (mm/s)	Peak input displacement (mm)	Strong motion duration (s)	Spectral acceleration at 2.5 s (g)
BI-1:CNP100	0.21	232.7	84.2	15	0.09
BI-2:LAC100	0.22	244.1	89.3	20	0.10
BI-3:LAC100	0.25	244.8	89.5	20	0.10
BI-4:SP100	0.52	348.7	82.7	80	0.09
BI-5:ICA50	0.17	223.2	47.6	130	0.11
BI-6:ICA100	0.32	425.9	94.6	128	0.21
BI-7:ICA140	0.50	625.9	129.2	97	0.29

2.6.1.2 Earthquake Motions: Fixed Base Configuration

While fixed to the shake table platen, four spectrally matched motions (Canoga Park and LA City Terrace, both originating from the 1994 M_w = 6.7 Northridge earthquake and Denali 67% and 100%, each from the 2002 M_w = 7.9 Denali-Alaska earthquake) and two actual motions (Ica 50% and 100% from the 2007 M_w = 8.0 Pisco-Peru earthquake) were applied to the specimen. Figure 2.12 shows the corresponding input (ground) acceleration, velocity and displacement time histories and Figure 2.13 shows the 5% damped elastic response spectra for the achieved table motions. Additionally, Table 2.7 summarizes the maximum peak acceleration, velocity, displacement, and strong motion duration of each achieved input motion. It is clear from the time histories that peak input accelerations increase in severity from around 0.2 g to 0.8 g and have a range of strong motion durations. Although the intensity of the motions from the 2002 Denali earthquake are much greater than from the 2007 Pisco-Peru earthquake, the strong motion duration of FB-5 and FB-6 are almost half that of FB-3 and FB-4.

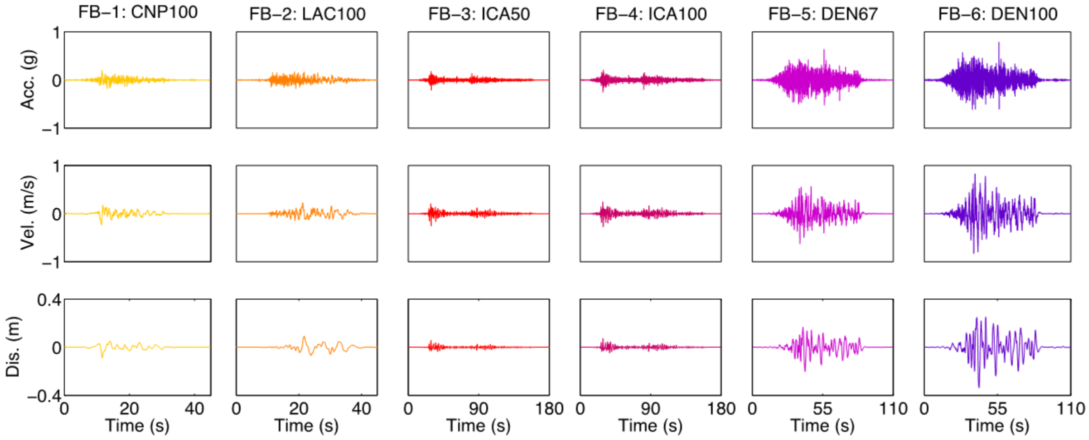

Figure 2.12: Time histories of achieved shake table motions applied to the fixed base building. Time axis for FB-1 to FB-2 formatted to 45 s, FB-3 to FB-4 formatted to 180 s, and FB-5 to FB-6 formatted to 110 s.

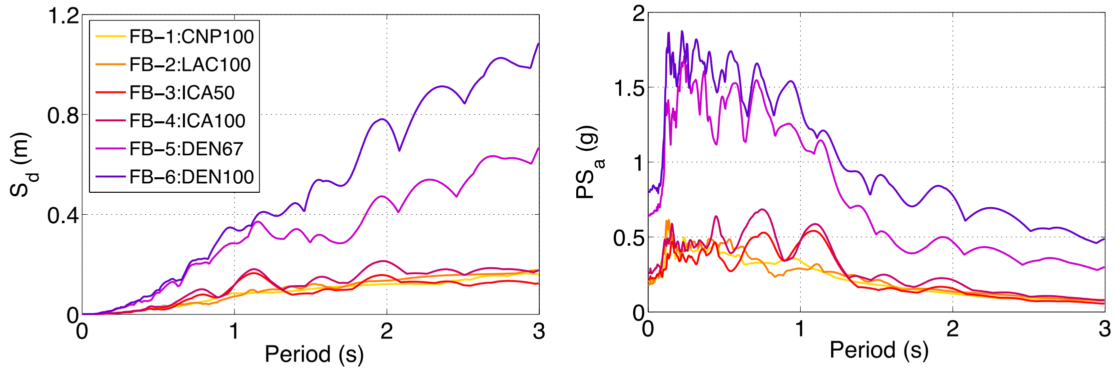

(a) (b)

Figure 2.13: (a) Overlaid displacement and (b) pseudo-acceleration elastic response spectra (ζ=5%) of shake table achieved motions applied to the fixed base building.

Table 2.7: Achieved peak input (ground) acceleration, velocity, displacements, duration of strong shaking, and spectral acceleration at periods of 0.2 s and 1.0 s of the motions applied while the building specimen was fixed at its base.

Motion	Peak input acceleration (g)	Peak input velocity (mm/s)	Peak input displacement (mm)	Strong motion duration (s)	Spectral acceleration at 0.2 s (g)	Spectral acceleration at 1.0 s (g)
FB-1: CNP100	0.21	235.0	87.8	15	0.42	0.34
FB-2: LAC100	0.18	230.5	93.1	20	0.42	0.29
FB-3: ICA50	0.21	262.2	58.3	91	0.35	0.48
FB-4: ICA100	0.26	284.9	73.2	96	0.46	0.48
FB-5: DEN67	0.64	637.4	200.6	49	1.50	1.10
FB-6: DEN100	0.80	835.7	336.2	49	1.60	1.40

2.7 Fundamental Period of Building-NCS Test Specimen

Using roof-to-ground undamped spectral ratios (Rosenblueth & Arciniega, 1992) found from test motion data, the predominant longitudinal periods (T_E) for the BI and FB building, prior to significant inelastic behavior, were obtained (Figure 2.14). For the final two BI motions, which both achieved high shear strains (> 100%), the predominant period of the building and BI system increased from about 2.5 s to 3.4 s, while the period found from ambient vibration prior to BI testing was about 0.85 s. Following the BI tests, the initial longitudinal period of the FB building obtained from ambient vibration was 0.52 s, with the partition walls and balloon framing contributing to about 25% of the building's stiffness (Astroza et al., 2013a). Prior to FB earthquake motion testing (after ambient vibration), a period of 0.74 s was obtained from low amplitude white noise base excitations (root mean square = 1.5% g) (Astroza et al., 2013d), indicating a significant decrease in stiffness (about 50% less than that found from ambient vibration) and the initiation of nonlinearity, possibly caused by partition wall and balloon framing slip as well as limited cracking of some structural elements. Based on the observed T_E of the building, the building's system stiffness had already been reduced to about 20% of its initial stiffness (obtained from ambient vibration) by the third FB motion.

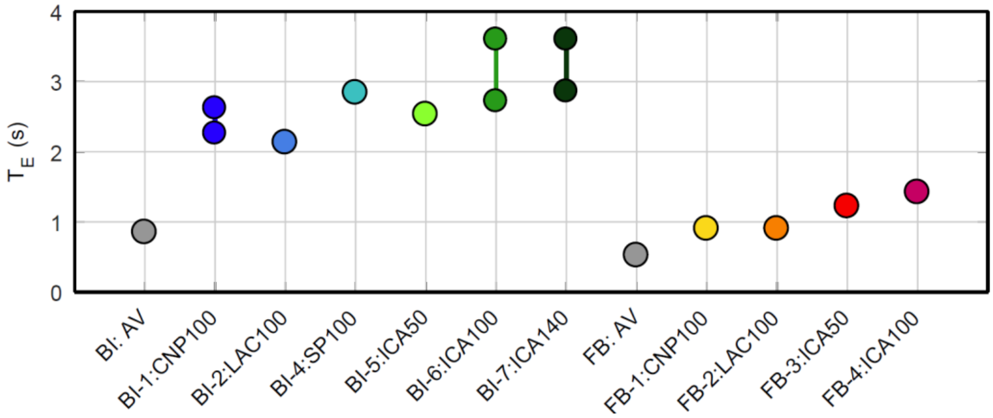

Figure 2.14: Variation of the building system's first longitudinal mode predominant period (T_E) during earthquake test motions and ambient vibration found using spectral ratios. Note AV = ambient vibration.

2.8 Seismic Test Results

In this chapter, presentation of test results from the seismic motion sequence focuses on the measured overall structural responses. Additional experimental results may be found in Pantoli et al. (2013a).

2.8.1 Peak Structural Responses

Raw acceleration measurements for all motions were filtered using a fourth-order bandpass Butterworth filter with corner frequencies of 0.08 and 25 Hz. Accelerations measured at the four corners of the building were double integrated to obtain floor level displacement histories and subsequently interstory drift was calculated as the difference of two averaged displacement histories between sequential floors. Interstory drift ratio, presented as a percentage, was then calculated by normalizing these values by the floor heights. Figure 2.15 shows the measured peak interstory drift ratios (PIDR) and peak floor accelerations (PFA), taken as the average of the four corners of the building. Both positive and negative values are presented to demonstrate the asymmetric demands imposed on the test building.

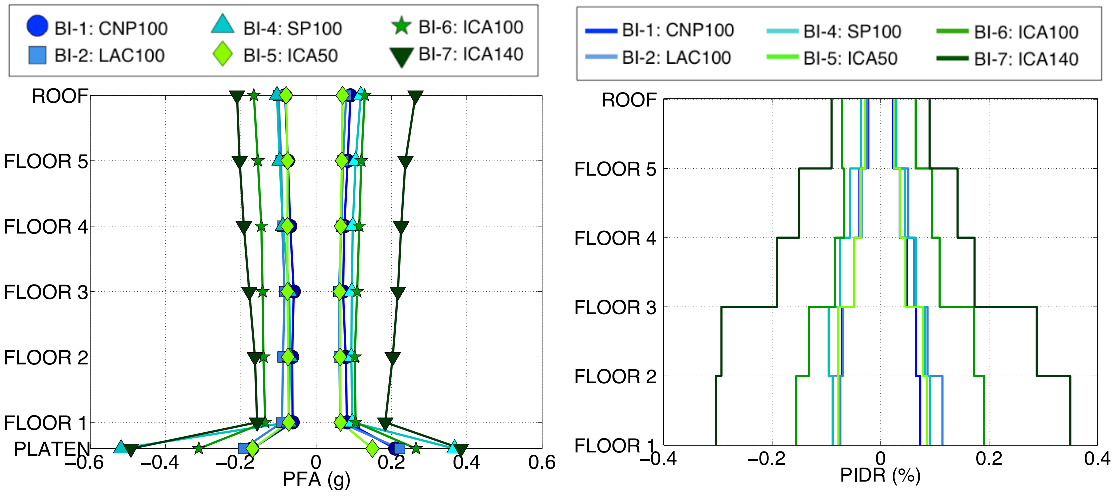

(a) (b)

Figure 2.15: (a) Peak floor acceleration (PFA) and (b) peak interstory drift ratio (PIDR) for the base isolated building-NCS test specimen. (Note: all responses are longitudinal, i.e. primary axis of shaking).

While isolated at its base, the building's longitudinal (shaking direction) PFAs were relatively constant up the height of the building. Simultaneously, input accelerations were dramatically attenuated by more than 50% (Figure 2.15a). Moreover, the building observed less than 0.4% interstory drift ratio (Figure 2.15b) along its primary shaking direction. Longitudinal shear strains, measured as the ratio of the relative horizontal displacement across the total height of the isolators to the height of the rubber in the base isolators, were as large as 157%, which corresponds to 325 mm of isolator displacement under the most intense, final motion BI-7 (Figure 2.16a). Approximately 90% of the total roof displacement relative to the shake table platen was concentrated in the isolators. It is noted that during each of the motions, the four isolators responded with approximately the same maximum longitudinal shear strain (Figure 2.16).

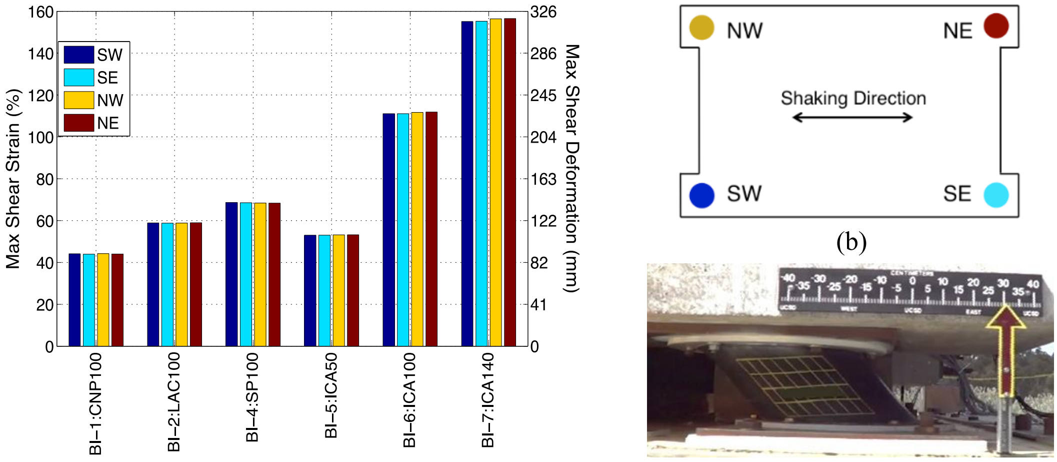

(a)

(b)

(c)

Figure 2.16: (a) Maximum longitudinal shear strain and deformation in each isolator for all base isolated motions and (b) schematic of isolator placement in plan view of the foundation and (c) image of deformed southeast isolator during BI-7. Note: NW = northwest, NE = northeast, SE = southeast, SW = southwest.

In contrast to the PFAs measured while the building was base isolated, the PFAs increased with increasing height from the base of the building and with each subsequent motion imposed during the test protocol while the building was fixed at its base (Figure 2.17a). During the FB testing phase, the largest floor level accelerations were consistently observed at the roof of the structure, with a maximum value of about 1.0 g, achieved during the targeted design event FB-5. The intense structural demands created softened lower stories, resulting in very large PIDRs approaching 6% during FB-6 (Figure 2.17b). With deformations concentrated predominantly within the lower stories, the PIDRs above level four remained below 2%. The PIDRs are plotted against the peak roof drift ratios, which were calculated as the peak roof displacement normalized by the height of the building above the foundation in Figure 2.18. This figure demonstrates that as the motion intensity increases, the PIDRs become increasingly larger than the peak roof drift ratios due to the nonlinearity of the building deformation. By the final FB motion, the PIDR is about twice the value of the peak roof drift ratio.

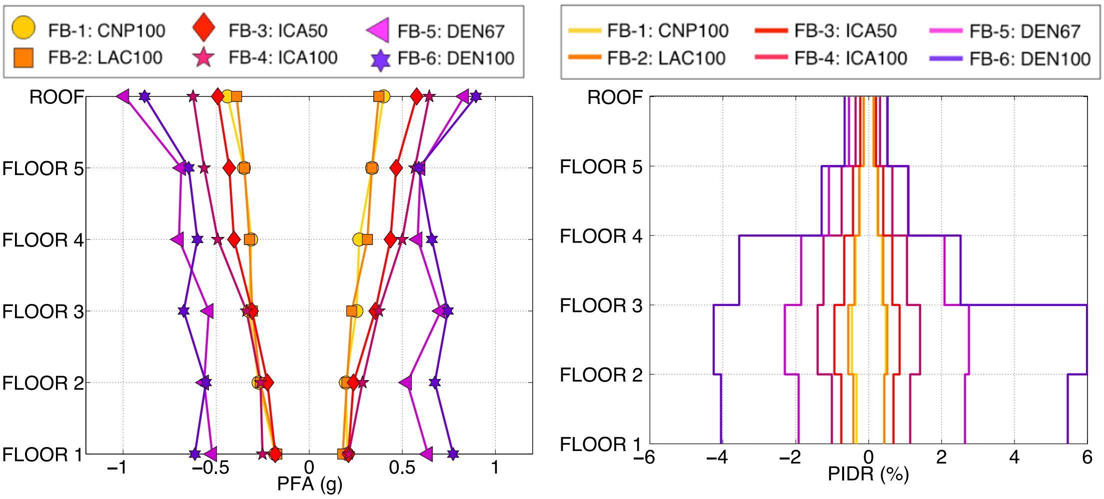

(a) (b)

Figure 2.17: (a) Peak floor acceleration (PFA) and (b) peak interstory drift ratio (PIDR) for the fixed base (FB) building-NCS test specimen. (Note: all responses are longitudinal, i.e. primary axis of shaking).

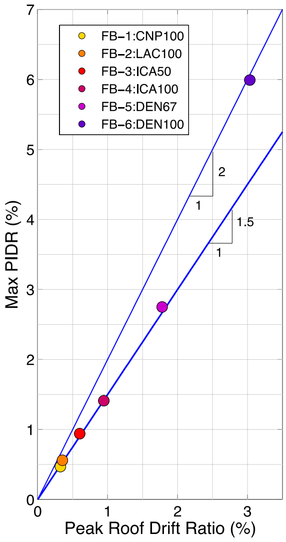

Figure 2.18: Max PIDR versus peak roof drift ratio for fixed base motions.

During the design event (FB-5), the largest PIDR values reaching 2.8% were concentrated at the lower levels (between floors 2-3), while the upper levels (above level 4) measured PIDRs less than about 2%. In contrast, test FB-6 resulted in the fracture of longitudinal rebar in the frame beams at the column faces on the north and south sides of the building (Figure 2.19a-f), leading to the development of an undesirable double story column side sway mechanism. By synchronizing various analog sensors with video capturing the third floor's interior beam column joint at the north side of the building, the bar fracture was determined to have occurred during a PIDR cycle with an amplitude of approximately 6%. Additionally, this time of fracture was observable in the form of acceleration and displacement spikes in nearby sensors as well as significant softening of the building. In addition, punching shear failure at the slab-column connections developed along with extensive cracking in the slabs on both floors two and three of the building, with cracking densely concentrated at the frame columns and extending outward (Figure 2.19g). Closely spaced flexural and shear cracks were observed along the lengths of the beams (Figure 2.19a and c) and concentrated at the ends of the beams, with the most severe beam cracking at the lower levels.

Synthesis of the peak demands imposed on the primary structure for the complete earthquake motion protocol is provided in Figure 2.20. This data is obtained by taking the maximum of the absolute values of the peaks of all floors using the data presented in Figures 2.15 and 2.17. This plot demonstrates the near linear-elastic response of the base isolated building, which was confirmed with physical observations made between the BI and FB testing phases. The nonlinear response, which cumulates while the building is fixed at its base, is also highly evident from the bend-over and progressive softening as the motion severity is increased. This data shows that the acceleration demand to the building saturated during the design event (FB-5) and was reduced by approximately 20% during the final very severe motion (FB-6) due to extensive cumulative damage and strength deterioration undergone by the building during the previous seismic tests.

From a design perspective, peak base shear demands are important in member sizing and detailing. Estimated floor weights and measured peak accelerations were used to calculate peak shear force demands distributed over the height of the building. Figure 2.21 shows these peak shear force values, normalized by the total weight of the building excluding the foundation (V_{max}/W_t, where $W_t = 4420$ kN), for each seismic motion while the building was in both the base isolated and fixed base configurations. As expected, larger normalized peak shear forces were observed in the building during the fixed base testing than in the base isolated testing. Peak base shear forces at the base of the first-floor columns/top of the foundation reached about 0.20 W_t for the base isolated building and 0.44 W_t for the fixed base building, which is much greater than 0.18 W_t, the expected peak base shear force for the fixed base building according to ASCE7-10. It is noted that in the base isolated configuration, shear imposed at the level of the isolator system reached 0.28 W_t (not shown in Figure 2.21). Assuming no higher modes contribute to the overturning moment, it can be concluded that about 90% of the maximum FB base shear is contributed to by the first mode. The saturation noted in the PFA distributions, while the building was fixed at its base, likewise emerges when studying the base shear force distributions (Figure 2.21b) as the positive envelope for motion FB-5 are of larger amplitude than those for motion FB-6.

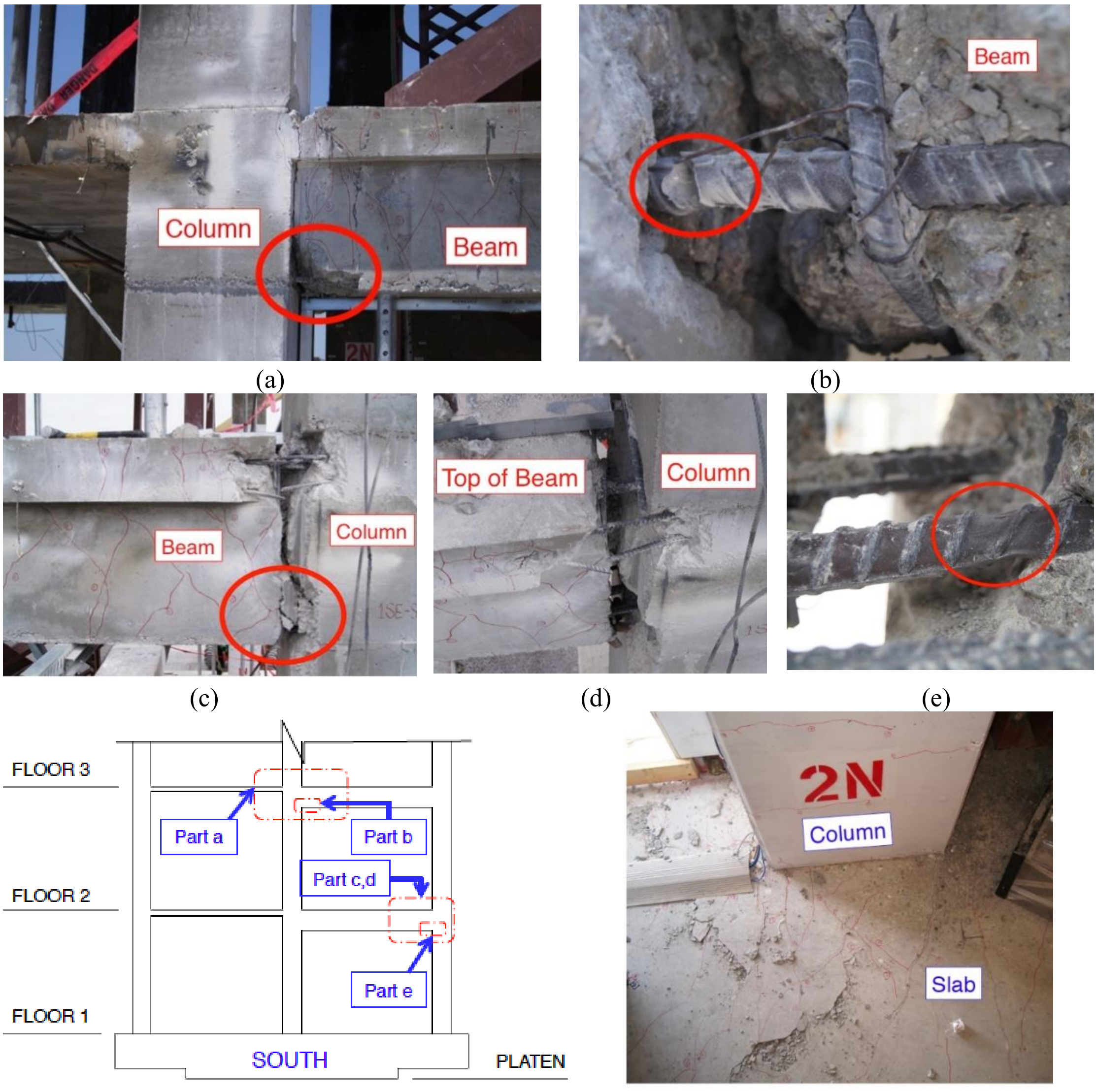

(f)

(g)

Figure 2.19: Photos from post-test deconstruction (a) south central column (b) close-up from part a: fractured long. reinforcement on floor 3 and (c,d) SE frame beam (e) close-up from part c: yielded (necked region) long. reinforcement on level two. (f) Map for parts a-e. (g) Cracking of slab at north central column on floor 2.

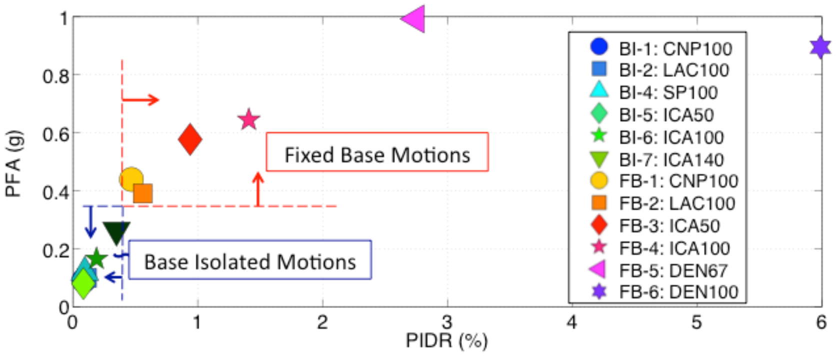

Figure 2.20: Peak floor acceleration versus peak interstory drift ratio for each seismic input motion.

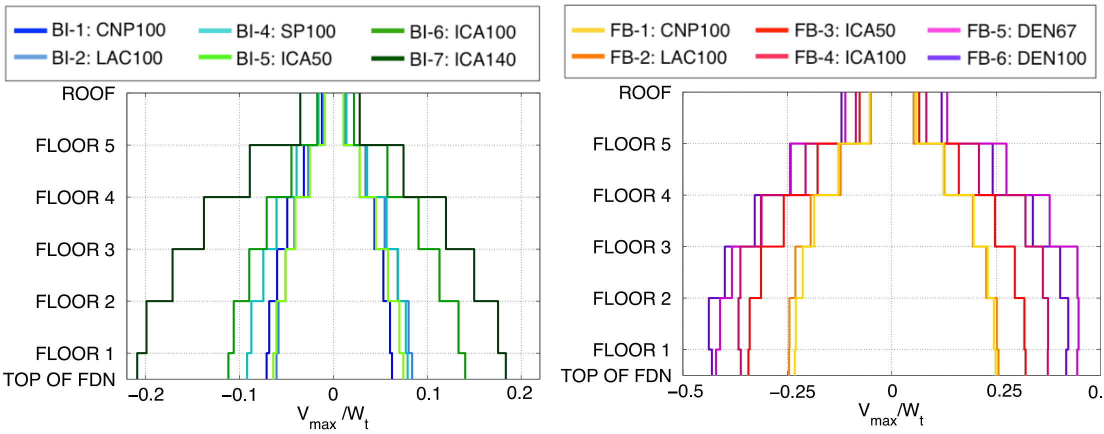

(a) (b)

Figure 2.21: Normalized peak story shear force distribution (V_{max}/W_t) over the height of the building for: (a) BI and (b) FB configurations. (Note: the x-axis scale varies between parts a and b). Note FDN = foundation.

2.8.2 Floor Response Spectra

Pseudo-acceleration floor response spectra for select BI and FB motions are shown in Figure 2.22. Overlaid BI and FB floor spectra for the platen and roof for target input motion ICA100 are shown in Figure 2.22a. In comparison to the BI roof response spectrum, peaks of the FB roof response spectrum occur at shorter periods, encompassing the range of periods in which most NCSs fall into (0.06 - 0.6 s). In the period range of interest, from 0.06 to 0.6 s, a peak acceleration of 1.3 g is expected for the FB building, while a peak acceleration of 0.3 g is expected for the BI building. A similar trend of larger peaks in the long period range for the BI building and larger peaks in the short period range for the FB building is observed in the largest amplitude BI motion and the FB motion where the performance objectives were achieved (FB-5; Figure 2.22b, c). Peak BI floor spectral accelerations of around 0.8 g were expected for the longer periods, while a peak of only about 0.5 g was expected for the 0.06 - 0.6 s NCS period range. In contrast, amplified peaks greater than 2 g were expected within the NCS period range on the third floor and roof of the FB building subjected to FB-5.

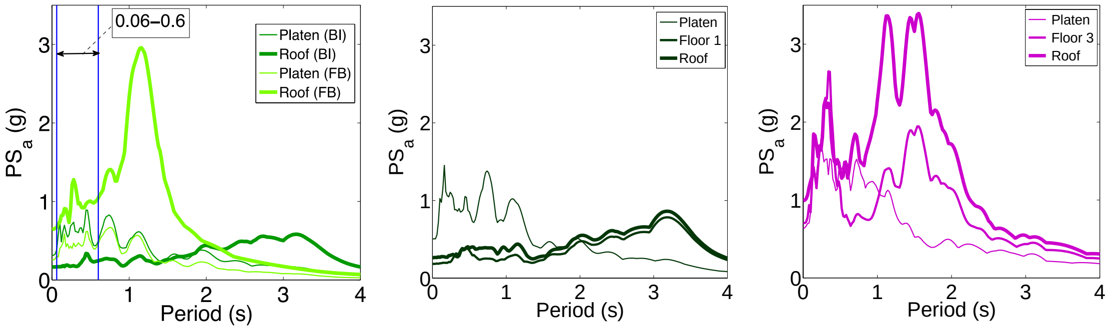

(a) (b) (c)

Figure 2.22: Achieved pseudo-acceleration elastic floor response spectra (ζ=5%) for (a) BI-6 and FB-4 with the estimated range of predominant NCS periods indicated with vertical lines, (b) BI-7, and (c) FB-5.

2.9 Conclusions

A full-scale five-story cast-in-place reinforced concrete building was constructed on the NEES@UCSD shake table. Unlike prior full-scale building shake table test programs, this experiment focused on investigating the interaction between structural and nonstructural systems during earthquakes. Therefore, the building was outfitted with a variety of nonstructural components and systems (NCSs) essential to supporting the operability of modern buildings with a range of occupancies. The building was subjected to a suite of earthquake motions while isolated at its base, and subsequently fixed to the shake table platen. Following two phases of seismic testing, post-earthquake live fire tests were conducted to evaluate the performance of fire protection systems and the impact of seismic damage in the building on the characteristics of fires. Within this chapter, the design and construction of the building, a detailed description of the NCSs, details of the seismic test protocol, and specific observations regarding the response of the primary structure of the test building to the earthquake motion suite were presented.

Conclusions from the base isolated seismic testing phase are consistent with prior investigations, and importantly demonstrate the benefits of using base isolation systems as a highly effective method for attenuating acceleration demands and therefore minimizing interstory drift ratios within building structures by shifting the fundamental period of the building. While isolated, the building responded with a fundamental period from about 2.5 – 3.4 s. In contrast, its fixed base predominant period, which was first measured as 0.52 s during ambient vibration, ranged from about 0.9 - 1.3 s during the first four test motions, indicating a significant loss in stiffness early in the fixed base test protocol. The four high damping rubber isolators utilized in the first phase of testing attained a maximum shear strain of almost 160% during the strongest motion. The building remained quasi linear-elastic throughout the base isolated testing phase, with peak floor accelerations relatively constant up the height of the building and reaching only 20 to 50% of the peak input accelerations. Peak interstory drift ratios also remained low, below 0.5%, while the fixed base building subjected to similar target input motions experienced close to a 1.5% peak interstory drift ratio and floor accelerations amplified more than two-fold. Importantly, while fixed at its base, performance objectives were met during the target design event, with measured floor accelerations of about 1.0 g at the roof level and PIDR reaching about 2.8% at the lower levels. Performance objectives were exceeded during the maximum intensity earthquake, with peak interstory drift ratios reaching about 6%. These extremely large interstory drift ratios are attributed to the severe damage which occurred in the lower beams of the special moment frames, which manifested into well-developed punching shear mechanisms at the slab-column regions and through-fracture of longitudinal reinforcing within frame beams pervasively observed in the two lowest floor levels of the test building resulting in the formation of a double story column side sway mechanism.

2.10 Acknowledgements

This project is a collaboration between four academic institutions (University of California, San Diego, San Diego State University, Howard University, and Worcester Polytechnic Institute), four government or granting agencies (the National Science Foundation, the Englekirk Advisory Board, the Charles Pankow Foundation, and the California Seismic Safety Commission), two oversight committees and over 40 industry partners from companies including: AGI, Armstrong, B.A.C, Brandow & Johnston, Cemco, Clark Pacific, Delco Sales, Baugrid, DASMA, 1st United Door Technologies, FM Global, Hilti, IBM, Klausbruckner and Associates, Mason Industries, Lawrence Doors, MMFX Technologies Corp., Omega Flex, Inc., Pacific Stair Corporation, PCI, QuakeHold, Regal Industries, Inc., Ruskin, Schindler Elevators, Square D/Schneider Electric, Sirve Seismic Protection Technologies, Seismic Isolation Engineering, Inc., Society of Fire Protection Engineers, Educational & Scientific Foundation, State Farm, Sure-Board, Timely Industries, USG Building Systems, Weir Minerals, Western Fire Protection, Inc., Willis Construction Co., Inc. A listing of industry project sponsors and committee members may be found on the project website: http://bncs.ucsd.edu/index.html. Funding is also provided by the NSF-NEESR program, grant number CMMI-0936505. The students who helped on the project are greatly appreciated: Consuelo Aranda, AJ Campanella, Elias Espino, Giovanni De Francesco, Jin-Kyung Kim, Diana Lin, Yujia Liu, Ceclia Luu, Steven Mintz (deceased), Yoshua Neuman, Hae-Jun Park, Francesco Selva, Christine Wittich and Richard Wood. We also express our thanks to Professor Brian Meacham, who was responsible for the fire tests and intimately involved in the planning and execution of the seismic tests as well. In addition, the technical support of NEES@UCSD and NEES@UCLA staff are greatly appreciated. Opinions and findings of this study are of the authors and do not necessarily reflect those of the sponsors.

The work in this chapter is published in Chen, M., Pantoli, E., Wang, X., Astroza, R., Ebrahimian, H., Hutchinson, T., Conte, J., Restrepo, J., Marin, C., Walsh, K., Bachman, R., Hoehler, M., Englekirk, R., and Faghihi, M. (2016). Full-scale structural and nonstructural building system performance during earthquakes: part I – specimen description, test protocol and structural response. *Earthquake Spectra, 32*(2), 737-770.

2.11 Appendix A: Structural Response

2.11.1 Base Isolated Building

The hysteretic normalized base shear-isolator shear strain response of the complete building-isolation system is shown in Figure 2.23: for the base isolated earthquake motions. The observed hysteretic response is consistent with the response of the bearings during quality control testing performed by the manufacturer. As the earthquake motions intensify and the peak shear strain increases, a decrease in effective stiffness is observed. As the isolation system reaches peak shear strains above 100%, the hardening behavior is observed. Figure 2.24 shows the hysteretic normalized shear force – roof drift ratio (roof displacement normalized by the height of the building above the foundation) response of the building above the isolation plane. The smoothness of the hysteretic response suggests minimal contributions from higher modes. The slight hysteresis visible in the final motion, BI-7, can be attributed to the onset of damage in the partition walls. The maximum and minimum peak base shear and overturning moments are indicated on the plot along with the time of occurrence, which are practically identical in both directions, indicating minimal relative movement of the building above the isolation plane.

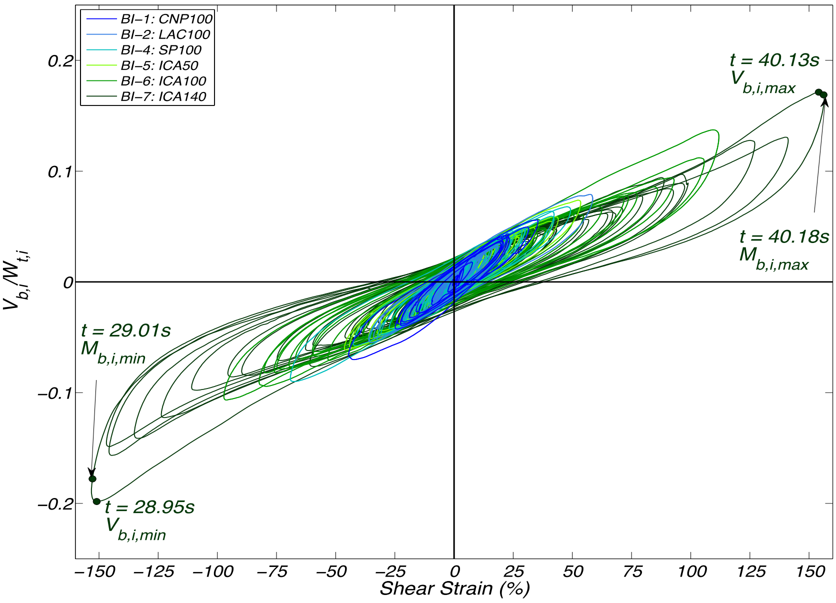

Figure 2.23: Normalized hysteretic base shear response of complete building-isolation system vs. average isolator shear strain for BI earthquake ground motions.

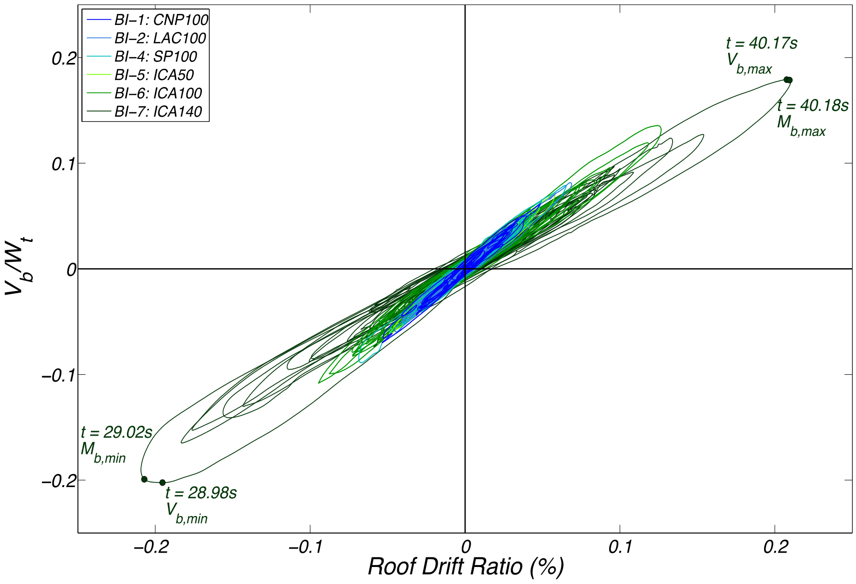

Figure 2.24: Normalized hysteretic base shear response of building above isolation plane vs. roof drift ratio for BI earthquake ground motions.

A snapshot of the story forces and story shears of the building are plotted in Figure 2.25 and Figure 2.26, respectively, at the time of peak maximum and minimum base shears, which shows that the forces are more or less uniform at each story. The ratio of the height above the foundation of the resultant of these forces to the roof height is also shown to be around 0.60-0.65 at the time of the peak base shears.

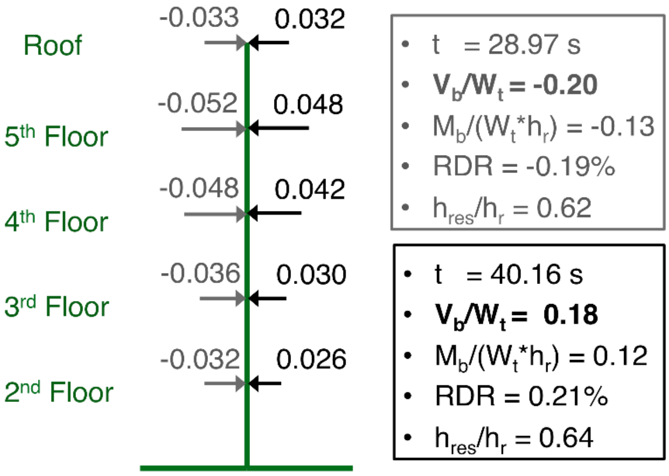

Figure 2.25: Snapshot of the story forces at the peak maximum and minimum base shears during BI-7.

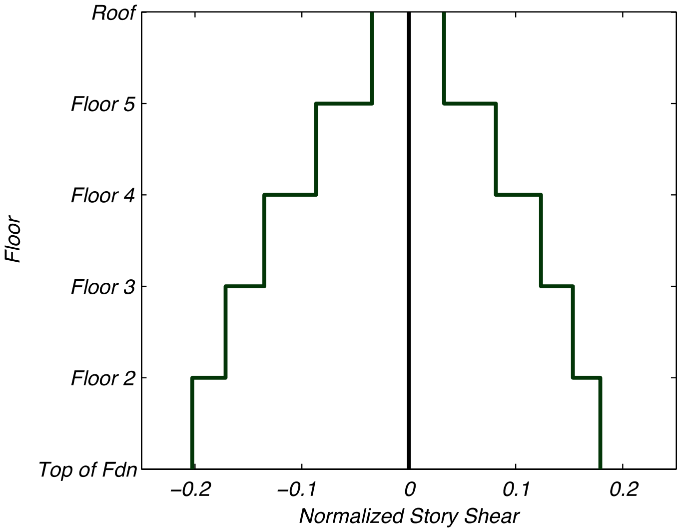

Figure 2.26: Snapshot of the story shears at the peak maximum and minimum base shears during BI-7.

The maximum peak floor accelerations for each ground motion are normalized by the peak ground (input) acceleration and plotted in Figure 2.27. This plot highlights how effective the isolators are at decreasing accelerations into the building, with foundation accelerations reaching only around 20-45% of the peak ground accelerations. The floor accelerations are also more or less uniform for each motion apart from BI-7, which shows some relative amplification from the foundation to the roof level due to the hardening of the isolators at the highest shear strains.

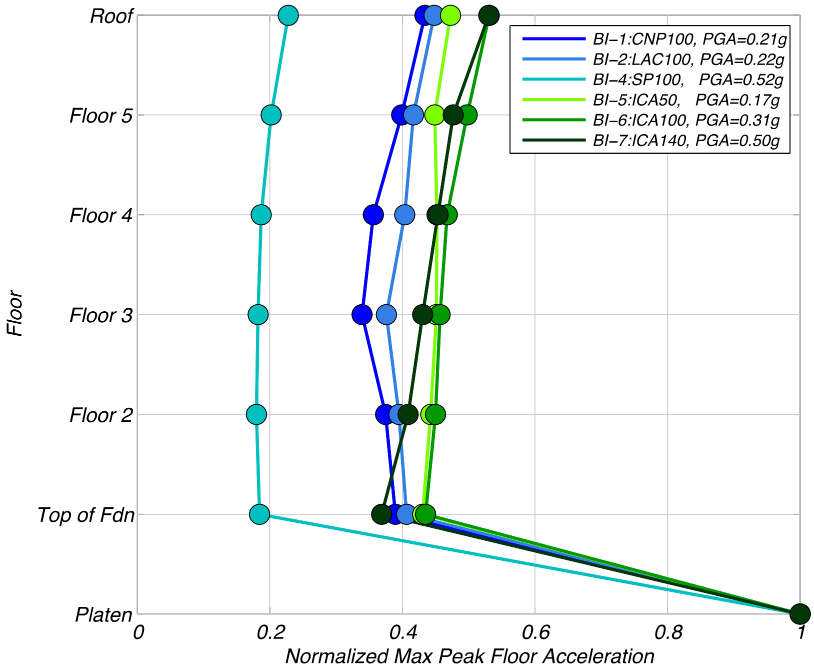

Figure 2.27: Maximum peak floor accelerations normalized by peak ground acceleration for BI earthquake ground motions.

Since the weight of the building is not evenly distributed, torsional effects were investigated. The difference between the accelerations recorded on the north side of the building and the south side of the building on each floor, evaluated at the time of the minimum and maximum total accelerations on each floor were found to be minimal, with a maximum of around 0.005g during the final motion and less than 0.0025 for all other motions. To further investigate the torsional influence, the peak interstory drifts were calculated for the north and south frames independently. The results from the north frame, plotted with solid lines, and the south side, plotted with dashed lines, are shown in Figure 2.28 and Figure 2.29 for the less intense and more intense motions, respectively. As observed from the minimal differences between the peak interstory drifts in the north and south frames, this also confirms that there is minimal torsion in the base isolated building. The isolator orbit is plotted for the southwest isolator during the most intense motion, BI-7, in Figure 2.30. While the peak shear strain in the longitudinal direction reached 150%, the peak shear strain in the transverse direction was less than 5%, also indicating minimal torsion.

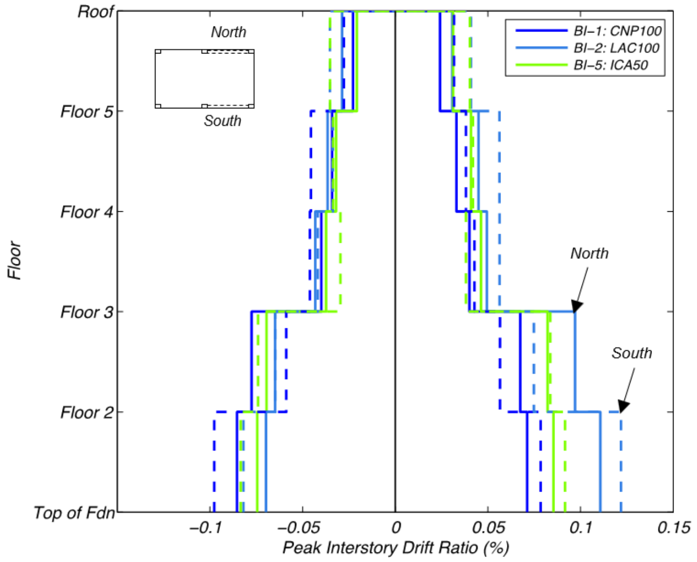

Figure 2.28: Peak interstory drift ratios of north and south frames for BI-1, BI-2 and BI-5.

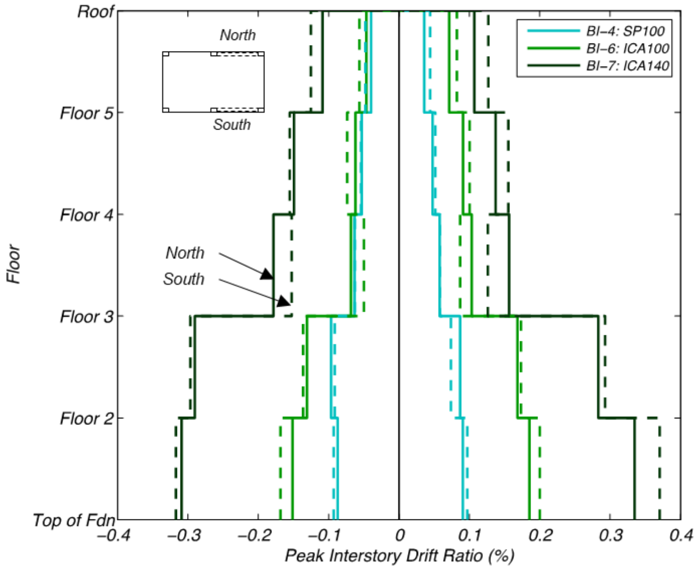

Figure 2.29: Peak interstory drift ratios of north and south frames for BI-4, BI-6 and BI-7.

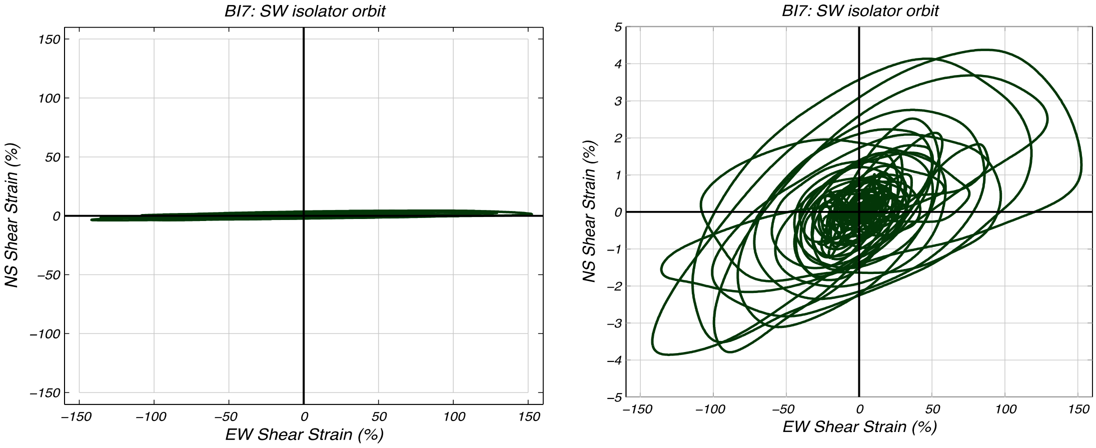

Figure 2.30: Orbit (NS vs EW shear strain) of SW isolator during BI-7.

The base isolated building roof drift ratio was disaggregated into the different contributing factors for BI-5, BI-6 and BI-7. The main contributing factors were identified as the isolator displacement itself, the rotation of the isolators, and the relative movement of the building above the isolation plane. These contributions are depicted in an exaggerated sketch in Figure 2.31. The shake table platen rotation was determined and found to have contributed to less than 0.3% of the total roof drift for all motions considered. The breakdown of the sources for the maximum and minimum roof drift ratios as well as a table listing the maximum and minimum roof drifts for the three base isolated motions considered is shown in Figure 2.32. For the three motions considered, about 90% of the roof drift is accounted for by the shear strain in the base isolator, about 7-9% occurs from the deformation of the moment frame, and 1-4% from the isolator rotations as the isolators compress and decompress axially.

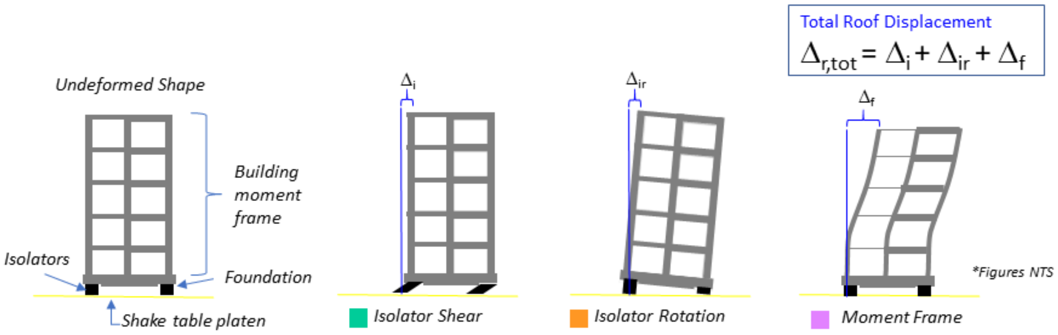

Figure 2.31: Illustration of main sources of roof drift.

BI-5: ICA50	max	121 mm
	min	-104 mm
BI-6: ICA100	max	253 mm
	min	-217 mm
BI-7: ICA140	max	361 mm
	min	-353 mm

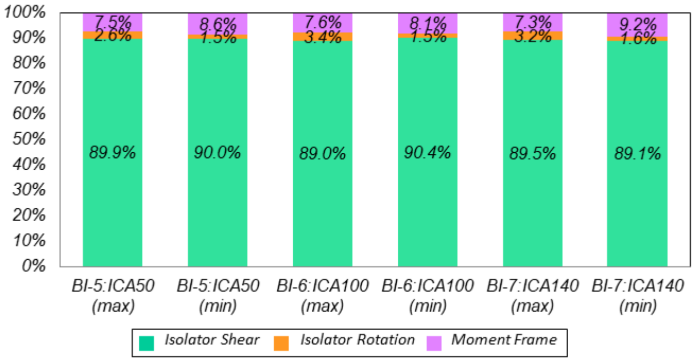

Figure 2.32: Breakdown of main sources of maximum and minimum roof drift ratio for BI-5, BI-6 and BI-7 and table listing maximum and minimum roof drifts.

The axial strains are found for each of the isolators for the most intense motions. The initial compression of the isolators (static strain) is approximated through the pressure recorded through the jacks when the building was lifted to remove the isolators between base isolation and fixed base configuration testing phases, with the vertical stiffness of the isolator given by the manufacturer. It is noted that the static strain found through the jacks is an approximate value due to the potential redistribution of the building weight since there were eight jacks in total (two at each corner of the building), and therefore the digital readings were connected to the pair of jacks at each corner. The dynamic transient axial strain, plotted against the shear strain in Figure 2.33 for each isolator for BI-6 and BI-7, is found through the linear potentiometers installed at the corners of the building to measure the vertical displacement of the foundation relative to the shake table platen. The accelerometers were not used for the vertical displacements due to the inaccuracy of the double integration method for small displacements.

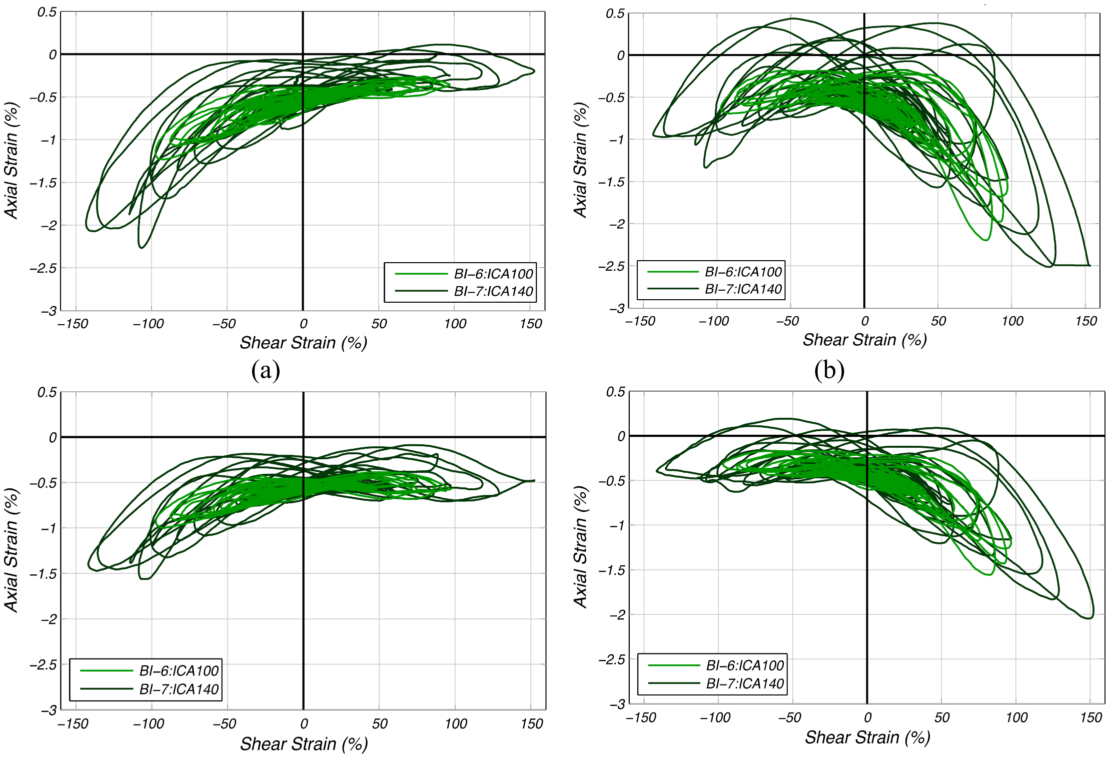

(a) (b)

(c) (d)

Figure 2.33: Axial strain vs. shear strain response during BI-6 and BI-7 for (a) northwest (b) northeast (c) southwest and (d) southeast isolators.

The axial force at mid-height of the isolator is plotted against the apparent axial strain for BI-5, BI-6 and BI-7 in Figure 2.34. The apparent axial strain is found through the linear potentiometers. The initial compression is subtracted from the axial strain, meaning that any value greater than zero represents an axial tension in the isolator and the values less than zero represent compression and decompression. It is assumed that the foundation is sufficiently rigid to spread the frame loads to the isolators at the corners of the building. It is also assumed that the point of inflection in the isolators is at mid-height and that it is time invariant. Isolator rotation is also assumed to be negligible. The axial force is found by taking the overturning moment in the north-south direction and the east-west direction about mid-height of the isolators, which includes the p-delta effects from relative displacements. This value is then divided by the distance between the isolators in the appropriate direction to obtain the axial forces. It is noted that the minimum axial forces for all isolators, seen prominently in BI-7, occur as the bearing approaches and departs from the position with zero axial force.

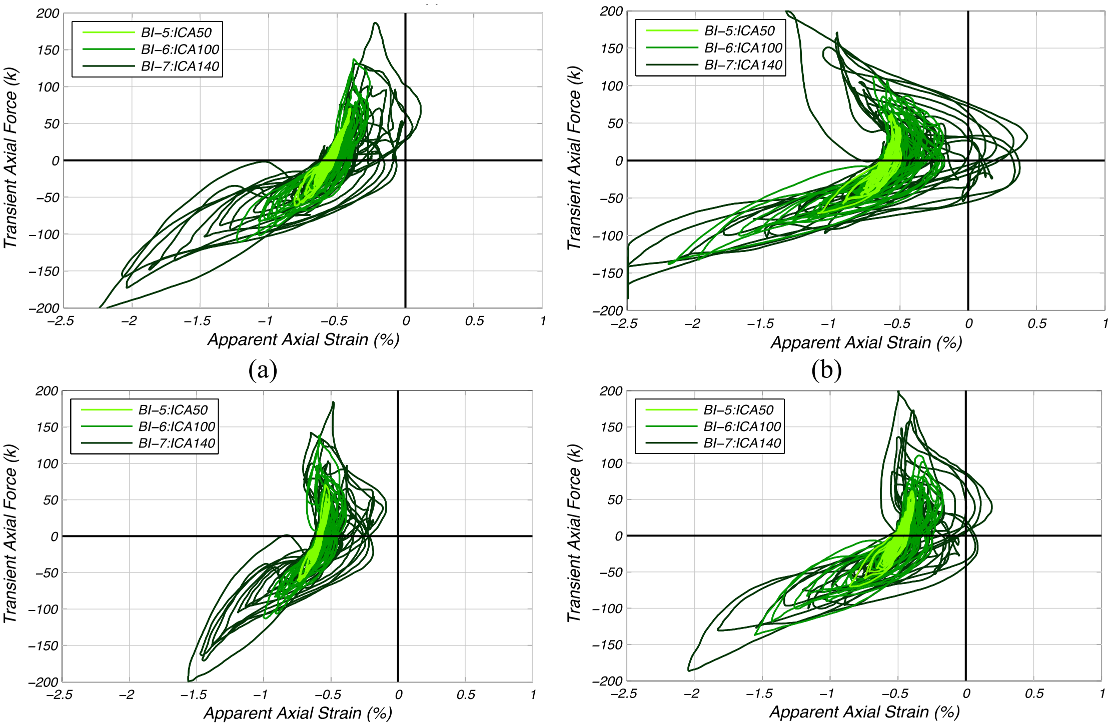

(a) (b)

(c) (d)

Figure 2.34: Transient axial force vs. apparent axial strain response during BI-5, BI-6 and BI-7 for (a) northwest (b) northeast (c) southwest and (d) southeast isolators.

2.11.2 Fixed Base Building

The normalized hysteretic base shears and normalized overturning moments are plotted against the roof drift ratios in Figure 2.35 and Figure 2.36, respectively, for all fixed base motions as well as the three initial white noise motions. The time at the peak positive and negative base shears and overturning moments are indicated on the plots for FB-5 and FB-6, in addition to the time at which a bar fracture in one of the frame beams occurred (denoted as t_{bf}). From the hysteretic base shear response at the higher intensity motions, it is observed that higher modes are contributing to the response from the lack of smoothness. It is also observed that there is a large jump in the response after the bar fractures, indicating the loss of strength, followed by a plateau in the response when the system is unable to regain that strength. From the hysteretic overturning moment response, the progressive loss of stiffness due to an accumulation of structural and nonstructural damage is evident as the effective slope of the response appears to decrease with each motion.

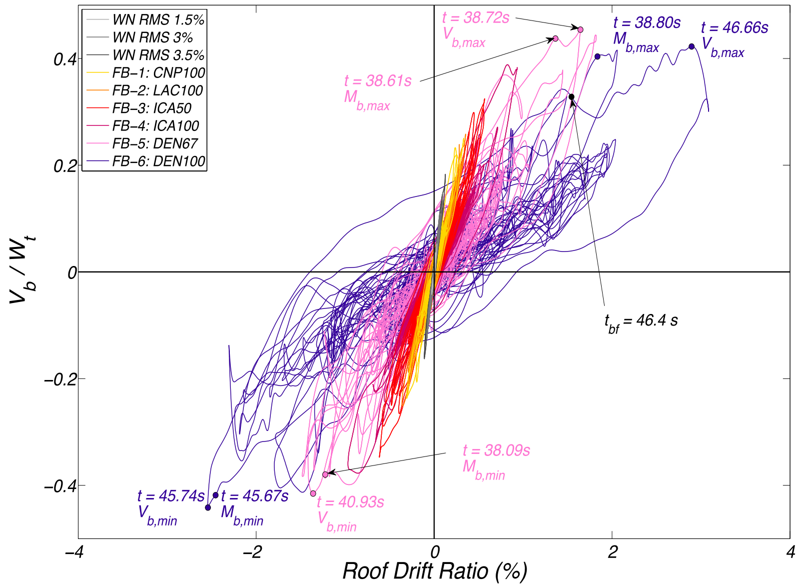

Figure 2.35: Normalized hysteretic shear force vs. roof drift ratio for FB earthquake ground motions and white noise input prior to FB-1.

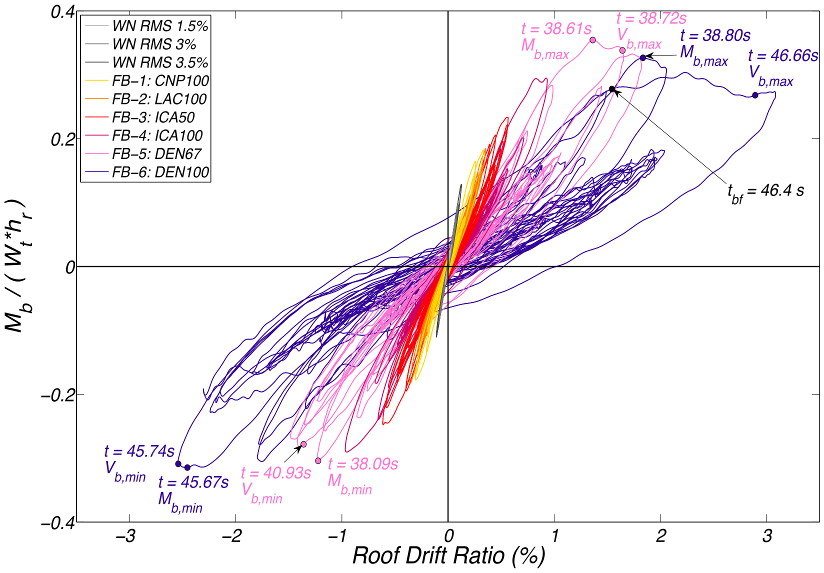

Figure 2.36: Normalized hysteretic overturning moment vs. roof drift ratio for FB earthquake ground motions and white noise input prior to FB-1.

The peak floor accelerations for the fixed base ground motions are normalized by the peak ground accelerations, listed in the legend for each motion, and shown in Figure 2.37. For the lower intensity motions, FB-1 to FB-4, there is significant floor acceleration amplification, with roof accelerations reaching about two to almost three times the peak ground acceleration. As the intensity increases with the final two motions when the building has highly nonlinear deformations, the floor acceleration amplification reduces due to a progressive loss of stiffness in the building.

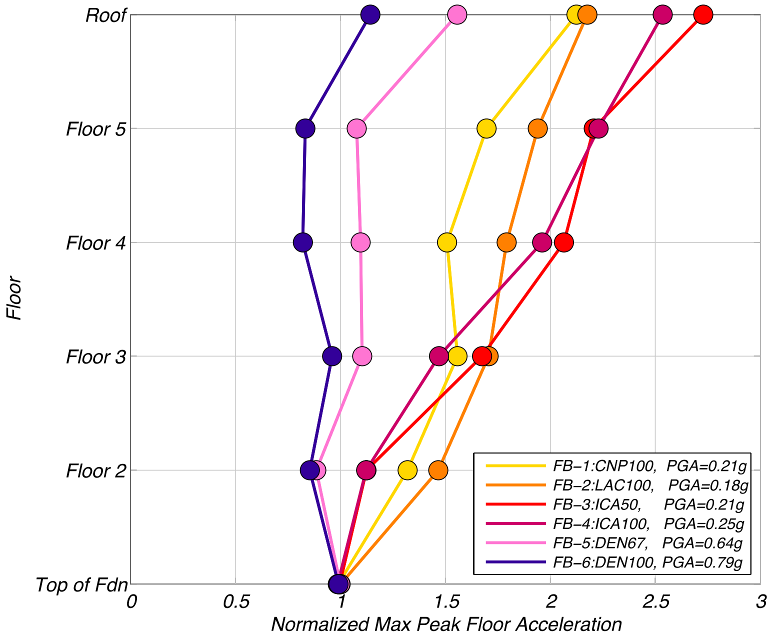

Figure 2.37: Maximum peak floor accelerations normalized by peak ground acceleration for FB earthquake ground motions.

To investigate the torsional effects, the difference between the accelerations in the north and south frame were determined for each floor at the time of the peak maximum and minimum floor accelerations for each ground motion. The acceleration differences remain less than 0.05 g for all motions except for the final motion, which reached almost 0.1 g at the third floor where the intermediate mechanism formed; indicating a large spike in torsion during this motion, compared to the response to lower intensity motions.

To investigate the torsional effects further, the peak interstory drift ratios were disaggregated between the north and south frames. The peak interstory drift ratios for the fixed base motions are shown in Figure 2.38 and Figure 2.39, for the less intense and more intense motions, respectively. For the first five motions, FB-1 to FB-5, there is a minimal difference between the north and south frames. There is, however, a large difference between the north and south frames in the final motion, FB-6, especially in the lower floors where the intermediate mechanism formed, indicating significant torsion during that motion.

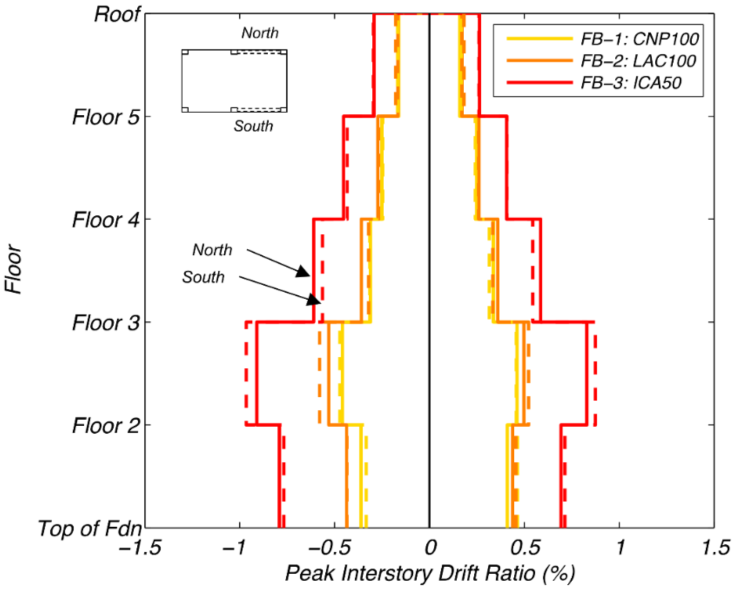

Figure 2.38: Peak interstory drift ratios of north and south frames for FB-1, FB-2 and FB-3.

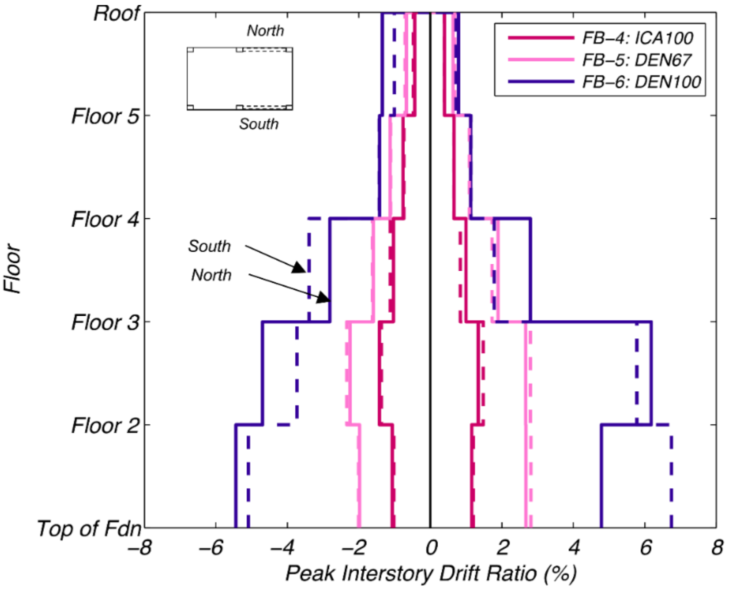

Figure 2.39: Peak interstory drift ratios of north and south frames for FB-4, FB-5 and FB-6.

2.12 References

American Concrete Institute (ACI) Committee 318. (2008). Building code requirements for structural concrete and commentary. *ACI 318-08*, Farmington Hills, MI.

American Concrete Institute (ACI) T1.2-03 ACI Innovation Task group 1 and collaborators. (2003). Special hybrid moment frames composed of discretely jointed precast and post-tensioned concrete members (ACI T1.2-03) and commentary (ACI T1.2R-03). *American Concrete Institute*, Farmington Hills, MI.

Arias, A. (1970). A measure of earthquake intensity. *Seismic Design for Nuclear Power Plants*, 23, 438-483.

ASCE/SEI. (2010). Minimum design loads for buildings and other structures. SEI/ASCE 7-10, *American Society of Civil Engineers*, Reston, VA.

Astroza, R., Ebrahimian, H., Conte, J.P., Restrepo, J.I., & Hutchinson, T.C. (2013a). Evolution of dynamic properties of a 5-story RC building during construction. *Topics in Dynamics of Civil Structures, Volume 4, Proceedings of the 31st IMAC, A Conference on Structural Dynamics.*

Astroza, R., Ebrahimian, H., Conte, J.P., Restrepo, J.I., & Hutchinson, T.C. (2013b). Statistical analysis of the identified modal properties of a 5-story RC seismically damaged building specimen. *Proceedings of the 11th International Conference on Structural Safety and Reliability (ICOSSAR'13).*

Astroza, R., Pantoli, E., Selva, F., Restrepo, J.I., Hutchinson, T.C., & Conte, J.P. (2013c). Full-scale structural and nonstructural building system performance during earthquakes and post-earthquake fire - Experimental evaluation of the seismic response of a roof-top mounted cooling tower. *Structural Systems Research Project Report Series, SSRP 13/14.* University of California San Diego, La Jolla, CA.

Astroza, R., Ebrahimian, H., Conte, J.P., Restrepo, J.I., & Hutchinson, T.C. (2013d). Modal identification of a 5-story RC building tested on the NEES-UCSD shake table. *Topics in Dynamics of Civil Structures, Volume 4, Proceedings of the 31st IMAC, A Conference on Structural Dynamics*.

Ayres, J. M., Sun, T. Y., & Brown, F. R. (1973). Nonstructural damage to buildings. *The Great Alaska Earthquake of 1964: Engineering, National Academy of Sciences*, Washington, D.C., 346–456.

BNCS Project Website (2014). Full-Scale Structural and Nonstructural Building System Performance During Earthquakes and Post-Earthquake Fire. <http://bncs.ucsd.edu/> [Accessed: January 20, 2014].

Bock, Y., Melgar, D., & Crowell, B. W. (2011). Real-time strong-motion broadband displacements from collocated GPS and accelerometers. *Bulletin of the Seismological Society of America, 101*(6), 2904-2925.

Chang, B. J., Hutchinson, T. C., & Englekirk, R. E. (2008). Experimental seismic performance evaluation of innovative beam-column subassemblies. *Structural Systems Research Project Report Series, SSRP 08/01*. University of California San Diego, La Jolla, CA.

Chang, B., Hutchinson, T., Wang, X., & Englekirk, R. (2013). Experimental seismic performance of beam-column subassemblies using ductile embeds. *ASCE J. Struct. Eng., 139*(9), 1555-1566.

Chen, M. C. Pantoli, E., Wang, X., Espino, E., Mintz, S., Conte, J., Hutchinson, T., Marin, C., Meacham, B., Restrepo, J., Walsh, K., Englekirk, R., Faghihi, M., & Hoehler, M. (2012). Design and construction of a full-scale 5-story base isolated building outfitted with nonstructural components for earthquake testing at the UCSD-NEES facility. *Proceedings, ASCE Structures Congress,* 1349-1360.

Chen, M. C., Pantoli, E., Wang, X., Astroza, R., Ebrahimian, H., Mintz, S., Hutchinson, T., Conte, J., Restrepo, J., Meacham, B., Kim, J., & Park, H. (2013a). BNCS report #1: full-scale structural and nonstructural building system performance during earthquakes and post-earthquake fire - specimen design, construction and test protocol. *Structural Systems Research Project Report Series, SSRP 13/9*. University of California San Diego, La Jolla, CA.

Chen, M. C., Pantoli, E., Wang, X., Mintz, S., Hutchinson, T., & Restrepo, J. (2013b). BNCS report #4: full-scale structural and nonstructural building system performance during earthquakes and post-earthquake fire – construction details and technical specifications of specific subsystems. *Structural Systems Research Project Report Series, SSRP 13/12*. University of California San Diego, La Jolla, CA.

CUREE. (2014). NEES Nonstructural. Simulation of the Seismic Performance of Nonstructural Components. http://www.nees-nonstructural.org. [Accessed: January 20, 2014].

Dao, N., Ryan, K., Sato, E., Okazaki, T., Mahin, S., Zahgi A., Kajiwara, K., & Matsumori, T. (2011). Experimental evaluation of an innovative isolation system for a lightweight steel moment frame building at E-Defense. *Proceedings, ASCE Structures Congress,* 2951-2962.

Ebrahimian, H., Astroza, R., Conte, J. P., Restrepo, J. I., & Hutchinson, T. C. (2013). Pre-test nonlinear FE modeling and simulation of a full-scale five-story reinforced concrete building. *Topics in Dynamics of Civil Structures, Volume 4, Proceedings of the 31st IMAC, A Conference on Structural Dynamics*.

Espino, E. (2012). *Case Study of Material Buffer Performance in a Construction Project.* Master of Science in Civil Engineering Thesis, San Diego State University, San Diego, CA.

FEMA E-74 (2012). Reducing the risks of nonstructural earthquake damage: a practical guide, fourth edition. *Applied Technology Council, for the Federal Emergency Management Agency*, Washington, D.C.

Filiatrault, A., Uang, C-M., Folz, B., Christopoulos, C., & Gatto, K. (2001). Reconnaissance report of the February 28, 2001 Nisqually (Seattle-Olympia) Earthquake. *Structural Systems Research Project Report No. SSRP-2000/15*, University of California, San Diego, La Jolla, CA.

Hoehler, M. S., Panagiotou, M., Restrepo, J. I., Silva, J. F., Floriani, L., Bourgund, U., & Gassner, H. (2009). Performance of suspended pipes and their anchorages during shake table testing of a seven-story building. *Earthquake Spectra, 25*(1), 71-91.

Hutchinson, T., Restrepo, J. I., Conte, J., & Meacham, B. (2013). Overview of the building nonstructural components and systems (BNCS) project. *Proceedings, Structures Congress 2013: Bridging Your Passion with Your Profession*, 1485-1498.

Hutchinson, T., Restrepo, J., Conte, J., Pantoli, E., Chen, M., Wang, X., Astroza, R., Ebrahimian, H. (2014). Shake table testing of a five story building outfitted with NCSs (BNCS project). Network for Earthquake Engineering Simulation (NEES) (distributor). Dataset. DOI: 10.4231/D38W38349. https://nees.org/warehouse/project/722

Kim, J. K., Meacham, B. J., & Park, H. (2013). Structural and nonstructural building system performance during earthquake and post-earthquake fire: fire test program. *Worcester Polytechnic Institute*, Worcester, MA.

Matsuoka, Y., Suita, K., Yamada, S., Shimada, Y., & Akazawa, M. (2008). Non-structural component performance in 4-story frame tested to collapse. *Proceedings, 14th World Conference on Earthquake Engineering*.

Mazzoni, S., McKenna, F., Scott, M. H., & Fenves, G. L. Open System for Engineering Simulation User-Command-Language Manual (version 2.0), Pacific Earthquake Engineering Research Center, University of California, Berkeley. <http://opensees.berkeley.edu/> [September 12, 2013].

Meacham, B. J., Kim, J. K., & Park, H. (2013). Shake table testing of a full-scale five-story building: post-earthquake fire performance. *Proceedings, ASCE Structures Congress*, 1499-1510.

Meneses et al., 2010. The El Mayor Cucapah, Baja California earthquake April 4, 2010. *An EERI Learning from Earthquakes Reconnaissance Report*, 2010/02.

Miranda, E. & Taghavi, S. (2003). Response assessment of nonstructural building elements. *PEER Report 2003/05*, 64-65.

Miranda, E., Mosqueda, G., Retamales, R., & Gokhan P. (2012). Performance of nonstructural components during the 27 February 2010 Chile Earthquake. *Earthquake Spectra, 28*(S1), S453-S471.

Ozcelik, O., Luco, J. E., Conte, J. P., Trombetti, T. L., & Restrepo, J. I. (2008). Experimental characterization, modeling and identification of the NEES-UCSD shake table mechanical system. *Earthquake Engineering & Structural Dynamics, 37*(2), 243-264.

Panagiotou, M., Restrepo, J. I., & Conte, J. P. (2011a). Shake-table test of a full-scale 7-story building slice. Phase I: Rectangular wall. *ASCE J. Struct. Eng., 137*(6), 691-704.

Panagiotou, M. & Restrepo, J. I. (2011b). Displacement-based method of analysis for regular reinforced-concrete wall buildings: Application to a full-scale 7-story building slice tested at UC-San Diego. *ASCE J. Struct. Eng., 137*(6), 677-690.

Pantoli, E., Chen, M. C., Wang, X., Astroza, R., Ebrahimian, H., Mintz, S., Hutchinson, T., Conte, J., Restrepo, J., Meacham, B., Kim, J., & Park, H. (2013a). BNCS Report #2: full-scale structural and nonstructural building system performance during earthquakes and post-earthquake fire - test results. *Structural Systems Research Project Report Series, SSRP 13/10*. University of California San Diego, La Jolla, CA.

Pantoli, E., Chen, M. C., Hutchinson, T., & Restrepo, J. (2013b). BNCS Report #3: full-scale structural and nonstructural building system performance during earthquakes and post-earthquake fire – camera and analog sensor details. *Structural Systems Research Project Report Series, SSRP 13/11*. University of California San Diego, La Jolla, CA.

Pantoli, E., Chen, M., Wang, X., Hutchinson, T., Meacham, B., & Kim, J. (2013c). Shake table testing of a full-scale five-story building: performance of the major nonstructural components – egress and façades. *Proceedings, ASCE Structures Congress*, 1447-1459.

Pantoli, E., Chen, M. C., Wang, X., Astroza, R., Ebrahimian, H., Hutchinson, T. C., Conte, J., Restrepo, J., Marin, C., Walsh, K.D., Bachman, R., Hoehler, M., Englekirk, R.E., & Faghihi, M. (2016a). Full-scale structural and nonstructural building system performance during earthquakes: Part II - NCS damage states. *Earthquake Spectra, 32*(2), 771-794.

Pantoli, E., Chen, M. C., Hutchinson, T., Astroza, R., Conte, J., Ebrahimian, H., Restrepo, J., & Wang, X. (2016b). Landmark dataset from the building nonstructural components and systems (BNCS) project. *Earthquake Spectra, 32*(2),1239-1259.

Park, H., Meacham, B. J., & Kim, J. K. (2014). Fire performance of full-scale building subjected to earthquake ground motion: fire test program and outcomes. *Proceedings, 11th International Symposium on Fire Safety Science, International Association for Fire Safety Science*.

Rosenblueth, E. & Arciniega, A. (1992). Response spectral ratios. *Earthquake Engineering & Structural Dynamics, 21*(6), 483-492.

Sato, E., Furukawa, S., Kakehi, A., & Nakashima, M. (2011). Full-scale shaking table test for examination of safety and functionality of base-isolated medical facilities. *Earthquake Engineering & Structural Dynamics, 40*(13), 1435-1453.

Singh, M. P. (1988). Seismic design of secondary systems. *Probabilistic Engineering Mechanics, 3*(3), 151-158.

Steinbrugge, K. V. & Schader, E. E. (1973). Earthquake damage and related statistics In San Fernando, California, earthquake of February 9, 1971. *National Oceanic and Atmospheric Administration*, *Washington D.C., 1A*, 709-713.

TNO DIANA (2010a). DIANA User's Manual, Element Library. Delft, The Netherlands.

TNO DIANA (2010b). DIANA User's Manual, Analysis Procedures. Delft, The Netherlands.

Van den Einde, L., Restrepo, J. I., Conte, J. P., Luco, E., Seible, F., Filiatrault, A., Clark, A., Johnson, A., Gram, Marty, Kusner, D., & Thoen, B. (2004). Development of the George E. Brown Jr. network for earthquake engineering simulation (NEES) large high performance outdoor shake table at the University of California, San Diego. *Proceedings of the 13th World Conference on Earthquake Engineering*.

Villaverde, R. (1997). Seismic design of secondary structures: state of the art. *Journal of Structural Engineering, 123*(8), 1011-1019.

Wang, X., Ebrahimian, H., Astroza, R., Conte, J., Restrepo, J., & Hutchinson, T. (2013). Shake table testing of a full-scale five-story building: pre-test simulation of the test building and development of a nonstructural components and systems design criteria. *Proceedings, ASCE Structures Congress*, 1460-1471.

Warcholik, G. & Priestley, M. (1998a). Structural systems research project: high strength concrete joints tests. *Report TR-98/01*. University of California, San Diego. La Jolla, CA.

Warcholik, G. & Priestley, M. (1998b). Structural systems research project: high strength concrete joints tests - series 3. *Report TR-98/12*. University of California, San Diego. La Jolla, CA.

Chapter 3

PREDOMINANT PERIOD AND EQUIVALENT VISCOUS DAMPING RATIO IDENTIFICATION FOR A FULL-SCALE BUILDING SHAKE TABLE TEST

3.1 Abstract

The predominant period and corresponding equivalent viscous damping ratio, also known in various loading codes as effective period and effective damping coefficient, are two important parameters employed in the seismic design of base isolated and conventional building structures. Accurate determination of these two parameters can reduce the uncertainty in the computation of lateral displacement demands and interstory drifts for a given seismic design spectrum. This chapter estimates these two parameters from data sets recorded from a full-scale five-story reinforced concrete building subjected to seismic base excitations of various intensities in a base isolated and fixed base configuration on the outdoor shake table at the University of California, San Diego. The scope of this chapter includes all test motions in which the yielding of the reinforcement has not occurred, and the response can still be considered “elastic”. The data sets are used with three system identification methods to determine the predominant period of response for each of the test configurations. One of the methods also determines the equivalent viscous damping ratio corresponding to the predominant period. It was

found that the predominant period of the fixed base building lengthened from 0.52 s to 1.30 s. This corresponded to a significant reduction in effective system stiffness to about 16% of the original stiffness. Then, a correlation between predominant period and peak ground velocity is established. Finally, the predominant periods and equivalent viscous damping ratios recommended by the ASCE 7-10 loading standard are compared with those determined from the test building.

3.2 Introduction

The predominant or effective period (T_E) of a building is used in seismic design of buildings to determine lateral forces, deflections, and interstory drifts. Some loading standards contain prescriptive requirements for calculating the predominant period of a building, or limiting it, when such period is determined from analysis. Determining a realistic predominant period is particularly challenging for reinforced concrete (RC) structures. Even if the building responds elastically, albeit nonlinearly, to the seismic excitation, the development of cracking in structural elements, loosening of building partitions, and or the nonlinearity in the soil foundation response results in nonlinear response, causing a decrease in the lateral stiffness and lengthening of the fundamental period, termed predominant period herein. The predominant period of a building is therefore, not uniquely defined, as it is earthquake intensity-dependent. In base isolated structures, the nonlinear response characteristics of the isolators also result in a dependency of the predominant period on earthquake intensity.

An under prediction of the predominant period may lead to an underestimation of lateral displacements and interstory drifts; and in base isolated structures, an underestimation of the seismic moat size. Observed building damage from past earthquakes (Miranda et al., 2012; Li & Mosalam, 2013; Baird et al., 2014) has indicated that the actual lateral building displacements are larger than expected, and therefore damage is seen in displacement-sensitive components such as stairs, partition walls, and other systems that are attached to multiple floors. To capture realistic earthquake responses and, particularly, lateral displacement demands in a simplified analysis, predominant periods should be estimated with some degree of accuracy.

In the past, the predominant period of buildings with the foundation fixed to the ground (i.e. without base isolation) has been found from data collected during seismic excitations using system identification methods, calibration of structural models, or a combination of both (Beck & Jennings, 1980; Cole et al., 1992; Çelebi et al., 1993; Marshall et al., 1994; Goel & Chopra, 1997; Nagarajaiah & Xiaohong, 2000; Trifunac et al., 2001; Rodriguez et al., 2006). For these buildings, the predominant periods calculated from recorded strong motion data are consistently greater than those calculated from low-level excitations such as ambient vibration (AV) or low-intensity forced vibrations on existing buildings (Goel & Chopra, 1997; Blume, 1935). Several factors have been speculated to be sources of period lengthening. For example, it was proposed that the lengthened period was due to interactions between structural and nonstructural components and systems (NCSs), or damage to the foundation or superstructure. Often, the lengthened period is concluded to be dependent on the input motion intensity (Çelebi et al., 1993; Trifunac et al., 2001; Ivanovic et al., 2000).

While state-of-the-art system identification methods can be applied to strong motion data, many well-established methods have utilized AV and low-level white noise (WN) base excitation test data to obtain modal properties, including the predominant period, which involve the underlying assumption of a linear dynamic system (Ji et al., 2011; Belleri et al., 2013; Moaveni et al., 2011; Astroza et al., 2015). Isolators installed under a base isolated (BI) building often have a high initial stiffness to prevent significant movement under low-level base excitations. For a fixed base (FB) building with light gauge steel partition walls, the effective system stiffness reduces as the gypsum board begins to slip relative to the steel studs (Restrepo & Bersofsky, 2011; Restrepo & Lang, 2011), and as cracking develops in the RC structural elements (Park & Paulay, 1975; Restrepo et al., 2006). These causes for reducing the stiffness, classified as recoverable stiffness, may not be detected through low-level excitations (i.e. existing cracks may not open, damaged walls may not overcome the initial frictions needed to slip, etc.), and therefore the predominant periods determined from AV will only elongate due to permanently degraded stiffness, but will not account for these phenomena.

Another parameter needed in seismic design is the equivalent viscous damping ratio (ζ_e) of the building. This ratio accounts for all sources of energy dissipation (including linear and nonlinear viscous, Coulomb friction, etc.), which are lumped into a single source. An approximation of ζ_e was first proposed by Jacobsen (1930, 1960) and is still used to approximate the equivalent viscous damping ratio of particular buildings or base isolators. An early example of finding a building's equivalent viscous damping ratio (Alford & Housner, 1953) was performed using a mechanical shaker on an existing building, which confirmed that the equivalent viscous damping ratio was not frequency-dependent and, therefore, indicating sources of energy dissipation other than viscous-type. Combining all damping terms into an equivalent viscous damping term was deemed acceptable as long as the damping value was low enough (Alford & Housner, 1953). In the spirit of simplicity, most loading codes prescribe 5% viscous damping ratio for all fixed base buildings, upon which all design response spectrum ordinates are based.

To obtain a suitable estimation of a building response using linear analysis, the period and equivalent viscous damping ratio should closely represent the values observed during ground motions below the intensity of the design earthquake, when no yielding of the reinforcement has occurred, and the response can still be considered elastic and be linearized. Therefore, it is valuable to use strong motion data when it is available to determine the predominant period of a building for both BI and FB configurations.

This chapter presents three different simplified system identification methods for determining the predominant period of a building, and one method to obtain the corresponding equivalent viscous damping ratio, using strong motion data. The first method uses transfer functions to characterize the building, which is a widely used standard for determining the predominant period of a building. The second method determines the predominant period through roof to ground spectral ratios. This method was first proposed by Rosenblueth and Arciniega for soils subjected to far field earthquakes. This method has been expanded to be applied to a building subjected to near fault and far field earthquakes. The third method optimizes the predominant period and equivalent viscous damping ratio by linearizing the building response and comparing the resulting response to the building’s displacement response obtained from GPS data. This method was inspired by the work first proposed by Beck and Jennings (1980). These methods are demonstrated through two case studies. Using the results, a correlation between the predominant period and peak ground velocity are determined, and the effective system stiffness of the FB building is derived.

3.3 Building Description and Test Program

To illustrate the different methods employed here for estimating the predominant period of a building, two case studies are analyzed, both drawn from the Building Nonstructural Components and Systems (BNCS) project, which consisted of a full-scale five-story RC building tested on the unidirectional NEES@UCSD shake table (Figure 3.1a,b). The almost 23-meter tall building consisted of a cast-in-place RC moment frame to support the structure and resist lateral loading. A complete set of NCSs was installed throughout the building to mimic a functional building system. Among the NCSs installed in the building were partition walls laid out in various configurations on each floor and an exterior façade composed of cold formed steel studs overlaid with gypsum board and finishing, which spanned from the bottom of the first floor to the top of the third floor. These NCSs provided additional stiffness to the building (Astroza et al., 2016) due to the connection points spanning vertically between floors and were anticipated to contribute to the system energy dissipation. A dense network of sensors, including accelerometers, a Global Positioning System (GPS), load cells, linear and string potentiometers, and strain gauges, was installed throughout the building to monitor the structural response. Details about the test program and building design are found in Chen et al. (2013, 2016).

Design for the BI building followed code requirements from the Chilean design for seismic isolation, NCh2745-2003, for a site in Chile, while design for the FB building was in accordance with performance-specific criteria for a site in downtown Los Angeles (Chen et al., 2013, 2016; LATBSDC, 2014; PEER, 2010). Similar to the seismic isolation requirements in ASCE 7-10, the NCh2745-2003 provides a guideline for design based on static analysis of the isolation system using effective isolator properties derived from prototype testing. A notable change in the building mass occurred during construction when a payload from the precast concrete façade was added. This additional mass changed the initial design parameters. A back-calculation of the seismic hazard parameters accounting for the added mass indicate that the design earthquake in ASCE 7-10 (2010) terms had $S_{d1} = 0.51g$ for the BI configuration and $S_{d1} = 0.98g$ for the fixed base configuration.

The fully-furnished building was tested first in a BI configuration, using four high-damping rubber isolators; each had a 650 mm outer diameter with a 100 mm diameter hollow core, a total height of 303 mm, and a total rubber height of 204 mm (Figure 3.1c). Prototype testing of the individual isolators showed a reduction in secant stiffness from 25% to 100% shear strain followed by almost constant secant stiffness up to 150% shear strain, see Figure 3.2. Secant stiffness, or effective stiffness k_{eff}, is defined as the difference between the peak positive force (F^+) and the peak negative force (F^-), divided by the difference between the peak positive displacement (Δ^+) and the peak negative displacement (Δ^-), as denoted for a sample loop in Figure 3.2. The equivalent viscous damping ratios are computed with Jacobsen's method (1930, 1960), and reproduced here using notation from ASCE 7-10 (2010):

$$\zeta_e = \frac{2}{\pi} \frac{E_{loop}}{k_{eff}(|\Delta^+|+|\Delta^-|)^2} \tag{3.1}$$

where E_{loop} is the hysteretic loop area, or the energy dissipated per cycle. The computed ζ_e values reduced from an average of 18.5% at a shear strain of 25% to 11% at a shear strain of 150%, see Figure 3.2.

Upon completion of the tests in the base isolated configuration, the base isolators were removed, and the building was clamped down to the shake table platen using post-tensioning rods, thus emulating a FB condition. The building corresponding to the BI configuration refers to the complete building-isolation system, in which the input, or ground motion, is imparted by the shake table platen. The input motion for the FB building, however, refers to the response of the first floor; that is, the top of the foundation, which is practically identical to that recorded on the shake table platen. Hereafter, the ground level will refer to the top of the shake table platen for the BI case study, and to the top of the foundation for the FB case study.

The test protocol consisted of six different earthquake input ground motions applied to the building for both base configurations (Chen et al., 2013, 2016). Between earthquake tests, low-amplitude WN base excitation and AV tests were conducted (Astroza et al., 2015). The test protocols, including the achieved peak ground (input) acceleration and velocity (PGA and PGV), as well as the spectral displacements at 2.0 s and 3.15 s ($S_{d2.0}$ and $S_{d3.15}$) for the BI building and spectral displacements at 0.72 s, 1.1 s, and 1.42 s ($S_{d0.72}$, $S_{d1.1}$ and $S_{d1.42}$) for the FB building, are shown in Tables 3.1 and 3.2 for the BI and FB configurations, respectively. Periods of 2.0 s and 3.15 s were the lowest and highest periods calculated for the BI building, as discussed later. A period of 0.72 s corresponds to that calculated for the FB building according to ASCE 7-10 (2010), and a period of 1.42 s was the highest period calculated for the FB building. Note that the spectral displacements listed in Tables 3.1 and 3.2 were computed for the equivalent viscous damping ratios assumed in design of the building for the design earthquake: ζ = 12% for the BI configuration and ζ = 5% for the FB configuration.

Table 3.3 summarizes the peak recorded structural response parameters for each test, including the peak foundation acceleration, peak average isolator shear strain and peak average shear strain rate for the BI configuration, the peak roof drift ratio for the

FB configuration, defined by normalizing the peak roof displacement relative to the base by the roof height (20.83 m to the center of mass), as well as the peak roof acceleration, and peak interstory drift ratio for both BI and FB configurations. The average isolator shear strains are defined as the displacement of the foundation relative to the shake table platen normalized by the total rubber height of an isolator. These values were found using data from GPS stations on the foundation level and data from Temposonics displacement sensors attached to the actuators below the platen, and differ only slightly from values inferred from accelerometer data (Chen et al., 2013).

The spectral displacement graphs for the achieved input ground motions recorded during testing in the BI and FB configurations are shown in Figure 3.3, together with the period range of interest displayed on the graph. For the BI configuration, the displacement response spectra for tests motions BI1, BI2, BI3 and BI5 were similar in the period range of interest. For these tests, the spectral displacement generally increases with period within this range. Test motion BI4 had greater spectral displacements than those in test motions BI1, BI2, BI3 and BI5 over the entire period range of interest, but contrary to the spectral displacement trend in these three test motions, the spectral displacement of test motion BI4 generally decreases with an increase in period. Test motions BI6 and BI4 had similar spectral displacements at the beginning of the period range of interest, but because in test motion BI5 the spectral displacements tended to increase with an increase in period, the spectral displacements at the end of the period range of interest for these two test motions were significantly different. The spectral displacements of test motion BI7 were approximately 140% those of test motion BI6 in the range of periods of interest. For the FB configuration, test motions FB1 and FB2 had similar displacement response spectra in the region of interest. For these two motions spectral displacements generally increased with an increase in period. Test motions FB3 and FB4, as reproduced by the shake table, exhibited similar spectral displacements in the range of periods between 0.72 s and 1.3 s. These two motions exhibit a distinct spectral displacement peak at 1.1 s. At 1.4 s, test motion FB3 had the smallest spectral displacement of all the four test motions whereas test motion FB4 had the largest spectral displacement. In all the test motions, but FB2, PGV and the maximum spectral displacement in the period range of interest correlate well. This means that an increase in PGV over that in a previous test, results in increased peak spectral displacement in the range. PGV will be used as an intensity measure later in this chapter. In test motions BI1 through BI7 and FB1 through FB4, the longitudinal reinforcement in the moment frame remained elastic as verified through strain gauges installed on top and bottom beam rebar as well as curvature potentiometers on critical elements (Pantoli et al., 2013). There were two additional motions that took the FB structure well into the inelastic range that are not considered in this chapter (Chen et al., 2013, 2016).

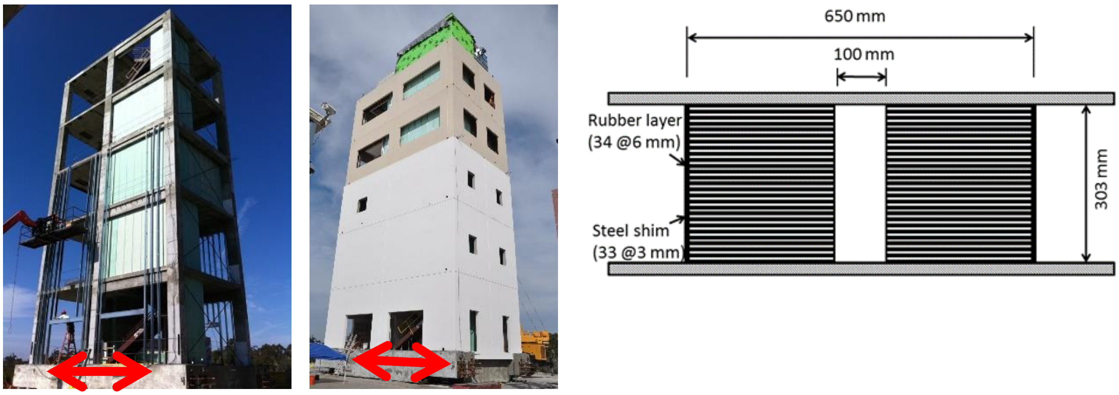

(a) (b) (c)

Figure 3.1: BNCS building on UCSD's outdoor shake table with arrow indicating direction of motion (a) during construction (b) with façade and (c) isolator dimensions.

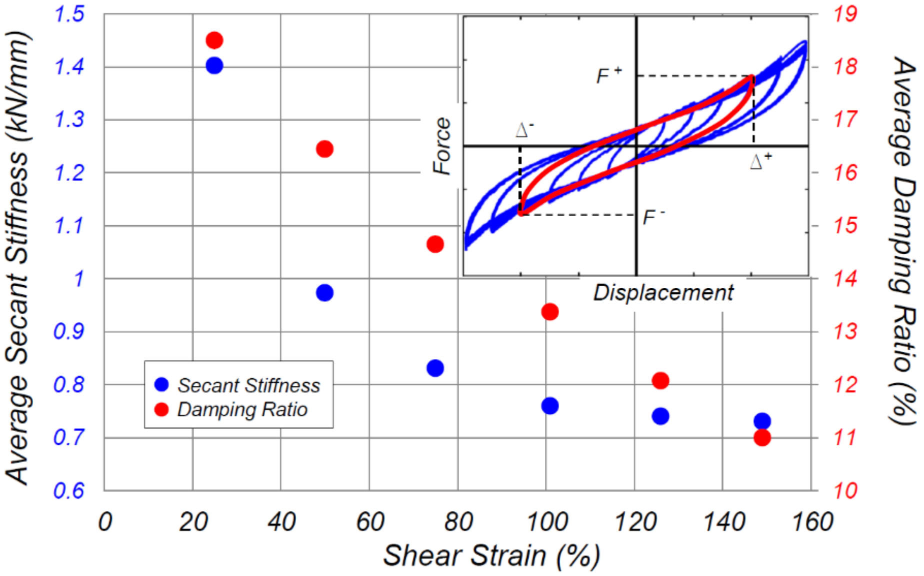

Figure 3.2: Prototype test results: average secant stiffness and damping ratio vs. shear strain with sample hysteretic responses for one isolator shown as inset.

Table 3.1: Summary of earthquake motion tests performed in the base isolated (BI) configuration (PGA/PGV/S_d are from the "as measured" motion during testing. ζ=12%* for S_d values).

Earthquake Event – Site – Scaling (%)	Test Motion Name (Abbreviated)	PGA (g)	PGV (m/s)	$S_{d2.00}$ (m)	$S_{d3.15}$ (m)
1994 Northridge – Canoga Park – 100%	BI-1:CNP100 (BI1)	0.210	0.234	0.091	0.11
1994 Northridge – LA City Terrace – 100%	BI-2:LAC100 (BI2)	0.223	0.243	0.10	0.13
1994 Northridge – LA City Terrace – 100%	BI-3:LAC100 (BI3)	0.250	0.245	0.10	0.13
2010 Maule (Chile) – San Pedro – 100%	BI-4:SP100 (BI4)	0.520	0.347	0.19	0.13
2007 Pisco (Perú) – Ica – 50%	BI-5: ICA50 (BI5)	0.169	0.220	0.11	0.12
2007 Pisco (Perú) – Ica – 100%	BI-6: ICA100 (BI6)	0.311	0.420	0.21	0.23
2007 Pisco (Perú) – Ica – 140%	BI-7:ICA140 (BI7)	0.498	0.621	0.29	0.33

* Note: ζ=12% was used in the design of the base isolated building for the design earthquake.

Table 3.2: Summary of earthquake motion tests performed in the fixed base (FB) configuration (PGA/PGV/S_d are from the "as measured" motion during testing. ζ=5%* for S_d values).

Earthquake Event – Site – Scaling (%)	Test Motion Name (Abbreviated)	PGA (g)	PGV (m/s)	$S_{d0.72}$ (m)	$S_{d1.13}$ (m)	$S_{d1.42}$ (m)
1994 Northridge – Canoga Park – 100%	FB-1:CNP100 (FB1)	0.207	0.236	0.041	0.086	0.095
1994 Northridge – LA City Terrace – 100%	FB-2:LAC100 (FB2)	0.179	0.228	0.044	0.097	0.10
2007 Pisco (Perú) – Ica – 50%	FB-3:ICA50 (FB3)	0.211	0.258	0.064	0.16	0.081
2007 Pisco (Perú) – Ica – 100%	FB-4:ICA100 (FB4)	0.254	0.277	0.084	0.18	0.11

* Note: ζ=5% was used in the design of the fixed base building for the design earthquake.

Table 3.3: Summary of recorded peak engineering response parameters for BI and FB configuration.

BI Configuration						
Test	PFA (g)	PRA (g)	PIDR (%)	PFV (m/s)	γ (%)	γ_{rate} (%/s)
BI1	0.0818	0.0912	0.089	0.268	46	178
BI2	0.0904	0.0997	0.11	0.297	59	149
BI3	0.0940	0.103	0.12	0.300	64	146
BI4	0.0959	0.119	0.091	0.261	69	291
BI5	0.0725	0.0796	0.086	0.238	51	170
BI6	0.135	0.165	0.19	0.399	105	252
BI7	0.183	0.264	0.34	0.599	155	455

FB Configuration				
Test	PRA (g)	RDR (%)	PIDR (%)	$\frac{\text{PIDR}}{\text{RDR}}$
FB1	0.439	0.34	0.47	1.4
FB2	0.390	0.36	0.56	1.5
FB3	0.577	0.64	0.94	1.5
FB4	0.644	1.0	1.4	1.4

Note: PFA = Peak Foundation Acceleration, PRA = Peak Roof Acceleration, PFV = Peak (Relative) Foundation Velocity, PRDR = Peak Roof Drift Ratio, PIDR = Peak Interstory Drift Ratio, γ= Peak average isolator shear strain, γ_{rate} = Peak average shear strain rate.

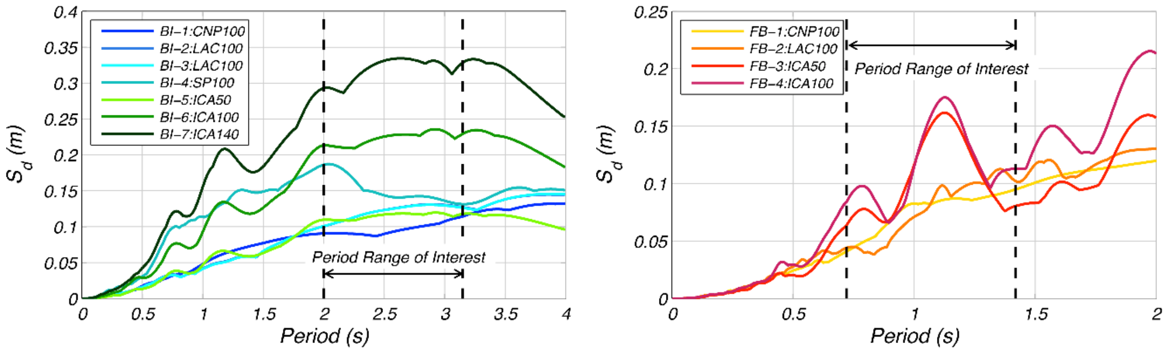

(a) (b)

Figure 3.3: Displacement response spectra for (a) BI configuration (ζ = 12%) and (b) FB configuration (ζ = 5%) for the achieved input ground motions in the case studies.

3.4 Predominant Period Identification Methods

3.4.1 Transfer Function Method

The first mode of response of the test building is identified as largely translational (Astroza et al., 2015), therefore a 2D model is deemed sufficient for analyzing the response of the BNCS building in this study. This assumption is held for all identification methods investigated. The first method for determining T_E of the structure during an earthquake motion is through spectral analysis using a nonparametric method. The predominant frequency components within a signal can be determined by finding the peak of the transfer function, which relates the input (ground floor response) to the output (roof response) signals using power spectral density (PSD) estimations, assuming that the system is linear and time-invariant (Ljung, 1999). The input (x) and output (y) signals were obtained from four triaxial accelerometers mounted at each corner of the ground floor and roof of the building, respectively, during shake table testing. The four longitudinal acceleration responses recorded by each of the four sensors were averaged in time. The floor accelerations measured in the longitudinal direction of the building at each floor during all of the tests discussed in this chapter were very similar, with relative root-mean-square (RMS) errors between the acceleration at the corners and the averaged acceleration less than 5%. For each test motion considered, the average roof and ground floor acceleration responses were first filtered with a fourth-order low-pass Butterworth filter with a cut-off frequency of 25 Hz. The predominant period of the building is found in the frequency domain to be the peak of the transfer function estimate ($\hat{T}_{xy}$), computed as the ratio of the cross PSD estimate between the input and output signals ($\hat{P}_{yx}$) to the PSD estimate of the input signal ($\hat{P}_{xx}$). The PSD functions are estimated using Welch's method (Welch, 1967; Tobita et al., 1988), in which the input and output signal are first segmented into eight overlapping sections of equal length (with a 50% overlap) and windowed using a Hamming window with a length equal to that of the segment.

To check the linearity of the system response, the magnitude-squared coherence function estimate between the input and output signals ($\hat{C}_{xy}$) is calculated as the ratio of the magnitude squared of the cross PSD estimate to the product of the PSD estimate of the input and output signals. A value $\hat{C}_{xy} = 1$ represents a linear system response.

The predominant period (T_E) obtained from $\hat{T}_{xy}$ and the values of $\hat{C}_{xy}$ at T_E are shown in Table 3.4. Estimates of the normalized amplitude of T_{xy} and C_{xy} are plotted against a range of periods for the building in a BI and FB configuration in Figures 3.4 and 3.5, respectively. The predominant periods found from the spectral ratio method are also shown in Table 3.4 and the normalized spectral ratio functions, discussed in the following section, are also plotted in Figure 3.4 and Figure 3.5. For most of the tests, the peak of $\hat{T}_{xy}$ corresponds to a relatively high coherence. However, slight drops in coherence exist around the predominant periods, which can imply slight nonlinearities in the system response (Tobita et al., 1988), which were expected as a result of cracking in the structural concrete members and loosening of the partition walls and façade, as well as measurement noise from both input and output channels.

Table 3.4: Predominant period, T_E, and magnitude-squared coherence, C_{xy}, function estimate at T_E of the building during each test motion using the transfer function method and spectral ratio method.

BI Configuration			
Test Motion	Transfer Function Method		Spectral Ratio Method
	C_{xy} at T_E	T_E (s)	T_E (s)
BI1	0.81	2.44	2.26-2.62
BI2	0.86	2.13	2.64
BI3	0.80-0.94	2.28-2.93	2.62
BI4	0.93	2.84	2.44
BI5	0.83	2.53	2.50
BI6	0.94	3.41	2.72-3.60
BI7	0.93	3.41	2.86-3.60

FB Configuration			
Test Motion	Transfer Function Method		Spectral Ratio Method
	C_{xy} at T_E	T_E (s)	T_E (s)
FB1	0.73	0.90	0.92
FB2	0.87	0.90	0.94
FB3	0.89	1.22	1.24
FB4	0.94	1.42	1.30

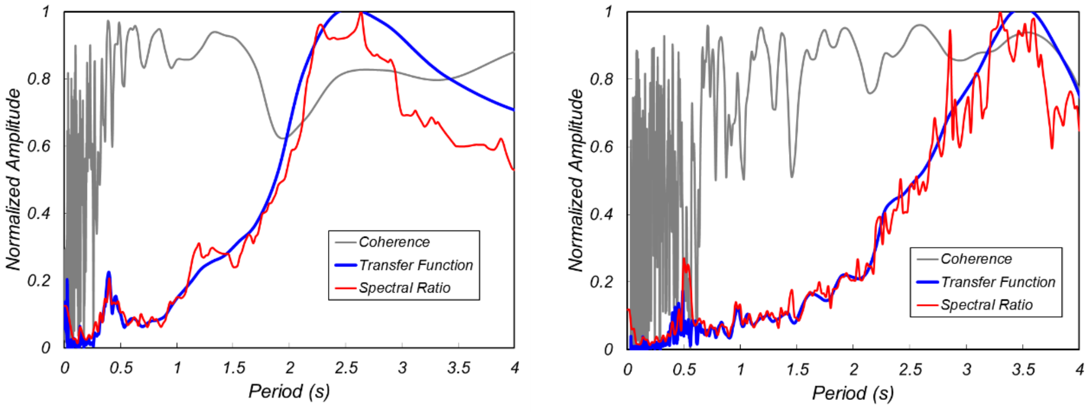

(a) (b)

Figure 3.4: Normalized amplitude of the transfer function estimate, spectral ratio estimate, and magnitude squared coherence function estimate for input and roof response of the base isolated building during (a) BI-1 and (b) BI-7.

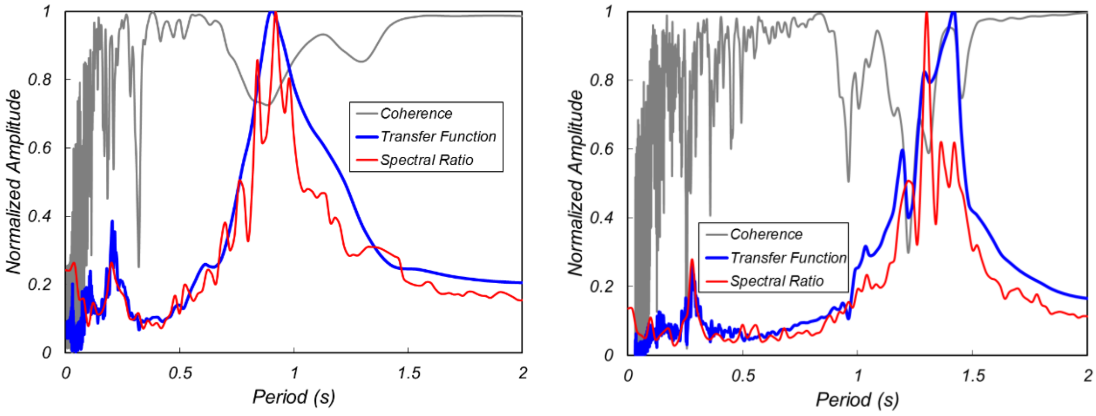

(a) (b)

Figure 3.5: Normalized amplitude of the transfer function estimate, spectral ratio estimate, and magnitude squared coherence function estimate for input and roof response of the fixed base building during (a) FB-1 and (b) FB-4.

3.4.2 Spectral Ratio Method

The second method employed in this chapter to identify the predominant periods of the building during the earthquake input ground motions utilizes the ratio of roof-to-ground undamped pseudo spectral acceleration responses. An advantage of using this method is that spectral responses are familiar to a wide range of structural engineers, and therefore this method can easily be implemented for determining T_E. This method is based on the response spectral ratio method first proposed by Rosenblueth and Arciniega (1992), in which spectral ratios were utilized to estimate the site response of soft soil deposits, taking a record from firm soil as reference, using data from distant earthquakes. This method has also been used to estimate the predominant periods of buildings and to distinguish fundamental structural properties from fundamental input frequencies and site amplifications (Çelebi, 1997).

The accelerations used in this method have also been averaged and filtered using the same process as described in the first method. The ratios of the roof-to-ground undamped response spectral accelerations are calculated for each earthquake motion for a period range of 0.0 - 4.0 s at an interval of 0.02 s. Similar to the transfer function method, the spectral ratios have been normalized by the peak spectral ratio. The peak corresponds to the estimated predominant period of the building system during each input motion.

The normalized amplitudes versus period functions obtained from the transfer function and the spectral ratio methods are plotted together in Figures 3.4 and 3.5 for the BI and FB configurations, respectively. It is apparent that the transfer function method produces a smoother curve than the spectral ratio method, due to the process of overlapping and windowing of the data for the transfer function method. However, the general shapes of the curves produced by the two methods are comparable. The resulting predominant periods in the longitudinal direction are compared in Table 3.4. If there are multiple peaks above 0.95, a range of periods is given rather than a single value. Since the isolator response to the input ground motions is highly nonlinear and because the predominant period of the building-isolation system is very dependent on the input ground motions, there are less distinct peaks for the BI configuration than for the FB configuration.

3.4.3 Time Domain Optimization (TDO) Method

The third method discussed in this chapter uses a time domain optimization method – a variation of the method first used by Beck and Jennings (1980). This method assumes linear response and time-invariant linear viscous damping over the entire excitation duration. In the TDO method, both the predominant period of the building, as well as the equivalent viscous damping ratio associated with the predominant period, are estimated jointly. While the first two methods described previously made use of the recorded total roof accelerations, this method utilizes the roof displacement response. The displacements were obtained at collocated locations by an optimal combination of observed accelerations and GPS displacements using a Kalman filter (Geng et al., 2013). The resulting displacement has millimeter accuracy (Bock et al., 2011). GPS stations were mounted on the roof and foundation levels of the building (as well as a reference location off of the shake table); therefore, Temposonics displacement sensors mounted on the actuators below the shake table platen were also utilized for the BI building. The benefit of using roof displacements is that it can be assumed that the first flexural mode of low to medium-rise regular buildings is almost completely dominated by the first translational mode of response. This method makes the assumption that the first longitudinal mode contributes to 100% of the roof displacements and that the shape of this mode is known and remains the same throughout each phase of testing.

The goal of this method is to optimize the equivalent viscous damping ratio and predominant period of the building during the strongest phase of the response time history. To achieve this, the multi-degree of freedom structure is represented as an equivalent single degree of freedom (SDOF) oscillator. Using the response of the SDOF oscillator with a modal contribution factor ($\Gamma_1\phi_{1,N}$), the roof displacement response is calculated for each input ground motion and compared to the recorded roof displacement response of the test building. The roof displacement is calculated in the following equation (Chopra, 1995):

$$u_{1,N}(t) = \Gamma_1 \phi_{1,N} D_1(t)\,, \qquad \text{where } \Gamma_1 = \frac{\sum_{i=1}^{N} w_i \phi_{1,i}}{\sum_{i=1}^{N} w_i \phi_{1,i}^2} \tag{3.2}$$

and where N is the number of floors, $\phi_{1,i}$ is the first mode shape (found through system identification using WN data and assumed to be time invariant), and w_i is the inertial weight of each floor. The modal participation factor, Γ_1, is relative to the first mode shape, $\phi_{1,i}$, the product of which is referred to as the modal contribution vector at each floor or the modal contribution factor at the roof level ($\Gamma_1\phi_{1,N}$). The modal contribution vector, floor heights, and weights for each floor are found in Table 3.5 for the BI and FB configuration. The spectral displacement, $D_1(t)$ in Equation 3.2, is governed by the equation of motion (Chopra, 1995):

$$\ddot{D}_1(t) + 2\zeta_1(2\pi/\mathrm{T}_1)\dot{D}_1(t) + (2\pi/\mathrm{T}_1)^2 D_1(t) = -\ddot{u}_g(t) \tag{3.3}$$

and
$$T_1 = 2\pi\sqrt{\frac{M_{e1}}{K_1}} \tag{3.4}$$

where ζ_1 is the trial equivalent viscous damping ratio and T_1 is the trial predominant period, which converge to ζ_e and T_E, respectively, when the optimum solution is found, $\ddot{u}_g(t)$ is the input ground acceleration, and where M_{e1} and K_1 are the generalized mass and stiffness for the first mode (Chopra, 1995). Summing the mass at each floor, a total mass (M_t) for the BI and FB configuration is 6306 and 4437 kN/g, respectively. Using the values of $\Gamma_1\phi_{1,i}$ listed in Table 3.5, the modal masses are found to be M_{e1} = 6277 kN/g (99.5% M_t) and 3690 kN/g (83.2% M_t) for the BI and FB test configurations, respectively.

Table 3.5: Height, inertial mass, and first mode contribution vector of each floor for BI and FB configuration.

BI Configuration			
Floor i	Height* (m)	mi (kN/g)	$\Gamma_1\phi_{1,i}$
Platen	0	0	0
Foundation/1	0.74	2075	0.91
2	5.67	727	0.96
3	9.94	757	1.01
4	14.87	989	1.04
5	19.06	1063	1.07
N=6 (Roof)	22.35	695	1.08

FB Configuration			
Floor i	Height* (m)	mi (kN/g)	$\Gamma_1\phi_{1,i}$
1	1.07	206	0
2	4.15	727	0.27
3	8.41	757	0.65
4	13.35	989	0.95
5	17.53	1063	1.13
N=6 (Roof)	20.83	695	1.24

* Note: Height is the distance above ground level to floor center of mass.

While the entire response record can be used with this method, the emphasis is given to the strongest part of the response. Therefore, a threshold can be set on which roof displacement response values are used in the analysis. If the threshold is set too low and includes most of the points in the entire record, the optimization process may not represent the peaks of the response well. Moreover, if the threshold is set too high, then the data used in the optimization is that of few peaks or only a single peak. This chapter only discusses the results obtained for a threshold of 50%. An example of how the threshold is applied to a record is shown in Figure 3.6, where the values of the roof displacement response between ± 50% of the PRDR would be excluded from the optimization process. By doing this, the strong phases of the response are optimized, which is desirable since the system is not truly linear and the sources of energy dissipation can be amplitude-dependent. As a result, accurate responses are not expected in the weak phase of the response.

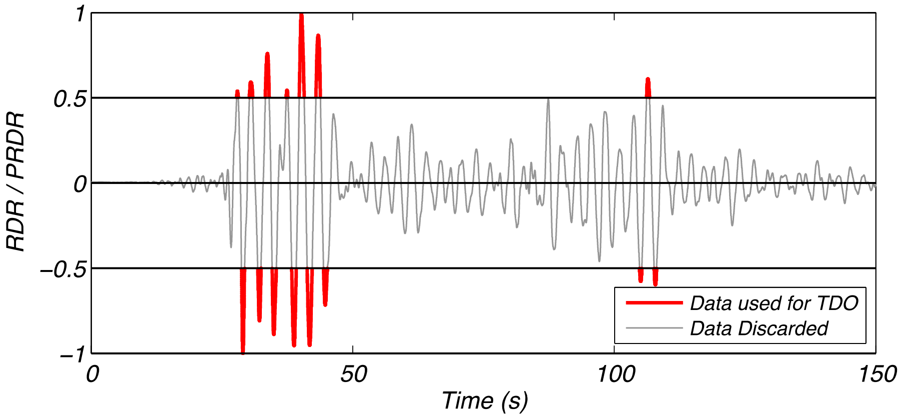

Figure 3.6: Roof drift ratio normalized by PRDR showing data used in TDO (in red) using a 50% threshold.

The roof displacement is calculated with Equation 3.2, where the modal contribution factors are $\Gamma_1\phi_{1,N}$ = 1.08 and 1.24 for the BI and FB configuration, respectively (Table 3.5). Using trial T_1 and ζ_1 values, this displacement is compared to the measured roof displacement for each test. The drift error is found as the difference between the measured response and Eq. 3 for each displacement point considered for this study. Subsequently, the root-mean-square of the drift error (RMS_e) is calculated for each trial T_1 and ζ_1 value. The root-mean-square of the measured roof displacement response (RMS_m) for the displacement points being considered is also found. Using these values, a relative error (RMS_e / RMS_m) is determined for each trial T_1 and ζ_1 value for all BI and FB tests (Figures 3.7 and 3.8, respectively). The error ratio was minimized using grid sizes for the period and damping ratio of 0.05 s and 0.25%, respectively, for the BI configuration, and 0.01 s and 0.25%, respectively, for the FB configuration. The minimum error ratio (marked with a white '+' sign in the figures) corresponds to the optimized T_E and ζ_e. The sensitivity of the solution to T_1 and ζ_1 is observed through the shape of the contour lines. For example, the horizontally elongated shape in Figure 3.7a implies that the solution is more sensitive to ζ_1 than to T_1. Similarly, a vertically elongated shape would imply the opposite. Using the optimized T_E and ζ_e (Table 3.6), the normalized roof displacement from Equation 3.2 is plotted for select motions against the measured roof drift ratio from the BI and FB tests (Figures 3.9 and 3.10, respectively).

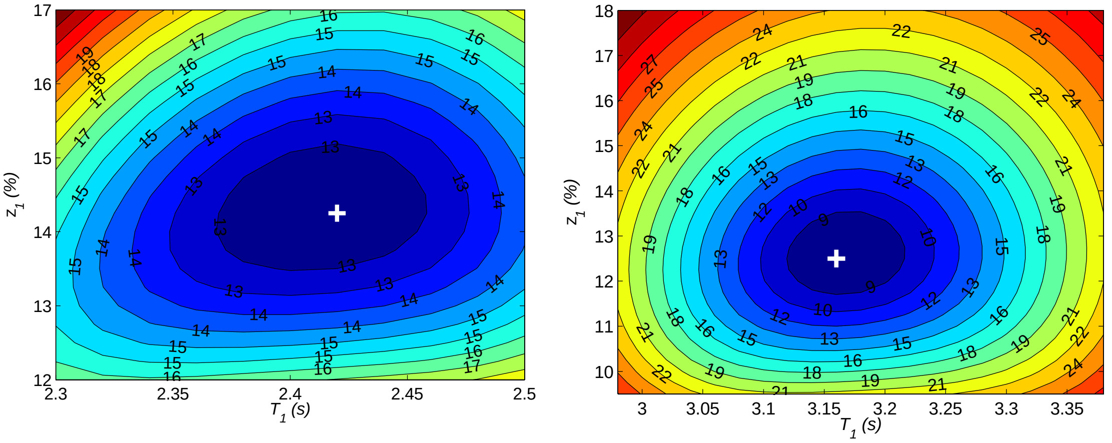

(a) (b)

Figure 3.7: Time domain optimization relative error plots to determine T_E and ζ_e for (a) BI-1:CNP100 and (b) BI-7:ICA140 ($\Gamma_1\phi_{1,N} = 1.08$).

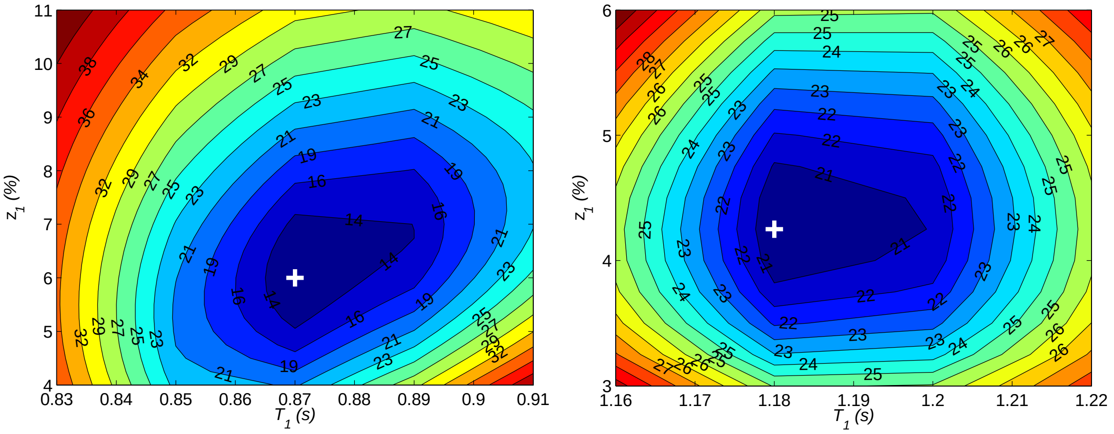

(a) (b)

Figure 3.8: Time domain optimization relative error plots to determine T_E and ζ_e for (a) FB-1:CNP100 and (b) FB-4:ICA100 ($\Gamma_1\phi_{1,N} = 1.24$).

Table 3.6: Optimized values of T_E and ζ_e using the TDO method.

BI Configuration		
Motion	T_E (s)	ζ_e (%)
BI1	2.42	14.3
BI2	2.49	13.3
BI3	2.48	12.8
BI4	2.70	13.5
BI5	2.52	13.5
BI6	2.98	13.5
BI7	3.16	12.5

FB Configuration		
Motion	T_E (s)	ζ_e (%)
FB1	0.87	6.0
FB2	0.96	5.0
FB3	1.09	7.0
FB4	1.18	4.3

*Note ζ_e values for BI configuration using $\Gamma_1\phi_{1,N} = 1.08$ and $\Gamma_1\phi_{1,N} = 1.24$ for FB configuration.

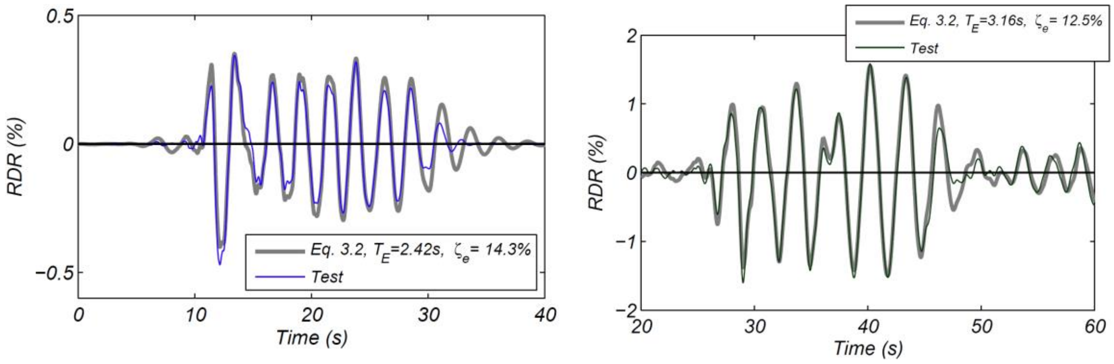

(a) (b)

Figure 3.9: Roof drift ratio time-history comparison between measured response (Test) and response calculated using the TDO method (Eq. 3.2) for (a) BI-1:CNP100 and (b) BI-7:ICA140 ($\Gamma_1\phi_{1,N} = 1.08$).

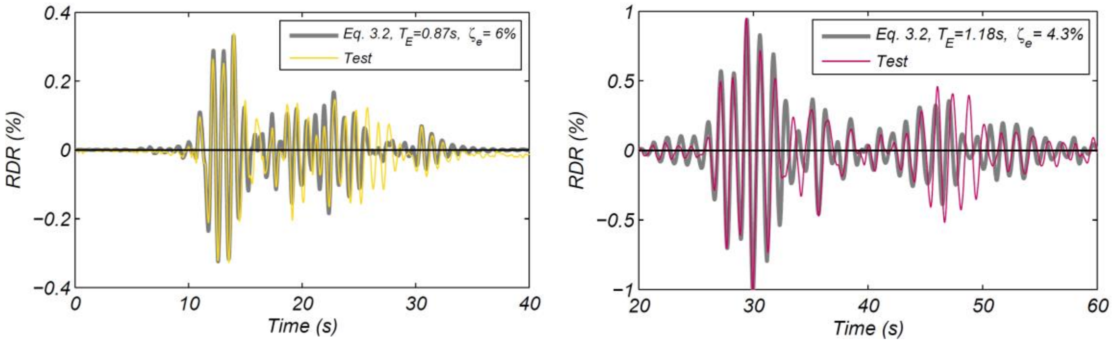

(a) (b)

Figure 3.10: Roof drift ratio time-history comparison between measured response (Test) and response calculated using the TDO method (Eq. 3.2) for (a) FB-1:CNP100 and (b) FB-4:ICA100 ($\Gamma_1\phi_{1,N} = 1.24$).

3.5 Discussion

3.5.1 Comparison of Methods for Determining the Predominant Period

The predominant periods, T_E, of the building identified by the three system identification methods in the BI and FB test configurations, see Tables 3.4 and 3.6, are plotted in Figure 3.11 for all earthquake input ground motions in the sequence the building was tested. The three methods described earlier in this chapter identified predominant periods that vary within a small range. For the BI test configuration, the predominant periods identified are within ± 15 percent of the average of the periods; whereas for the FB test configuration the predominant periods range only within ±10 percent of the average. This means that simple time-domain methods described in this chapter, like the spectral ratio method proposed by Rosenblueth and Arciniega (1992) and the TDO method, have a place in practice for buildings that are regular and whose translational mode shapes are largely uncoupled from torsion.

The predominant periods identified by the methods using strong motion data are, as expected, significantly greater than those periods determined from AV (Astroza et al., 2015), which are also plotted in Figure 3.11. While the predominant period computed from AV remained constant at 0.85 s throughout the BI configuration tests, the predominant periods computed from AV in the FB configuration tests increased progressively from an initial period of 0.52 s before FB1 to 0.56, 0.59, 0.62 and 0.69 s following FB1, FB2, FB3 and FB4, respectively. The increase in predominant period is interpreted herein as due to damage progression, particularly with the loosening and crushing of the gypsum board partitions observed in post-test visual inspections (Pantoli et al., 2013).

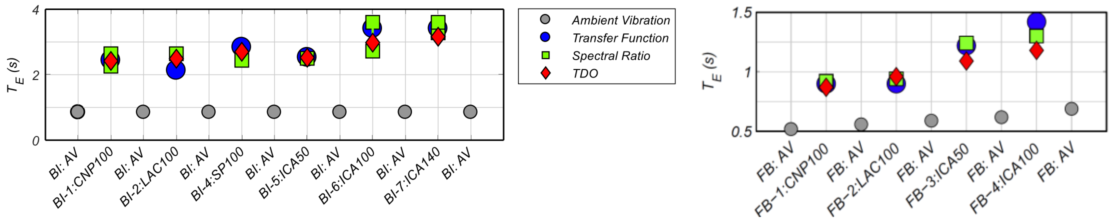

(a) (b)

Figure 3.11: Predominant period, T_E, for (a) BI and (b) FB test motions using three methods. Note different y-axis scales for the BI and FB configuration.

3.5.2 Correlation Between Predominant Period and Peak Ground Velocity

Research has shown that peak ground velocity (PGV) is a good indicator for seismic demand and damage to different types of structures over a broad range of earthquake intensities (Bommer & Alarcon, 2006; Bradley, 2012; Wu et al., 2004). It is therefore of interest to determine the correlation between T_E and PGV for the two case studies. To assess the correlation between T_E and PGV, the predominant periods determined from the TDO method normalized by the initial period T_o, determined from AV before the earthquake tests, are plotted in Figure 3.12 against the PGV for the BI and FB test configurations. Figure 3.12 also plots the predominant periods determined from WN tests and AV measurements recorded before the earthquake tests in each configuration. It is noted that during AV measurements, PGV → 0 m/s. For the two case studies investigated in this chapter, T_E correlates strongly to PGV, and a predictive empirical equation can be used to relate these two parameters in the following equation:

$$T_E = T_0 + (T_f - T_0)\left(1 - \frac{1}{1+\frac{PGV}{1\ m/s}}\right)^p \tag{3.5}$$

where T0 is the initial period determined from AV prior to seismic test motions in the corresponding configuration, Tf is an empirical maximum predominant period, and the p power coefficient is determined empirically. Best fit parameters of Equation 3.5 are shown in Figure 3.12 for both test configurations using data from the TDO method. For the FB motions investigated, the PGV varied within a narrow range of 0.23 to 0.28 m/s, whereas the PGV for the BI motions varied between 0.22 to 0.62 m/s. Additionally, damage to the building in the BI configuration was negligible, whereas a progression of damage was observed during the FB motions, particularly in the partition walls and façade (Pantoli et al., 2013). The R-squared value for the TE values found using the TDO method for the BI and FB configurations are 0.99 and 0.84, respectively. It is noted that the TDO method resulted in a better fit than the other two system identification methods. The mean and standard deviation of the predominant period predicted with Equation 3.5 normalized by the measured predominant period are 0.997 and 0.0346 s for the building in the BI test configuration and are 1.01 and 0.0778 s for the FB test configuration.

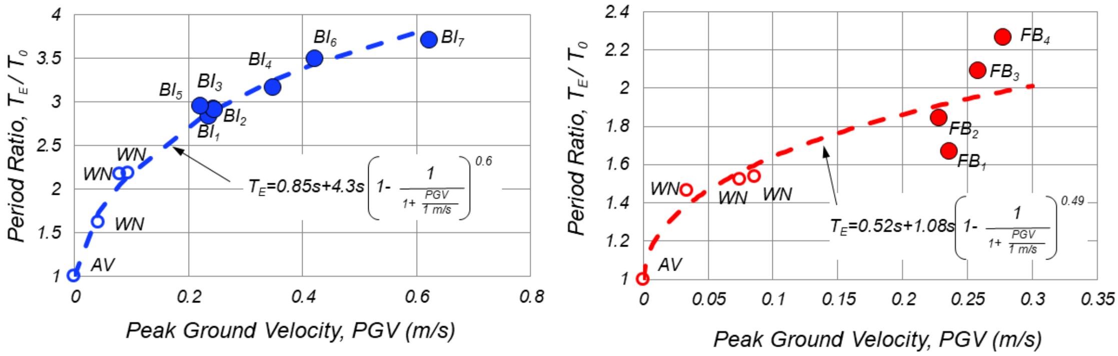

(a) (b)

Figure 3.12: Period ratio (T_E / T_0) vs. Peak Ground Velocity (PGV) for (a) BI configuration and (b) FB configuration.

3.5.3 Predominant Periods and ASCE 7-10

ASCE 7-10 (2010) provides equations to estimate the predominant period of a building in FB and BI configurations. For a base isolated building, predominant periods are defined by ASCE 7-10 for the design and maximum considered earthquakes, respectively as:

$$T_D = 2\pi\sqrt{\frac{W}{k_D g}} \qquad \text{and} \qquad T_M = 2\pi\sqrt{\frac{W}{k_M g}} \tag{3.6}$$

where W is the weight of the building and k is the effective isolation system stiffness determined from prototype testing results at shear strains of 100% and 150% used as the objective for the design and maximum considered earthquakes, respectively. The predominant periods calculated for the BNCS building in the base isolated configuration were 2.9 s for both the design and maximum considered earthquakes. These two periods are identical because the isolator's secant stiffness obtained from prototype testing is practically independent of the shear strain for strains beyond 100%, see Figure 3.2. The shear strains reached in the base isolators in tests BI6 and BI7 were 105 and 155%, respectively. These strains are very close to the target design and maximum considered earthquake strains of 100 and 150%.

Equation 3.6 does not consider the flexibility of the building above the isolation level. Therefore, it is expected that the actual predominant period of the building will exceed the period of 2.9 s found using this equation. This is consistent with the results from the transfer function method (T_E = 3.41 s for BI6 and BI7) as well as the TDO method (T_E = 2.98 s for BI6 and T_E = 3.16 s for BI7). Multiple peaks were determined for the spectral ratio method, resulting in a range of periods from 2.72-3.6 s in test BI6 and 2.86-3.6 s in test BI7 (Table 3.4), in which the shortest period in the ranges are lower than the period given by Equation 3.6.

For buildings in fixed based configurations, ASCE 7-10 (2010) provides two options to determine the predominant period. The first option is equation 12.8-7 in ASCE 7-10 reproduced here for convenience:

$$T_a = C_t h_n^x \tag{3.7}$$

where h_n is the height of the structure taken as 20.83 m, and C_t and x are tabulated parameters corresponding to a RC moment-resisting frame, which are 0.0466 and 0.9, respectively. This equation results in a predominant period of 0.72 s. The second option is given by ASCE 7-10 §12.8.2. The predominant period in this method is defined as the lesser of C_uT_a and the predominant period of the building found from structural analysis, where C_u is the upper limit coefficient found from Table 12.8-1. For this building, C_u = 1.4, resulting in an upper bound period of 1.0 s. This upper bound period is within the range of predominant periods identified for the building in tests FB1 through FB4 that ranged between 0.87 – 1.42 s for all three system identification methods discussed above.

The predominant period found using Equation 3.7 as well as the upper bound period is plotted for a range of building heights in Figure 3.13. Data collected from RC moment frame buildings during ground motions with PGA ≥ 0.15 g and reported by Goel and Chopra (1997) are also plotted in this figure. Similar to the other buildings, the predominant periods identified for the BNCS building are within acceptable range of the upper bound period.

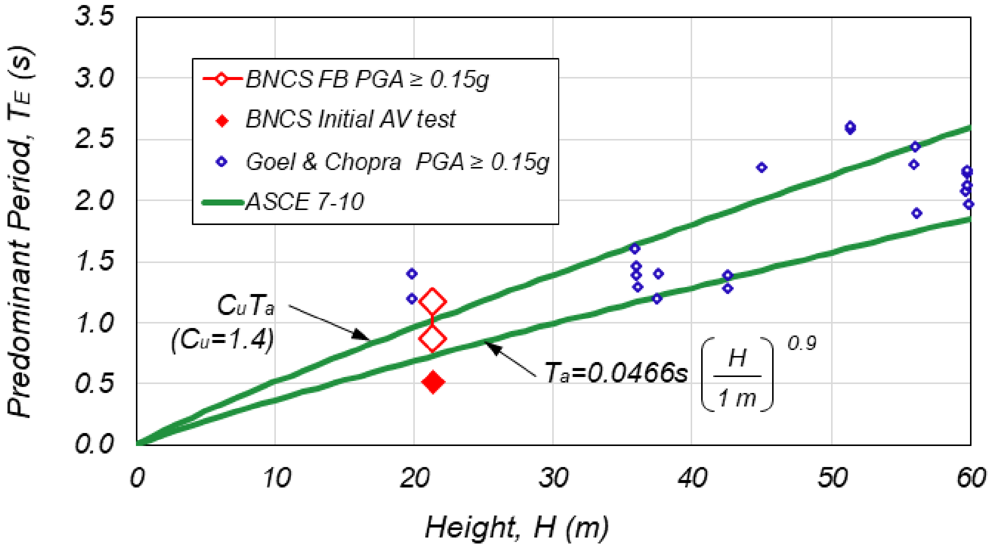

Figure 3.13: Predominant period of buildings when PGA ≥ 0.15 g and code formulas for RC moment frame buildings.

3.5.4 Effective Stiffness in the Fixed Base Configuration

The predominant period of a building, T_E, is inversely proportional to the square root of the effective system stiffness, K_e. Assuming that the first mode shape and the first mode modal mass remain unchanged throughout the tests investigated, the lengthening of the predominant period represents a degradation of the building system's stiffness. Mathematically, the degraded or effective system stiffness can be expressed as:

$$K_e = (T_0/T_E)^2 K_0 \qquad (3.8)$$

where the period determined through system identification from AV data recorded prior to FB testing is considered the initial period, T_0 = 0.52 s (Figure 3.11), which corresponds to the initial building stiffness, K_0. The reduced stiffness can be attributed to both recoverable and non-recoverable (or degraded) stiffness. Degraded stiffness refers to the stiffness that has been permanently reduced and is detectable through the lengthened period found from AV data. The recoverable stiffness refers to the loss of stiffness due to cracks that open and close, or nonstructural components that slide after overcoming an initial friction force. It is assumed that any loss of recoverable stiffness is not detectable during AV; therefore, the total reduced stiffness can be disaggregated into recoverable and degraded stiffness. The distinction of recoverable stiffness has been previously identified and discussed (Ebrahimian et al., 2016), where it was thought to have been the main contributor to larger changes in frequency using strong motion data than using AV following the earthquake motion.

Table 3.7 lists values of the total reduced stiffness computed from Equation 3.8, normalized by the initial stiffness, K_e / K_0, for motions FB1-FB4 using the three system identification methods described in this chapter. The average from the three methods is also listed in this table. Using the three methods, the stiffness is reduced to an average of 33% and 16% of the initial stiffness at the peak displacements during FB1 and FB4, respectively, and is reduced to 85% and 56% of the initial stiffness at the end of these tests (using periods from AV), implying that 52% and 40% of the initial stiffness was recovered – chiefly by closure of cracks in structural elements. As noted before, test FB4 was below the design earthquake intensity. Due to the complexity of the system, it is not possible to disaggregate the loss of stiffness of the system into the loss of stiffness of the nonstructural systems or their connection to the structure and the loss of stiffness of the structure.

Table 3.7: Building effective system stiffness for FB motions.

Motion	Identification Method				AV following motion
	Transfer Function	Spectral Ratio	TDO	Average	
	K_e / K_0	K_e / K_0	K_e / K_0	K_e / K_0	K_e / K_0
FB1	0.33	0.32	0.35	0.33	0.85
FB2	0.33	0.30	0.29	0.31	0.77
FB3	0.18	0.17	0.23	0.19	0.70
FB4	0.13	0.16	0.19	0.16	0.56

3.5.5 Equivalent Viscous Damping Ratio Associated with the Predominant Period

Prior to seismic testing, each isolator underwent quasi-static testing at shear strain histories prescribed by NCh2745-2003. Figure 3.14 plots the equivalent viscous damping ratio versus the peak shear strain using quasi-static reversed cyclic load prototype test data, with the error bars indicating the range of results for the four bearings. The recommended ASCE 7-10 values for damping are presented by connecting the average ζ_e values linearly. These equivalent viscous damping ratios, ζ_e, were calculated using Jacobsen's method (1930, 1960), as is done in NCh2734-2003 as well as ASCE 7-10. These quasi-static tests indicate that ζ_e decreases when the peak shear strain increases.

The equivalent viscous damping ratios of the system were also computed for the BNCS building in the BI configuration using the TDO method. The values of ζ_e shown were computed for $\Gamma_1\phi_{1,N} = 1.08$ as reported in Table 3.6. These ζ_e values of the system include energy dissipated from the isolation system as well as other sources of energy dissipation from the building above the isolation system. The small interstory drift ratios observed during BI tests suggest that most of the energy dissipation occurred at the isolation level. Figure 3.14 compares the values of ζ_e, found from the TDO method for $\Gamma_1\phi_{1,N} = 1.08$ with the values of ζ_e found from prototype testing. For the TDO method, a threshold of 50% is shown as well as a range of 40-60%, with the lower damping value corresponding to a 60% threshold. This range illustrates the sensitivity of the results based on the ground motion, with minimal sensitivity in the BI tests with peak shear strain exceeding 100% compared to the sensitivity of the BI test with a peak shear strain close to 60%. In contrast with the values of ζ_e determined from quasi-static tests using Jacobsen's method as recommended in ASCE 7-10, the values of ζ_e determined from the seismic tests using the TDO method are largely independent of peak shear strain. While there are discrepancies between the ζ_e approximations for the lower peak shear strains from the difference in the derivations of ζ_e, both methods, give very similar values of ζ_e at peak shear strains exceeding 100%. The close comparison of the values of ζ_e at peak shear strains in excess of 100% leads to the conclusion that ζ_e for the high damping isolators used in this test program is represented well by the values of ζ_e found from prototype testing using recommendations by ASCE 7-10.

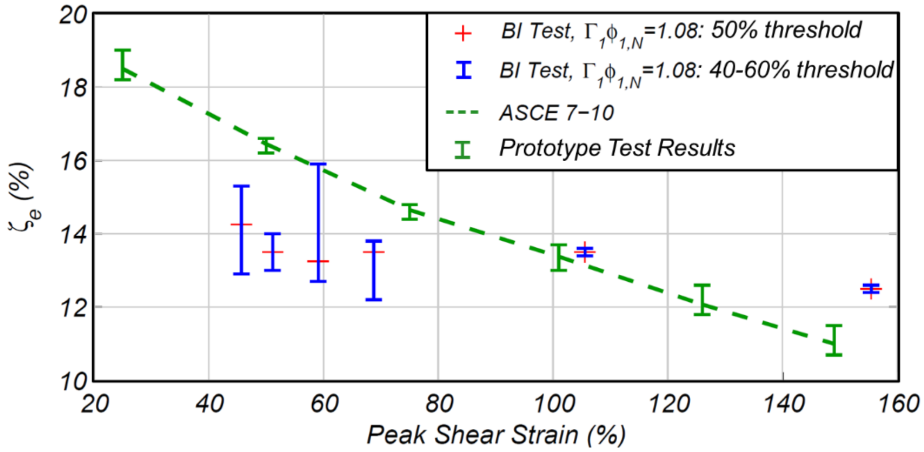

Figure 3.14: Equivalent viscous damping ratio vs. peak isolator shear strain.

For the building in the FB configuration, the equivalent viscous damping ratios found from the TDO method range from 4.3-7.0% and are listed in Table 3.6. Similar to the BI configuration, these ζ_e values correspond to the T_E values computed for each earthquake motion. It should be noted that the ζ_e computed for the initial period during AV recorded before FB testing, T_0, is 1.0% (Astroza et al., 2015), which is considerably lower than those computed during the earthquake motions. The equivalent viscous damping ratios observed for the BNCS building in the FB configuration in the tests prior to the development of yielding in the structural elements are all within the bounds recommended in elastic analysis.

3.6 Conclusions

Three simple system identification methods for determining the predominant period, T_{E}, one of which also determines the corresponding equivalent viscous damping ratio, ζ_e, of a building during strong seismic excitations were presented in this chapter. Two case studies were investigated to demonstrate the applicability of these methods. The building used for these case studies is a full-scale five story reinforced concrete building which was tested on a shake table in a base isolated configuration and in a fixed base configuration. The building was fully outfitted with nonstructural systems, including partition walls and a façade, which added to the initial stiffness of the building. The building was subjected to a series of earthquake ground motions in both base configurations. For this chapter, the motions investigated for the fixed base building were below the design earthquake intensity and the structure had not developed any plasticity.

All three methods presented in this chapter resulted in similar predominant periods for each earthquake motion. The predominant period of the building was found to be dependent on the earthquake intensity, with a strong correlation to the PGV. A reasonable estimate for the predominant period was found using equations provided by ASCE 7-10 for both the base isolated and fixed base building. Using the T_E values found during each motion, the degraded system stiffness was found for the building in a fixed base configuration after each motion. A significant reduction of system stiffness was observed during the series of earthquakes investigated, with an effective system stiffness of about 16% of the initial stiffness at the peak displacements, and 56% of the initial stiffness after the earthquake motion, implying that 40% of the initial stiffness was recovered.

One of the system identification methods presented in the chapter estimated the equivalent viscous damping ratio corresponding to the predominant period of the building during each motion. The results were also compared to the values computed using a code-based approach. For the building in a base isolated configuration, the equivalent viscous damping ratio was compared to the results from quasi-static reversed cyclic prototype test data, as recommended by ASCE 7-10. While there were inconsistencies in the equivalent viscous damping ratios below 100% shear strain, the results above 100% shear strain, which are the values of interest for design purposes, were consistent between the code-based and experimental results.

3.7 Acknowledgements

The BNCS project was a collaboration between four academic institutions (University of California, San Diego, San Diego State University, Howard University, and Worcester Polytechnic Institute) and was funded by NSF-NEESR program, grant number CMMI-0936505, the National Science Foundation, the Englekirk Advisory Board, the Charles Pankow Foundation, and the California Seismic Safety Commission, over 40 industry partners and two oversight committees. A listing of project participants may be found on the project website: http://bncs.ucsd.edu/index.html. The accelerometer/GPS Kalman filter analysis was performed by Jessie Saunders and funded by NASA grant NNX14AT33G. Opinions and findings expressed in this chapter are those of the authors and do not necessarily reflect the views of the funding agencies.

The work in this chapter is published in Chen, M., Astroza, R., Restrepo, J. I., Conte, J. P., Hutchinson, T., and Bock, Y. (2017). Predominant period and equivalent

viscous damping ratio identification for a full-scale building shake table test, Earthquake *Engineering and Structural Dynamics, 46*(14), 2459-2477.

3.8 Appendix B: Supplemental Information

3.8.1 Transfer Function Method and Spectral Ratio Method

Supplemental figures to sections 3.4.1 and 3.4.2 are shown in Figure 3.16 for the remaining fixed base configuration earthquake ground motions. Likewise, Figure 3.15 shows supplemental figures to sections 3.4.1 and 3.4.2 for the remaining base isolated configuration earthquake ground motions.

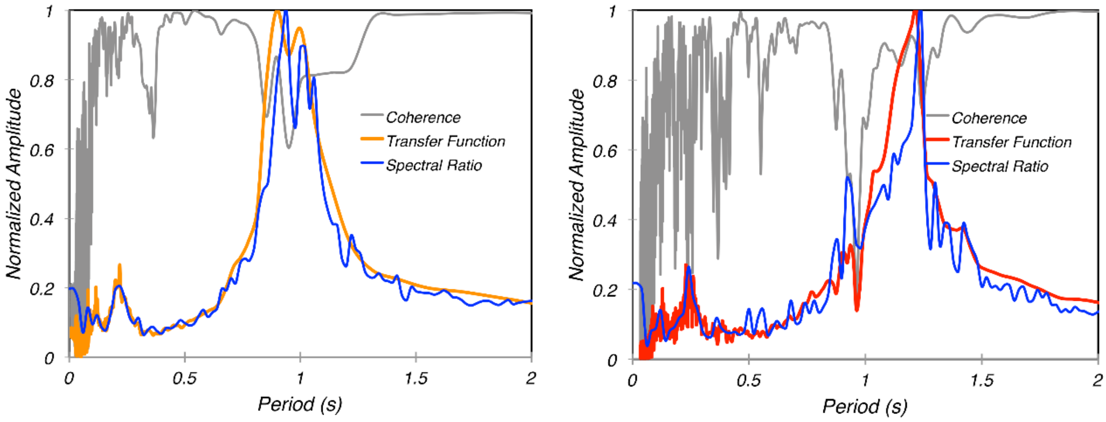

(a) (b)

Figure 3.15: Normalized amplitude of the transfer function estimate, spectral ratio estimate, and magnitude squared coherence function estimate for input and roof response of the base isolated building during (a) FB-2 and (b) FB-3.

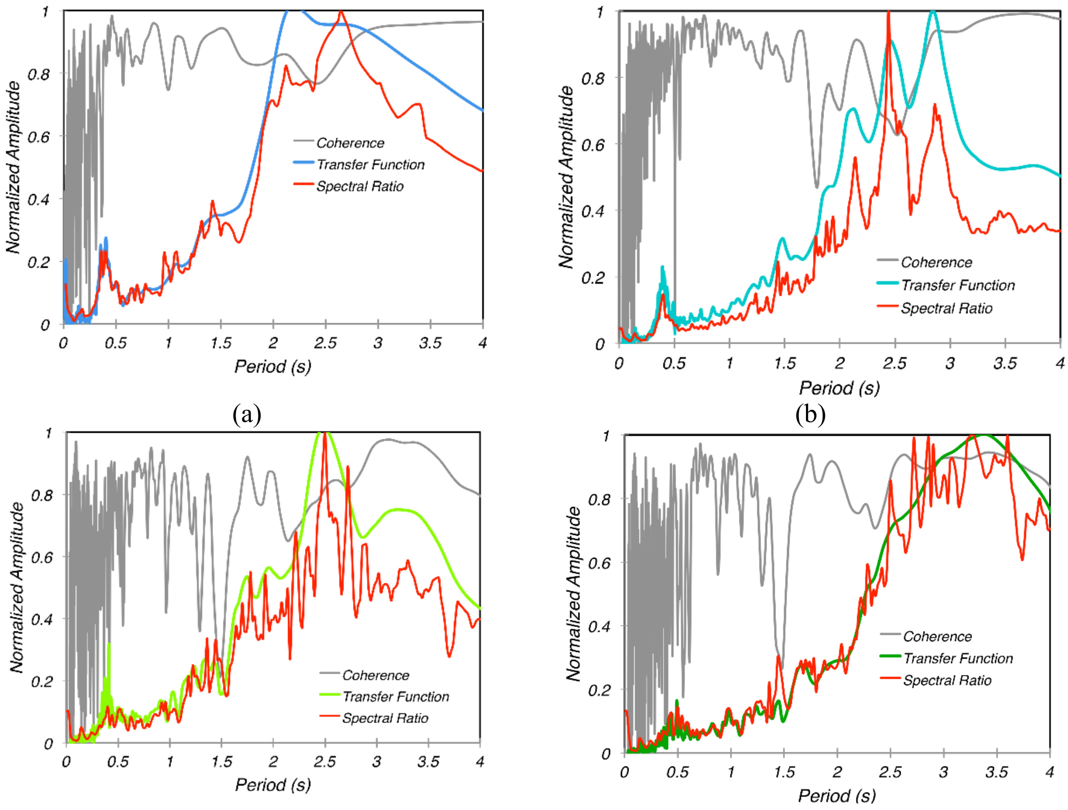

(a) (b)

(c) (d)

Figure 3.16: Normalized amplitude of the transfer function estimate, spectral ratio estimate, and magnitude squared coherence function estimate for input and roof response of the base isolated building during (a) BI-2, (b) BI-4, (c) BI-5, and (d) BI-6.

3.8.2 Time Domain Optimization Method

Supplemental figures to section 3.4.3 are shown in Figure 3.17 and Figure 3.18 of the remaining base isolated configuration earthquake ground motions. Similarly, Figure 3.19 and Figure 3.20 show supplemental figures to sections 3.4.3 for the remaining fixed base configuration earthquake ground motions.

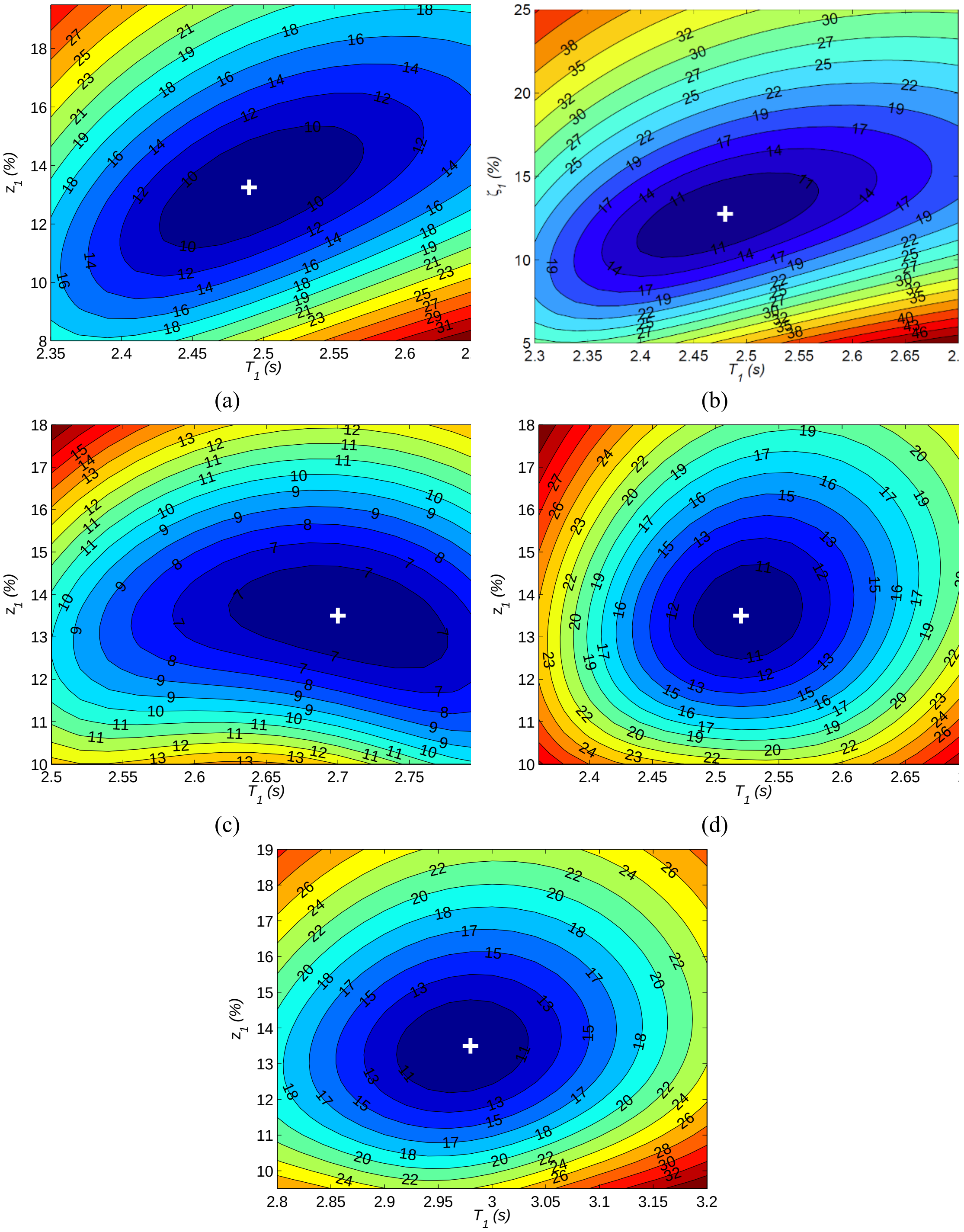

(a) (b) (c) (d) (e)

Figure 3.17: Time domain optimization relative error plots to determine T_E and ζ_e for (a) BI-2, (b) BI-3, (c) BI-4, (d) BI-5, and (e) BI-6 ($\Gamma_1\phi_{1,N}$ = 1.08).

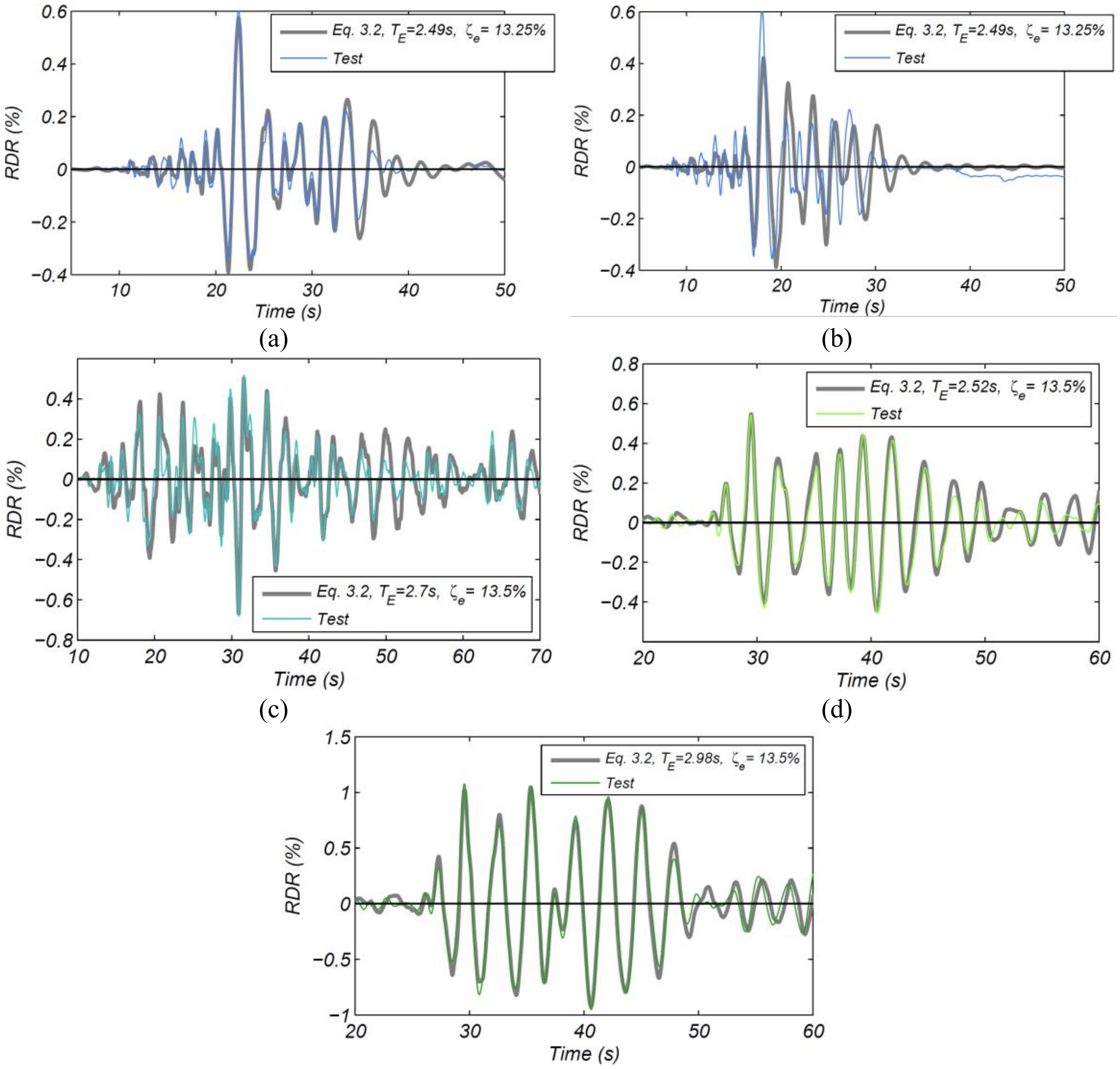

(a) (b)

(c) (d)

(e)

Figure 3.18: Roof drift ratio time-history comparison between measured response (Test) and response calculated using the TDO method (Eq. 3.2) for (a) BI-2, (b) BI-3, (c) BI-4, (d) BI-5, and (e) BI-6 ($\Gamma_1\phi_{1,N}$ = 1.08).

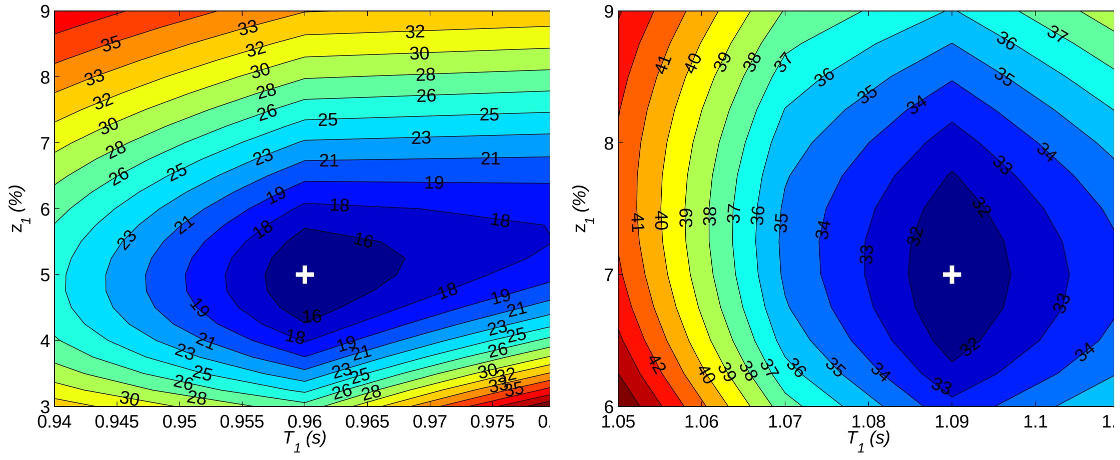

(a) (b)

Figure 3.19: Time domain optimization relative error plots to determine T_E and ζ_e for (a) FB-2 and (b) FB-3 ($\Gamma_1\phi_{1,N}$ = 1.24).

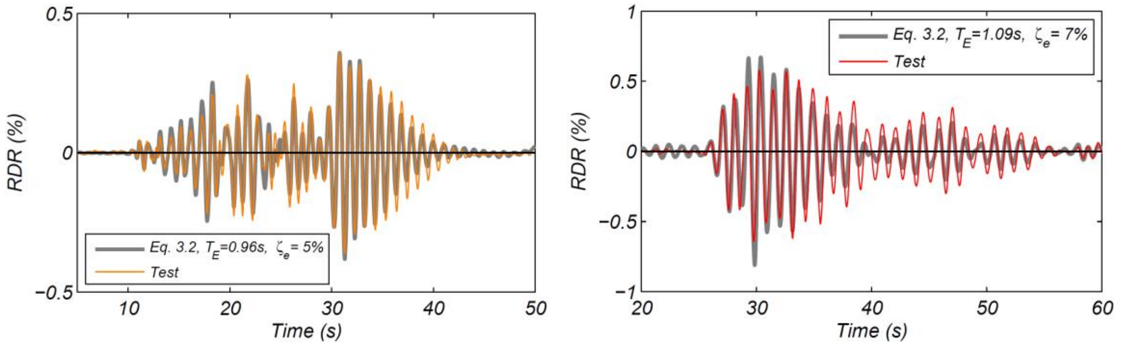

(a) (b)

Figure 3.20: Roof drift ratio time-history comparison between measured response (Test) and response calculated using the TDO method (Eq. 3.2) for (a) FB-2 and (b) FB-3 ($\Gamma_1\phi_{1,N}$ = 1.24).

3.8.2.1 White Noise Base Excitation

The time domain optimization method was also utilized to find the predominant period and the corresponding equivalent viscous damping ratio of the building during three white noise base excitations of increasing intensity performed prior to FB-1. The results are tabulated in Table 3.8 for a threshold of 30% (where the values of the roof displacement response between ± 30% of the PRDR would be excluded from the optimization process) and in Table 3.9 for a threshold of 50%. These results compare well with the results using system identification methods (Astroza et al., 2015) which found T_E = 0.71s, 0.77s and 0.79s for WN1, WN2 and WN3, respectively; and ζ_e = 6.8%, 5.9% and 4.7% for WN1, WN2 and WN3, respectively. TDO relative error plots and plots comparing the measured and calculated roof drift ratio time history response (using the results for the threshold with the minimum error ratio) are presented for the three white noise motions in Figure 3.21 and Figure 3.22, respectively.

Table 3.8: Optimized values of T_E and ζ_e for white noise motions using the TDO method with a 30% threshold.

FB Motion	T_E (s)	ζ_e (%)	Error ratio (%)
WN1	0.74	7.0	12
WN2	0.79	5.5	11
WN3	0.80	4.5	63

Table 3.9: Optimized values of T_E and ζ_e for white noise motions using the TDO method with a 50% threshold.

FB Motion	T_E (s)	ζ_e (%)	Error ratio (%)
WN1	0.76	7.2	7.9
WN2	0.79	2.5	41
WN3	0.80	3.5	73

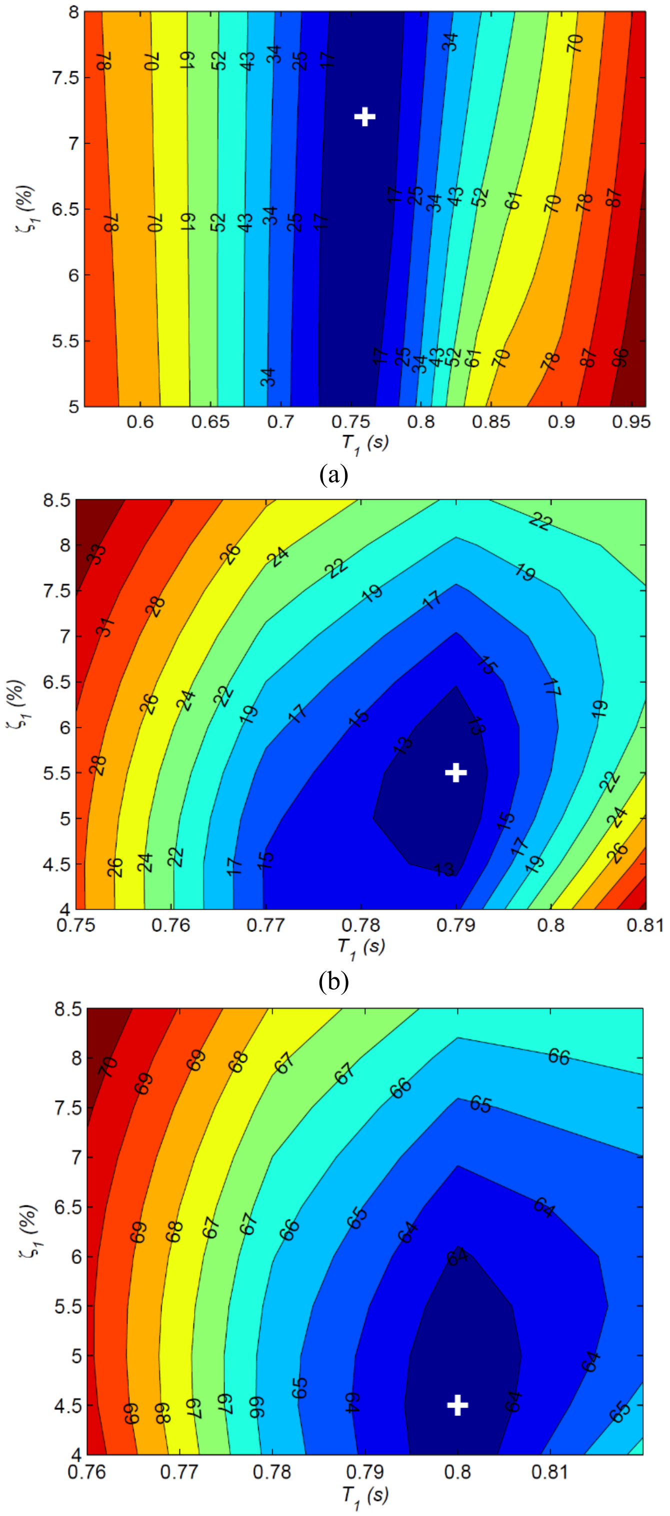

(a)

(b)

(c)

Figure 3.21: Time domain optimization relative error plots to determine T_E and ζ_e for (a) WN1 (50% threshold), (b) WN2 (30% threshold), and (c) WN3 (30% threshold).

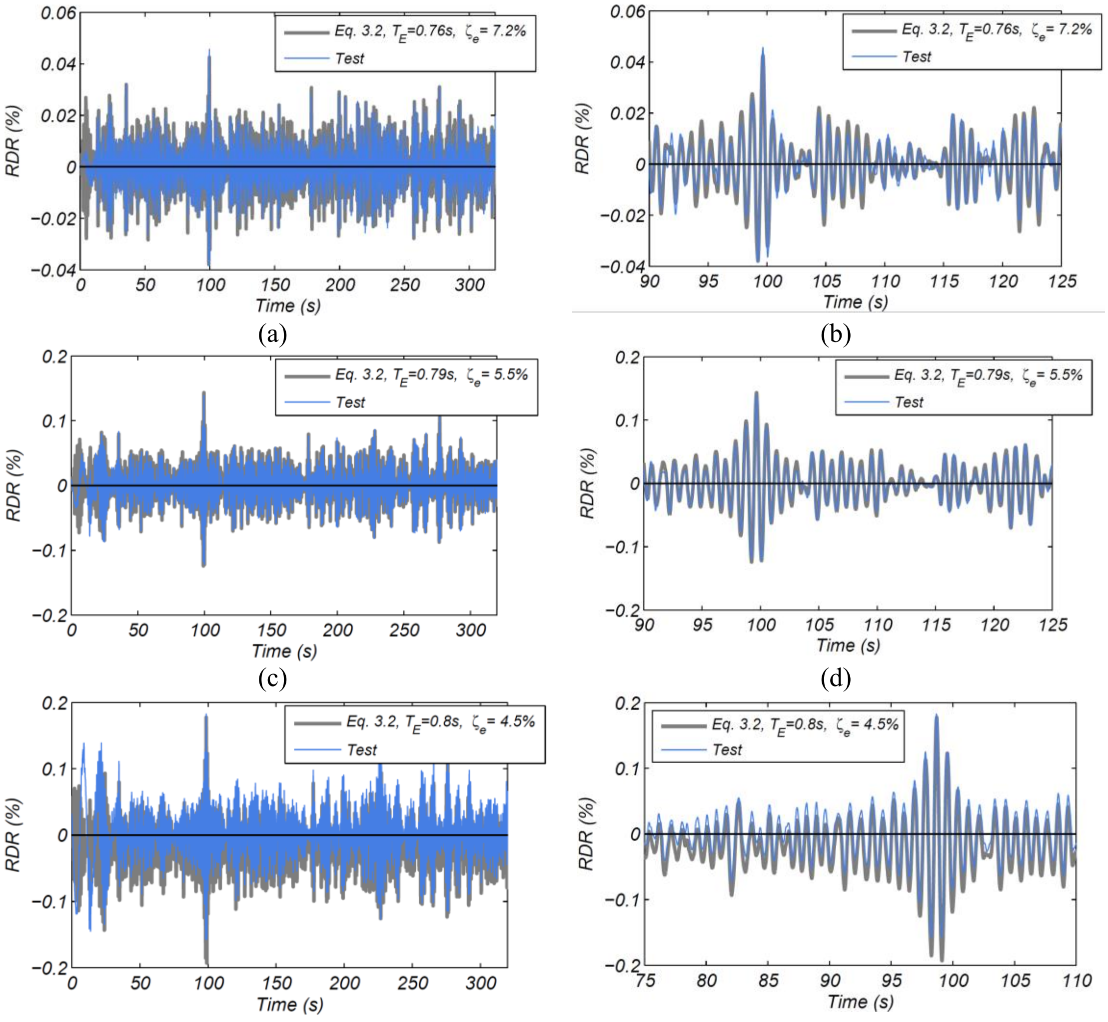

(a) (b)

(c) (d)

(e) (f)

Figure 3.22: Roof drift ratio time-history comparison between measured response (Test) and response calculated using the TDO method (Eq. 3.2) for (a) WN1, (b) WN1 (zoomed), (c) WN2, (d) WN2 (zoomed), (e)WN3 and (f) WN3 (zoomed).

3.8.3 Equivalent Viscous Damping Ratio

The equivalent viscous damping ratio found from quasi-static testing appears to be accurate for the larger intensity ground motions, but is over predicted for the lower intensity ground motions. Because of this disparity, the ratio of the energy dissipated by the building above the isolation system to the total energy dissipated was investigated. This ratio was calculated by finding the ratio of the areas within the hysteretic loops in Figure 3.23a and Figure 3.23b (although presented differently in the plots, the ratios were normalized using the same parameters and equivalent x-axes). The resulting ratios are plotted against the peak shear strains for the earthquake ground motion tests in Figure 3.24b. Since the building's participation in energy dissipation relative to the building-isolation system is minimal and relatively constant for all ground motion intensities, ranging from about 3 – 6%, it is noted that the additional energy dissipated by the building above the isolation system does increase with higher intensity motions, but is proportional to the shear strain of the isolator.

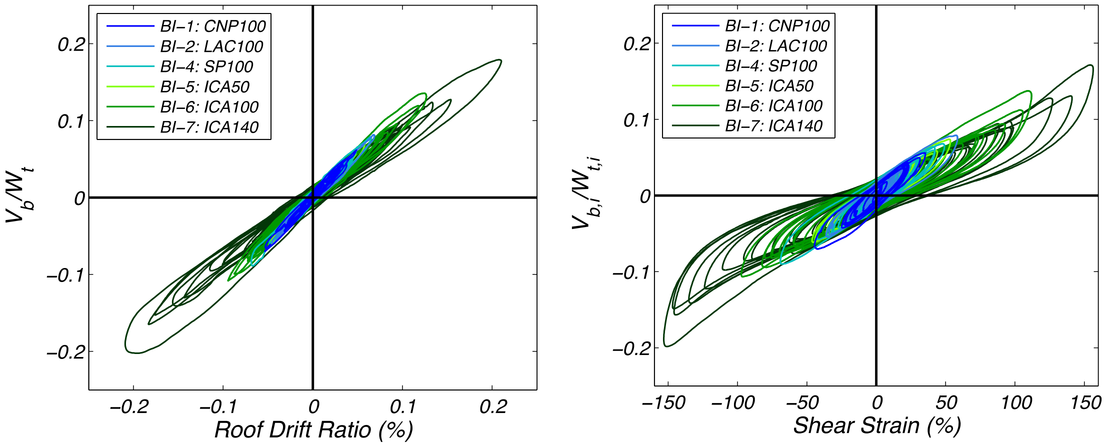

(a) (b)

* Note: W_t = weight of building above foundation, $W_{t,i}$ = weight of building including foundation

Figure 3.23: Hysteretic response of (a) total base shear above isolation system (V_b) vs. roof drift ratio and (b) total base shear below isolation system ($V_{b,i}$) vs. shear strain for all BI tests.

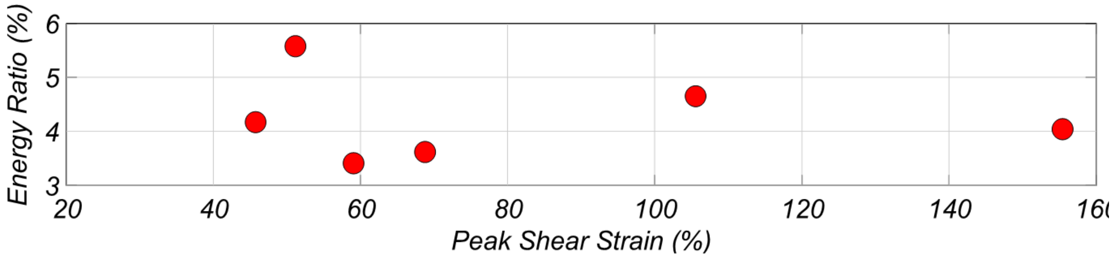

Figure 3.24: Ratio of hysteretic energy dissipated by the building above isolation system to total energy dissipated (energy index ratio) vs. peak isolator shear strain.

3.9 References

Alford, J. L., & Housner, G. W. (1953). A dynamic test of a four-story reinforced concrete building. *Bulletin of the Seismological Society of America*, *43*(1), 7-16.

ASCE/SEI. (2010). Minimum design loads for buildings and other structures. *SEI/ASCE 7-10,* American Society of Civil Engineers, Reston, VA.

Astroza, R., Ebrahimian, H., Conte, J. P., Restrepo, J. I., & Hutchinson, T. C. (2015). System identification of a full-scale five-story reinforced concrete building tested on the NEES-UCSD shake table. *Structural Control and Health Monitoring*, *23*(3), 535–559.

Astroza, R., Ebrahimian, H., Conte, J. P., Restrepo, J. I., Hutchinson, T. C. (2016). Influence of the construction process and nonstructural components on the modal properties of a five-story building. *Earthquake Engineering & Structural Dynamics*, *45*(7), 1063–1084.

Baird, A., Tasligedik, A. S., Palermo, S., & Pampanin, S. (2014). Seismic performance of vertical non-structural components in the 22nd February 2011 Christchurch earthquake. *Earthquake Spectra, 30*(1), 401-425.

Beck, J. L., & Jennings, P. C. (1980). Structural identification using linear models and earthquake records. *Earthquake engineering & structural dynamics*, *8*(2), 145-160.

Belleri, A., Moaveni, B., & Restrepo, J. I. (2013). Damage assessment through structural identification of a three-story large-scale precast concrete structure. *Earthquake Engineering & Structural Dynamics*, *43*(1), 61–76.

Blume J. (1935). A machine for setting structures and ground into forced vibration. *Bulletin of the Seismological Society of America*, *25*(4), 361-379.

Bock, Y., Melgar, D., & Crowell, B. W. (2011). Real-time strong-motion broadband displacements from collocated GPS and accelerometers. *Bulletin of the Seismological Society of America*, *101*(6), 2904-2925.

Bommer, J. J., & Alarcon, J. E. (2006). The prediction and use of peak ground velocity. *Journal of Earthquake Engineering*, *10*(01), 1-31.

Bradley, B. A. (2012). Empirical correlations between peak ground velocity and spectrum-based intensity measures. *Earthquake Spectra*, *28*(1), 17-35.

Çelebi, M., Phan, L. T., & Marshall, R. D. (1993). Dynamic characteristics of five tall buildings during strong and low-amplitude motions. *The Structural Design of Tall Buildings*, *2*(1), 1-15.

Çelebi, M. (1997). Response of Olive View Hospital to Northridge and Whittier earthquakes. *Journal of Structural Engineering*, *123*(4), 389-396.

Chen, M. C., Pantoli, E., Astroza, R., Ebrahimian, H., Mintz, S., Wang, X., Hutchinson, T., Conte, J., Restrepo, J., Meacham, B., Kim, J., Park, H. (2013). BNCS report #1: full-scale structural and nonstructural building system performance during earthquakes and post-earthquake fire - specimen design, construction and test protocol. *Structural Systems Research Project Report Series, SSRP 13/9*. University of California San Diego, La Jolla, CA.

Chen, M. C., Pantoli, E., Wang, X., Astroza, R., Ebrahimian, H., Hutchinson, T. C., Conte, J. P., Restrepo, J. I., Marin, C., Walsh, K., Bachman, R. E., Hoehler, M. S., Englekirk, R., & Faghihi, M. (2016). Full-scale structural and nonstructural building system performance during earthquakes: part I – specimen description, test protocol and structural response. *Earthquake Spectra, 32*(2), 737-770.

Chopra, A. K. (1995) Dynamics of structures. Vol 3. New Jersey: Prentice Hall.

Cole, E. E., Tokas, C.V., & Meehan, J. F. (1992). Analysis of recorded building data to verify or improve 1991 uniform building code (UBC) period of vibration formulas. *Proceedings of SMIP92, Strong Motion Instrumentation Program, Division of Mines and Geology, California Department of Conservation*.

Ebrahimian, M., Todorovska, M. I., & Falborski, T. (2016). Wave method for structural health monitoring: testing using full-scale shake table experiment data. *Journal of Structural Engineering, 143*(4), 04016217.

Geng, J., Melgar, D., Bock, Y., Pantoli, E., & Restrepo, J. (2013). Recovering coseismic point ground tilts from collocated high-rate GPS and accelerometers. *Geophysical Research Letters*, *40*(19), 5095-5100.

Goel, R. K., & Chopra, A. K. (1997). Vibration properties of buildings determined from recorded earthquake motions, *UCB/EERC-97/14*.

INN, Instituto Nacional de Normalizacion, NCh2745, Seismic Analysis and Design of Building with Seismic Isolation (applicable 2006), Santiago, Chile (in Spanish).

Ivanovic, S. S., Trifunac, M. D., & Todorovska, M. I. (2000). Ambient vibration tests of structures – a review, *Journal of Earthquake Technology, ISET, 37*(4), 165-197.

Jacobsen, L. S. (1930). Steady forced vibrations as influenced by damping. *Transactions*, *52*(15), 169-181.

Jacobsen, L. S. (1960). Damping in composite structures. *Proceedings, 2nd WCEE.*

Ji, X., Fenves, G., Kajiwara, K., & Nakashima, M. (2011). Seismic damage detection of a full-scale shaking table test structure. *Journal of Structural Engineering*, *137*(1), 14–21.

LATBSDC: Los Angeles Tall Buildings Structural Design Council. (2014). An alternative procedure for seismic analysis and design of tall buildings located in the Los Angeles region. Los Angeles, CA.

Li, B., & Mosalam, K. M. (2013). Seismic performance of reinforced-concrete stairways during the 2008 Wenchuan earthquake. *Journal of Performance of Constructed Facilities, 27*(6), 721–730.

Ljung, L. (1999). System identification: theory for the user, 2nd ed., Prentice Hall, Upper Saddle River, NJ.

Marshall, R. D., Phan, L. T., & Çelebi, M. (1994). Full-scale measurement of building response to ambient vibration and the Loma Prieta earthquake. *Proceedings, Fifth U.S. National Conference of Earthquake Engineering*, 661-670.

Miranda, E., Mosqueda, G., Retamales, R., & Pekcan, G. (2012). Performance of nonstructural components during the 27 February 2010 Chile earthquake. *Earthquake Spectra*, *28*(S1), S453–S471.

Moaveni, B., He, X., Conte, J. P., Restrepo, J. I., & Panagiotou, M. (2011). System identification study of a seven-story full-scale building slice tested on the UCSD-NEES shake table. *Journal of Structural Engineering, 137*(6), 705–717.

Nagarajaiah, S., & Xiaohong, S. (2000). Response of base-isolated USC hospital building in Northridge earthquake, *Journal of Structural Engineering, 126*(10), 1177–1186.

Pacific Earthquake Engineering Research (PEER) Center. (2010). TBI - Guidelines for performance-based seismic design of tall buildings. Berkeley, CA.

Pantoli, E., Chen, M. C., Wang, X., Astroza, R., Ebrahimian, H., Mintz, S., Hutchinson, T., Conte, J., Restrepo, J. I., Meacham, B., Kim, J., & Park, H. (2013). BNCS report #2: full-scale structural and nonstructural building system performance during earthquakes and post-earthquake fire - test results. *Structural Systems Research Project Report Series, SSRP 13/10*. University of California San Diego, La Jolla, CA.

Pantoli, E., Chen, M. C., Hutchinson, T., & Restrepo, J. I. (2013). BNCS report #3: full-scale structural and nonstructural building system performance during earthquakes and post-earthquake fire – camera and analog sensor details. *Structural Systems Research Project Report Series, SSRP 13/11*. University of California San Diego, La Jolla, CA.

Park. R. & Paulay, T. (1975) Reinforced concrete structures. New Jersey: John Wiley and Sons.

Restrepo, J. I., Seible, F., Stephan, B., & Schoettler, M. J. (2006). Seismic testing of bridge columns incorporating high-performance materials. *ACI Structural Journal*, *103*(4), 496.

Restrepo, J. I., & Bersofsky, A. M. (2011). Performance characteristics of light gage steel stud partition walls. *Thin-Walled Structures*, *49*(2), 317-324.

Restrepo, J., & Lang, A. F. (2011). Study of loading protocols in light-gauge stud partition walls. *Earthquake Spectra*, *27*(4), 1169-1185.

Rodriguez, M. E., Restrepo, J. I., & Blandon, J. J. (2006). Shaking table tests of a four-story miniature steel building-model validation. *Earthquake Spectra, 22*(3), 755-780.

Rosenblueth, E., & Arciniega, A. (1992). Response spectral ratios. *Earthquake Engineering & Structural Dynamics, 21*(6), 483-492.

Tobita, J., Izumi, M., & Katukura, H. (1988). Identification of vibration systems and nonlinear dynamic characteristics of structures under earthquake excitations. *Proceedings of Ninth World Conference on Earthquake Engineering*, vol. 5, 337-342.

Trifunac, M. D., Ivanovic, S. S., & Todorovska, M. I. (2001). Apparent periods of a building. I: Fourier analysis, *Journal of Structural Engineering, 127*(5), 517-526.

Welch, P. D. (1967). The use of fast Fourier transform for the estimation of power spectra: a method based on time-averaging over short, modified periodograms. *IEEE Trans. Audio Electroacoustics*, *15*(2), 70 -73.

Wu, Y. M., Hsiao, N. C., & Teng, T. L. (2004). Relationships between strong ground motion peak values and seismic loss during the 1999 Chi-Chi, Taiwan earthquake. *Natural Hazards, 32*(3), 357-373.

Chapter 4

RESPONSE OF A HIGH DAMPING RUBBER BEARING TO MULTIAXIAL EXCITATION

4.1 Abstract

A high damping rubber bearing fabricated as part of a seismic isolation system was tested at the Caltrans Seismic Response Modification Device Test Facility located at the University of California, San Diego. The purpose of the test program, which consisted of 33 tests, was to assess the impact of axial force rate, pitch rate, shear strain rate and multiaxial excitation on the response of the bearing. The bearing was tested in all six degrees of freedom (uncoupled and coupled) and tested dynamically to failure. This chapter examines the hysteretic response of the bearing to the different tests. Data obtained from these tests can help engineers understand the effects of coupling when calibrating or validating analytical models.

4.2 Introduction

In current U.S. design practice, prototype testing of seismic isolators is required to determine and verify the design parameters that are used in analysis and design calculations. While the seismic isolation design process is an evolving field, some of the common design parameters used in practice, include: the energy dissipated per cycle or the equivalent viscous damping ratio, the secant (effective) stiffness, and the peak force for a given shear strain. For this reason, these design parameters will be used in this chapter to quantify the differences in the bearing's response to a variety of inputs. In the United States, unidirectional prototype testing is required by both the AASHTO Guide Specifications for Seismic Isolation Design (1999) and ASCE 7-10 and ASCE 7-16 (2010, 2016). Wind resistant testing is also outlined in these provisions but will not be discussed in this chapter. For seismic loading, ASCE 7-10 requires a minimum of six unidirectional tests (ASCE 7-16 has the option of a minimum of three) for two representative bearings at various shear strains. If the seismic isolator is load bearing, then four additional unidirectional tests are required at two different constant axial loads to verify vertical load stability. ASCE 7-10 and ASCE 7-16 also stipulate that if the response of the seismic isolator is velocity dependent or bilateral load dependent, then additional testing is required. The AASHTO Guide Specifications for Seismic Isolation Design requires prototype testing for two representative isolators consisting of at least 13 fully reversed cyclic unidirectional tests each as well as vertical load stability tests. To account for bidirectional motion, the bearing could be rotated at 45 degrees in one of the tests. For design, AASHTO and ASCE use property modification factors to account for effects such as aging, temperature, velocity, and others. While a plethora of data is collected during prototype testing, there are not clear guidelines for interpreting the results and separating the different effects to obtain property modification factors. The European Standard for anti-seismic devices (EN 15129, 2010) requires 11 tests to verify the isolator behavior. One of these tests is bidirectional, following a “clover leaf” path, however, there is also an option to perform this test as two perpendicular unidirectional tests. Even though results are specific to each manufactured bearing, very seldom is data from prototype testing made public to create a database that would aid in the calibration and validation of analytical models.

Since prototype testing is largely performed with unidirectional or bidirectional excitation under a constant axial load, this implies that the engineering design parameters are verified only from the bearing's response to these loading conditions. Despite this, the installed seismic isolators are expected to experience multiaxial excitation at various strain rates. It is important to understand how strain rate, and excitation in each of the six degrees of freedom will affect the performance parameters established through prototype testing. This chapter outlines the test protocol, and discusses results determining the influence of axial force rate, pitch rate, shear strain rate and multiaxial excitation on the performance of one kind of seismic isolator: a high damping rubber (HDR) bearing.

4.3 Literature Review

A number of experiments have been conducted on high damping rubber materials and bearings to understand the behavior of the materials and of the devices as a whole. Experimental programs to investigate the strain rate dependence (Aiken et al., 1992; Morgan et al., 2001; Amin et al., 2002; Tsai et al., 2003; Yoshida, 2004; Amin et al., 2006; Dall'Asta & Ragni, 2006, 2008; Bhuiyan et al., 2009), nonlinear stress-strain relationship and coupling effects (Morgan et al., 2001; Abe et al., 2004; Burtscher & Dorfmann, 2004; Yamamoto et al., 2012), axial load effects (Aiken et al., 1992; Abe et al., 2004), relaxation rates (Amin, 2001, 2002), temperature (Hwang & Hsu, 2001; Itoh et al., 2006), and response to seismic excitation (Kikuchi & Aiken, 1997; Hwang & Ku, 1997; Hwang & Wang, 1998; Chaudhary et al., 2001).

The Mullins effect, also known as scragging, which is characterized by a reduction in stiffness following the first (few) cycles, stress softening with increasing shear strains, and the apparent strain history memory, was first observed in 1903

(Bouasse & Carriere) and thoroughly studied by Mullins (1948, 1969), is the subject of many experiments and research including different aspects of the effect such as the relaxation or recovery rate, the tensile cyclic, effect of temperature (Rigbi, 1980; Govindjee & Simo, 1992; Lion, 1996, 1997; Morgan et al., 2001; Laraba-Abbes et al., 2003; Burtscher & Dorfmann, 2004; Cantournet et al., 2009; Diani et al., 2009; Drozdov, 2009; Violaine, 2015). While the concentration and grade of fillers contained in the high damping rubber impacts the characteristics of the material, there is not a general consensus on what is physically causing some of the phenomena observed. Some researchers associate the main cause of the Mullins effect with bond ruptures (both physical and chemical bonds), while others reject this hypothesis due to the recovery rate and thermal impact on recovery, and instead attribute the phenomena to molecules slipping over the fillers and reforming bonds. The effect is observed in virgin (never before tested) rubber as well as rubber that has been untested for a period of time, which has led to the concern that Mullins effects will be present in the first or first few cycles of a bearing during when an earthquake occurs. Despite the uncertainties that still exist with high damping rubber, it is the opinion of the authors that the impact of the Mullins effect can be accounted for in design if proven significant and overall this effect does not outweigh the benefits of using HDR bearings to protect structures from earthquake damage.

4.4 Test Program

4.4.1 Description of the Test Specimen

The test specimen is an HDR bearing with a 650 mm diameter containing a 100 mm diameter hollow core. The bearing consists of 34 rubber layers and 33 steel shims for a total height of 303 mm, and a total rubber height of 204 mm (Figure 4.1) which resulted in a shape factor of 22.9. The bearing had a Shore hardness of around 60A. The HDR bearing had been incorporated in two testing series prior to this test protocol, including unidirectional quasi-static prototype testing by the manufacturer up to a shear strain, calculated as the lateral displacement of the bearing divided by the total rubber height (204 mm), of 152%, and shake table testing in a full-scale five story building test program, where the shear strain and shear strain rate reached 155% and 455 %/s, respectively (Chen et al., 2013, 2016, 2017). The bearing had been manufactured in November 2011, the shake table testing took place in April 2012 and the testing program described in this chapter occurred in June 2014 - 31 months (2.6 years) after the bearing was manufactured and 26 months (2.2 years) after the shake table tests.

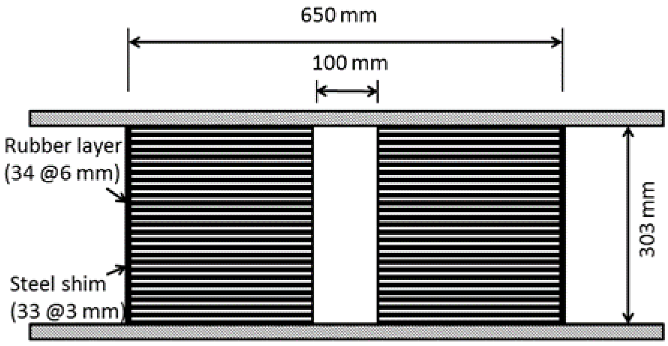

Figure 4.1: Main bearing dimensions.

4.4.2 Testing Apparatus

The Seismic Response Modification Device (SRMD) Test Facility consists of a moving platen capable of dynamic excitation in six degrees of freedom (Shortreed et al., 2001). The test specimen is attached to the moving platen below and to a fixed cross beam above (Figure 4.2). The notation for each degree of freedom is shown in Figure

4.3. The facility has a lateral displacement capacity in the longitudinal (H1) and transverse (H2) directions of ±1.2 m and ±0.61 m, respectively; a vertical compression force capacity of 53.4 MN; a ±1.8 m/s, ±0.76 m/s, and ±0.25 m/s velocity capacity in the H1, H2 and vertical directions, respectively; and a ±2 degree capacity in all three rotational degrees of freedom.

SRMD uses a total of 16 hydraulic actuators to move the platen: 4 horizontal actuators control the lateral displacements and 12 vertical actuators provide vertical load, platen rotation, and stability. An accumulator bank provides hydraulic oil in pressure to supply the actuators for the required high performance. The complex interaction between actuators is managed by an ad-hoc digital controller and software. Horizontal motions are commonly performed in displacement control while the vertical load is maintained to the desired levels through a force control approach.

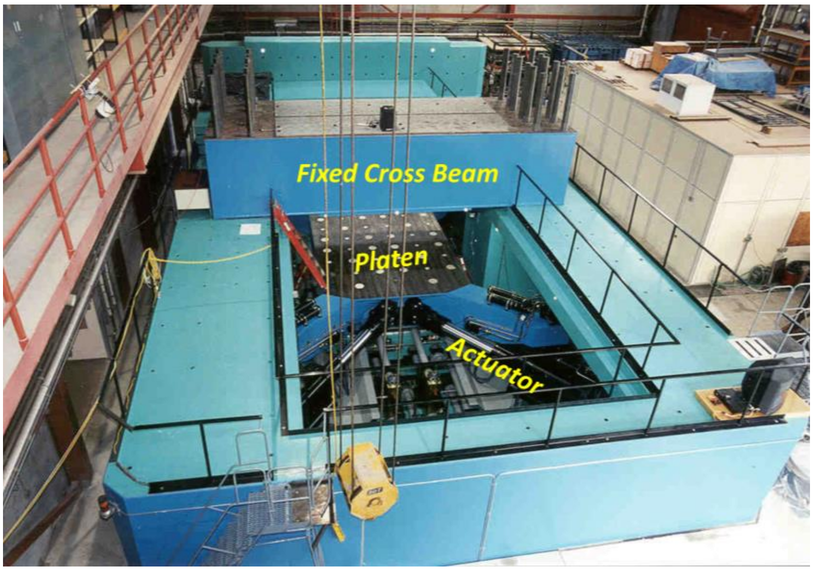

Figure 4.2: View of the SRMD testing facility.

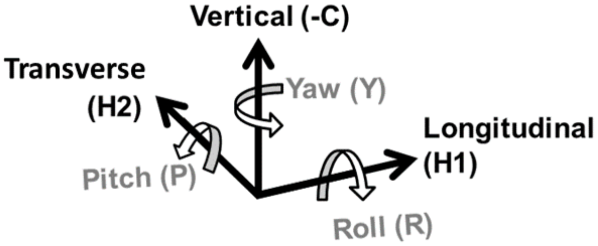

Figure 4.3: Degrees of freedom notation.

4.4.3 Test Protocols

The test protocols were designed to characterize the bearing in each degree of freedom and to observe the influence of strain rate (shear, axial, pitch), multiaxial loading, including axial load, bidirectional loading, and rotation, on the response of the HDR bearing. The test protocols are detailed in Table 4.1, which includes the number of degrees of freedom with dynamic input excitation, the input waveform, peak amplitude and velocity for each degree of freedom, and compressive force. Physical clearance as well as the available oil volume in the blow-down system of the SRMD facility posed some limitations, which shaped some of the maximum inputs (velocity, number of cycles and rotation angle) for some of the test protocols. The peak input displacements for the H1 and H2 directions were 305 mm (150% shear strain) and 153 mm (75% shear strain), respectively. The peak input angles for pitch and roll were 0.25 degrees and 0.125 degrees, respectively. These peak values chosen for input angles exceeded those measured from the shake table test, which were measured as less than 0.02 degrees. The peak input yaw angle was 1.6 degrees, corresponding to 4.5% bearing torsional strain. The compressive forces for all tests were chosen based on the highest (2.5 MN or an axial pressure of 7.7 MPa) and lowest (0.78 MN or an axial pressure of 2.4 MPa) compressive forces felt during the strongest shake table test motion (Chen et al., 2013, 2016). The three peak input shear strain rates in the H1 direction were 313 %/s, 469 %/s, and 750

%/s, which correspond to peak velocities of 0.638 m/s, 0.957 m/s, and 1.53 m/s, respectively.

Table 4.1: Test protocol.

			Peak Amplitude (Peak Input Velocity) for Degree of Freedom					
Test no.	DOF	Wave-form	H1 mm (mm/s)	H2 mm (mm/s)	P °θ (°θ/s)	R °θ (°θ/s)	Y °θ(°θ/s)	C (kN)
1	H1	sine	305 (638)					2489
2	H1	sine	305 (63.8)					2489
3	C	var. sine						778-2489
4	C	var. sine						778-2489
5	C	var. sine						778-2489
6	H1	var. sine	305 (638)					2489
7	H1	var. sine	305 (958)					2489
8	H1	var. sine	305 (1532)					2489
9	H1	var. sine	305 (638)					778
10	Y	var. sine					1.61 (3.38)	2489
11	Y	var. sine					1.61 (5.07)	2489
12	Y	var. sine					1.61 (8.12)	2489
13	Y	var. sine					1.61 (3.38)	778
14	P	var. sine			0.25 (0.53)			2489
15	P	var. sine			0.25 (0.79)			2489
16	P	var. sine			0.25 (1.26)			2489
17	P	var. sine			0.25 (0.53)			778
18	H1	sine	305 (638)					2489
19	H1+P	var. sine	305 (629)		0.25 (0.53)			2489
20	H1+P	var. sine	305 (647)		0.25 (0.53)			2489
21	H1+Y	var. sine	305 (638)				1.61 (3.38)	2489
22	H1+C	seismic motion	221 (614)					778-2489
23	H1+C	seismic motion	320 (925)					778-2489
24	H1+H2	elliptic	305 (63.8)	153 (32.0)				2489

Table 4.1 continued

25	H1+H2	elliptic	305 (638)	153 (319)				2489
26	H1+H2	elliptic	305 (958)	153 (479)				2489
27	H1+H2	elliptic	305 (1532)	153 (766)				2489
28	H1+H2	elliptic	305 (638)	153 (319)				778
29	H1+H2 +P+R	elliptic	305 (638)	153 (319)	0.25 (0.52)	0.125 (0.26)		2489
30	H1+H2 +P+R+ Y	elliptic	305 (638)	153 (319)	0.25 (0.52)	0.125 (0.26)	1.61 (3.38)	2489
31	H1+H2 +P+R+ Y+C	elliptic	305 (638)	153 (319)	0.25 (0.52)	0.125 (0.26)	1.61 (3.38)	778-2489
32	H1	sine	305 (638)					2489
33	H1	sine	610 (1282)					2489

Note: H1: Longitudinal displacement.
H2: Transverse displacement.
C: Axial compressive force.
P: Pitch (rotation about H2 axis).
R: Roll (rotation about H1 axis).
Y: Yaw (rotation about vertical axis).

Three different input waveforms or load patterns, see Figure 4.4, were used for almost all tests: sine waveform, variable amplitude sine waveform, and an elliptical orbit in the horizontal plane - which decomposes into sine waveforms in two orthogonal directions (full amplitude in one direction and half amplitude in the other direction). The variable amplitude sine waveform was created by applying a Hanning window to a sine waveform. This waveform was chosen in order to obtain data for varying amplitudes as well as 2.5 cycles at peak amplitude. For the tests with varying rates, the rates were determined by altering the period of the input waveform; a period of 3s, 2s and 1s were used for assessing rate dependency in certain degrees of freedom. The tests were performed with a minimum of about 0.5 – 1.0 hour between each test, with the temperature monitored using an infrared and digital thermometer, to ensure that a temperature build up did not occur.

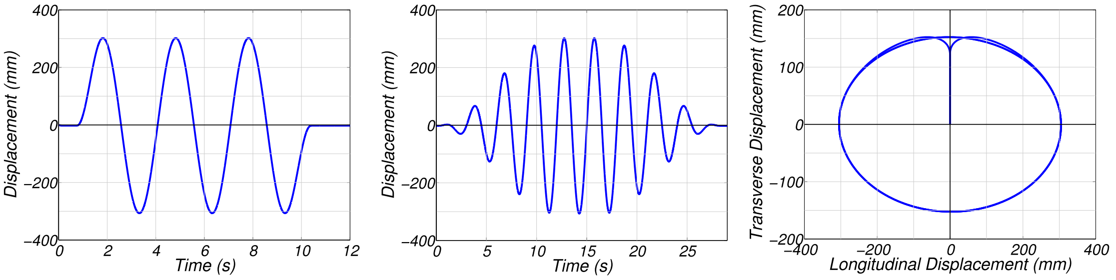

(a) (b) (c)

Figure 4.4: Sample input waveforms: (a) sine (b) variable amplitude sine (var. sine) (c) elliptic.

4.5 Test Results

4.5.1 Performance Parameters

In the following sections, several performance parameters, extracted from either the shear force – shear strain, axial force – axial strain, or pitch – bending moment response, are compared for different tests to assess the impact of various loading conditions. The performance parameters investigated include the peak positive and negative forces, the effective lateral stiffness – defined by ASCE 7-10 and ASCE 7-16 (2010; 2016) as:

$$k_{eff} = \frac{|F^{+}|+|F^{-}|}{|\Delta^{+}|+|\Delta^{-}|} \tag{4.1}$$

where F^+ and F^- are the peak positive and negative forces, respectively, and Δ^+ and Δ^- are the peak positive and negative displacements, respectively. The effective stiffness for the axial response is compared for various tests in this chapter using the following definition for the effective axial stiffness:

$$k_{eff,a} = \frac{|F_a{}^{+}|+|F_a{}^{-}|}{|\Delta_a{}^{+}|+|\Delta_a{}^{-}|} \tag{4.2}$$

where F_a^+ and F_a^- are the peak positive and negative axial forces, respectively, and Δ_a^+ and Δ_a^- are the peak positive and negative axial displacements, respectively. The effective pitch stiffness is also compared for various tests. The definition for the effective pitch stiffness used in this chapter is:

$$k_{eff,p} = \frac{|M_p{}^+|+|M_p{}^-|}{|\theta_p{}^+|+|\theta_p{}^-|} \tag{4.3}$$

where M_p+ and M_p- are the peak positive and negative pitch bending moments, respectively, and Θa+ and Θa- are the peak positive and negative pitch angles, respectively. Another parameter compared is the energy dissipated per cycle (EDC), which can be used to calculate an equivalent viscous damping ratio, as proposed by Jacobsen (1930) and used in various codes (ASCE 7-10, ASCE 7-16, AASHTO). A summary of results tabulating the relevant effective stiffness, maximum and minimum shear forces, as well as energy dissipated per cycle for all relevant tests is provided in Table 4.2.

Table 4.2: Summary of achieved results.

Test no.	K_{eff} (kN/mm)	Max shear force (kN)	Min shear force (kN)	Max displacement (mm)	Min displacement (mm)	Energy dissipated per cycle (kN-mm)
3	847	2469 (axial)	793 (axial)	10.1	8.10	366
4	874	2462 (axial)	798 (axial)	10.1	8.15	316
5	890	2438 (axial)	812 (axial)	10.0	8.18	288
6	0.71	217	-220	303	-308	50793
7	0.67	199	-214	304	-308	48523
8	0.65	198	-212	305	-309	54269
9	0.81	249	-246	303	-308	42338
14	597 (kN-m/°)					
15	567 (kN-m/°)					
16	516 (kN-m/°)					
17	421 (kN-m/°)					
18	0.71	233	-230	304	-308	48509
20	0.67	208	-209	307	-312	53554
21	0.69	210	-213	303	-308	48965
25	0.62	203	-196	303	-308	64922
26	0.63	206	-200	303	-308	66592
27	0.69	235	-221	304	-308	74476
28	0.73	233	-224	303	-307	54600
29	0.58	191	-190	307	-312	62817
30	0.58	188	-185	307	-312	62412
31	0.67	206	-227	307	-312	63601
32		216	-215	303	-308	

4.5.2 Test Repeatability

Reference tests (Test #18 and Test #32), which were similar in shear strain and waveform to the prototype testing carried out by the manufacturer, were also performed at different stages during the test protocol to check if the bearing had accumulated damage. While the prototype testing was performed quasi-statically and with a constant axial load of 2.2 MN rather than 2.5 MN for the reference tests, less than 10% variation between energy dissipated per cycle were found between the first cycle of both reference tests (Test #18 and #32) when compared to the prototype testing (as well as compared to each other), and less than 5% variation between the energy dissipate per cycle for the second cycle when compared to the prototype testing, see Figure 4.5a and Figure 4.5b, as well as compared to each other. The prototype test had a 6% and 14% higher effective lateral stiffness for the first loops in the H1 direction than that obtained from Test #18 and #32, respectively, and a 9% and 16% higher effective lateral stiffness for the second loops. The higher stiffness is expected due to the lower axial force during prototype testing, which will be discussed below.

Despite minimal differences between the response of the bearing during the two reference tests (Test #18 and #32), a physical difference was observed visually. At peak shear strain (150%), a slight bulge mid-height on the east side of the bearing is observed during the final reference test (Test #32), see the profile shown in Figure 4.5d, which was not visible at the peak shear strain during Test #18, see Figure 4.5c. This visible defect was a sign of fatigue which led to failure during the final test (Test #33).

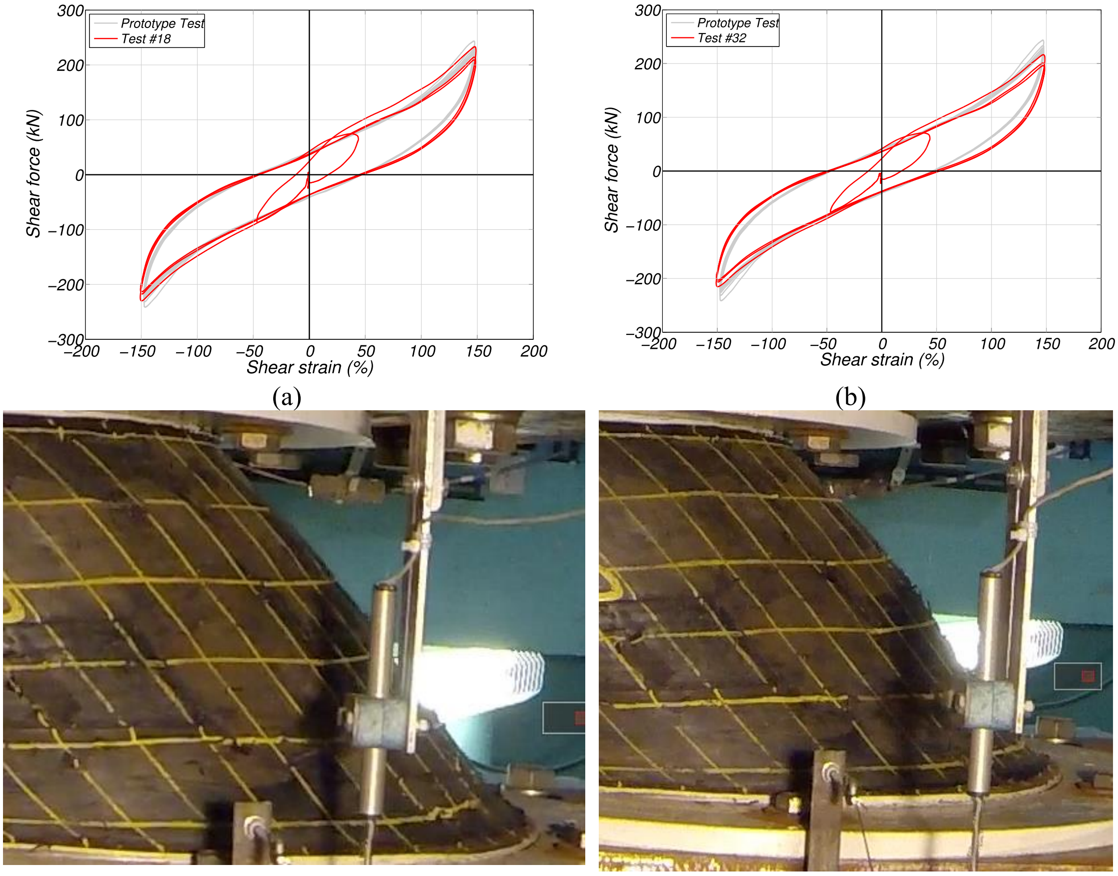

(a) (b)

(c) (d)

Figure 4.5: Prototype test with reference tests hysteretic response and video images from Test #18 (c) and Test #32 (d).

4.5.3 Axial Testing

To determine the compressive axial response characteristics of the bearing, Tests #3, #4 and #5 had only compressive axial load input, varying between 0.78 MN and 2.5 MN, corresponding to an axial pressure variation between 2.4 MPa and 7.7 MPa as seen in Figure 4.6. The three tests varied only in axial force rate, reaching peak instantaneous rates (lowpass filtered at 25 Hz) of 1.8, 2.7 and 4.4 MN/s in Tests #3, #4 and #5, respectively. For Tests #3, #4 and #5, the peak to peak shear strain rate reached 1.1, 1.6 and 2.5 MN/s, respectively. The rates during these tests correspond well to the rates achieved during the shake table tests, covering both the peak to peak axial strain rates as well as the peak instantaneous axial strain rates. The final, most intense shake test motion reached a peak to peak axial strain rate of 1.1 MN/s and a peak instantaneous axial strain rate of 3.9 MN/s. The axial force - axial strain hysteretic responses for the three tests are plotted in Figure 4.7. The axial stiffness is determined to be 847, 874 and 890 kN/mm for Tests #3, #4, and #5, respectively, which corresponds to only 3% and 5% increased effective axial stiffness when the peak axial force rate is increased by 50% (Test #4) and 144% (Test #5), compared to that calculated from Test #3. The energy dissipated per cycle at the peak force decreased as the axial force rate increased, decreasing by 14% to 316 kN-mm (Test #4) and by 21% to 288 kN-mm (Test #5) compared to Test #3 (366 kN-mm).

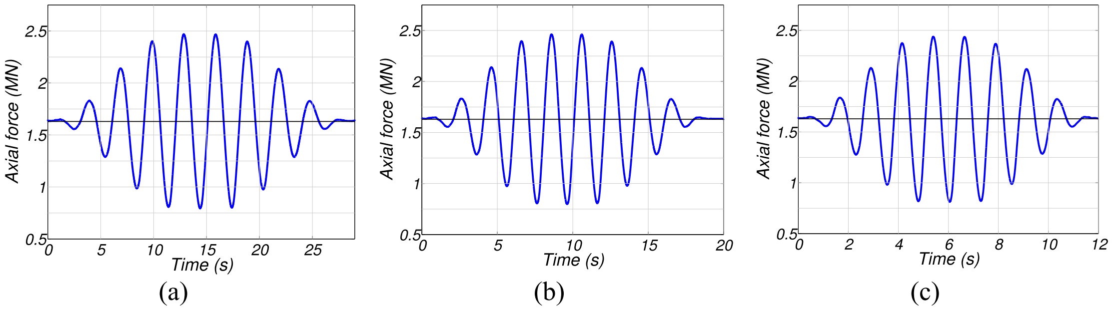

(a) (b) (c)

Figure 4.6: Axial force time histories for (a) Tests #3, (b) #4 and (c) #5.

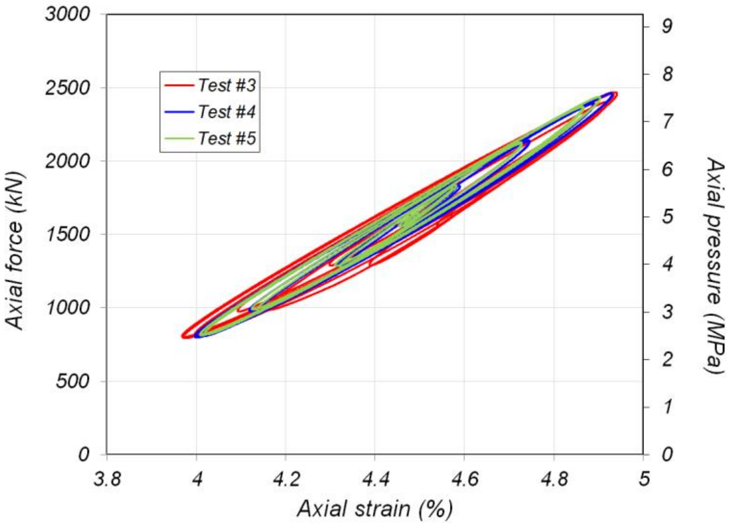

Figure 4.7: Axial force-axial strain hysteretic response for Tests #3, #4 and #5.

4.5.4 Pitch Testing

The bearing was also tested with reverse pitch motion as the only dynamic excitation. For these tests, the top of the test specimen is held static while the base is rotated. The rotation is measured as the relative rotation between the moving bottom platen with respect to the top static plate. To determine if the bearing response under this rotational motion was velocity dependent, Tests #14, #15 and #16, which were identical except for the input rotational velocity, were completed. The peak rotational velocity in Tests #14, #15 and #16 was 0.53, 0.79 and 1.26 °/s, respectively, see Table 4.1. The bending moment - rotation hysteretic response is plotted for Tests #14 - #16 in Figure 4.8a. The effective pitch stiffness is 597 kN-m/° during Test #14. Increasing the peak rotational velocity by 49% (Test #15) and 138% (Test #16) caused a decrease in effective pitch stiffness of 5% and 14%, respectively, see Table 4.2. This observed behavior warrants further investigation to fully understand the causes of these results.

Test #14 and #17 differed only in the constant axial load applied during the test to capture the impact of axial load on the moment-rotation hysteretic response. The moment-rotation hysteretic responses for Test #14 and #17 are plotted in Figure 4.8b. Decreasing the constant axial load by 69% (0.78 MN in Test #17 compared to 2.5 MN in Test #14) led to a 30% decrease in effective pitch stiffness. This decrease in constant axial load had a significant impact on the effective pitch stiffness; a lower axial load caused a decrease in effective pitch stiffness, which is the opposite effect for the effective lateral stiffness, as discussed later.

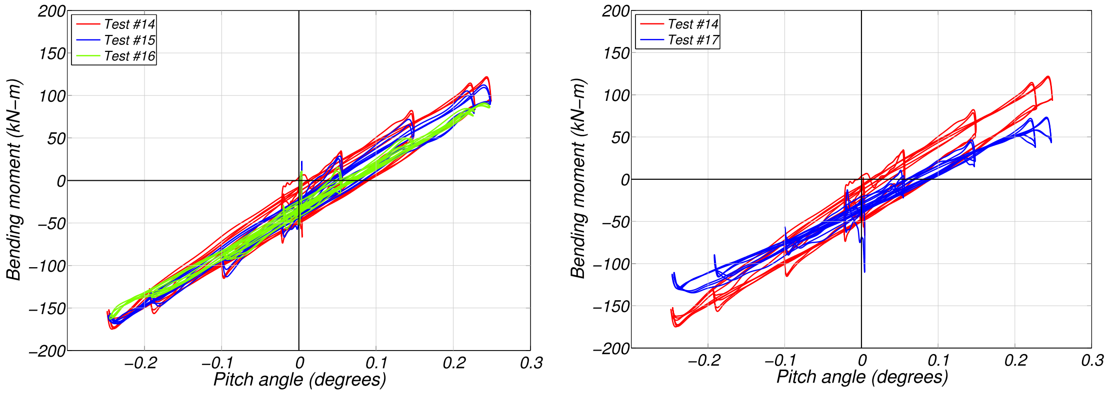

(a) (b)

Figure 4.8: Pitch moment-rotation hysteretic response.

4.5.5 Variable Amplitude Shear Strains

The effective shear stiffness of the bearing was assessed at various shear strains for one of the tests (Test #6), which had the variable amplitude shear strain input waveform. Since the positive and negative shear strain peaks varied in amplitude for each cycle below peak shear strain, see Figure 4.4 (b), the effective stiffness of the bearing was calculated as the peak positive or negative force divided by the peak positive or negative displacement in each direction. In total, five peaks occurred with the peak amplitude shear strain (~150%). The effective shear stiffness for these five peaks varied within 3% of the mean. In general, the average effective stiffness decreases steadily up to 100% shear strain and increases thereafter as the bearing shows hardening after 100% shear strain.

Degradation in effective stiffness due to load history is observed from Figure 4.9. The cycles in the first half of the test have a higher stiffness than the cycles at the same target shear strains in the second half of the test, suggesting a form of the Mullins effect. Not including the five peaks at ~150% shear strain, the effective stiffness at the shear strains during the first half of the test are on average 19% higher than those in the second half at the same shear strains, and up to 37% higher at the lowest (~15%) shear strain (Figure 4.9). Compared to the average effective stiffness at the maximum peak shear strain, the average stiffness at the lowest shear strain (~15%) is about 75% higher. The three average effective stiffness values at the subsequent shear strain peaks (~33%, 62%, 89%) below 100% shear strain decrease steadily from the stiffness at the lowest shear strain by 29%, 45% and 50%. As the bearing shows hardening after 100% shear strain, the effective stiffness starts to increase again. For the shear strains above 50%, the effective stiffness did not vary greatly; the average effective shear stiffness at these shear strains is 0.67 kN/mm, varying within 9% of the mean, and is only 5% less than the average stiffness of the peaks at ~150% shear strain (0.70 kN/mm).

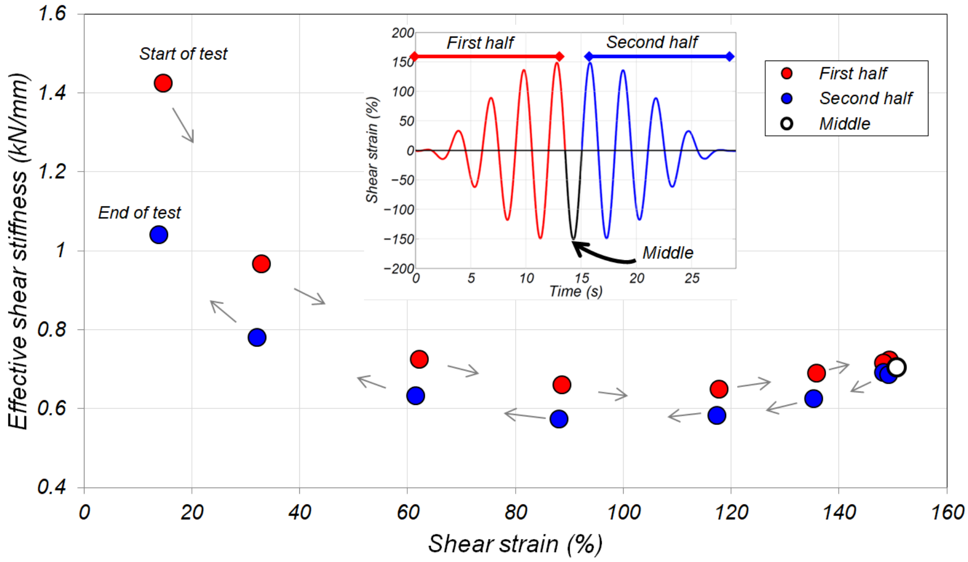

Note: arrows indicate sequence in which data points occurred during test.

Figure 4.9: Effective shear stiffness at various shear strains.

4.5.6 Bidirectional Lateral Testing

The longitudinal shear force - shear strain hysteretic response is compared in Figure 4.10a for Test #18, which had dynamic input in the longitudinal (H1) direction only, and Test #25, which had dynamic input in the longitudinal and transverse (H1 and H2) directions. The input for both Test #18 and #25 were identical in the H1 direction, with a peak displacement of 305 mm or 150% shear strain. Test #25 also had input in the H2 direction, which took the bearing to a peak displacement of 153 mm or 75% shear strain. During these tests, the bearing reached 13% and 15% lower peak forces in the positive and negative longitudinal direction, respectively, during bidirectional testing (Test #25) than during unidirectional testing (Test #18). The effective lateral stiffness in the H1 direction was also 12% lower during the bidirectional test (Test #25) than during the unidirectional test (Test #18). It is noted that according to ASCE 7-10 and ASCE 7-16, a 15% or greater difference in effective lateral stiffness calls for additional bidirectional testing (ASCE, 2010; ASCE, 2016).

A comparison between the energy dissipated per cycle is examined by comparing the areas of a single loop of the hysteretic shear force-shear strain response in the H1 direction (the second loop at peak shear strain). It is found that 34% more energy was dissipated per cycle in the H1 direction during bidirectional testing than during unidirectional testing, indicating path dependability and coupling. Another indication of path dependability and coupling in this HDR bearing is observed at zero longitudinal shear strain, where the force was 45% greater during the bidirectional test (Test #25) than during the unidirectional test (Test #18). It is noted that while zero longitudinal shear strain corresponds to zero total displacement for the unidirectional test (Test #18), it corresponds to a peak transverse displacement for the bidirectional test (Test #25). Experimental programs with bidirectional lateral input for HDR bearings investigated by Morgan et al. (2001), Abe et al. (2004a), Abe et al. (2004b) and Yamamoto et al. (2012) also displayed coupling effects in the two lateral directions, leading to the conclusion that caution must be taken when using unidirectional data directly for 3D modelling, even if the effective stiffness does not differ by more than 15%.

4.5.7 Lateral with Pitch, Roll and/or Yaw Testing

A series of tests were performed to observe any influence that pitch, roll, and yaw angles may have on the response of the HDR bearing when concurrently subjected to lateral loading. The input waveforms were designed such that the maximum pitch, roll, or yaw angle occurred at the peak displacements for each cycle. Figure 4.10b compares Test #6, which had dynamic input in the longitudinal direction only, with Test #20, which had dynamic input in the longitudinal direction as well as pitch. Moreover, Figure 4.10 (c) compares Test #6 with Test #21, which had input in the longitudinal direction as well as yaw. The peak positive and negative force decreased by 4% and 5%, respectively when the pitch component was introduced. The effective lateral stiffness in the H1 direction decreased by 6% with the addition of pitch in Test #20, while the energy dissipated per cycle increased by 5%, with respect to the performance without rotational motion. With the addition of yaw in Test #21, the peak positive and negative force, as well as the effective lateral stiffness in the H1 direction, decreased by 3%, and the energy dissipated per cycle decreased by 4%, in comparison to Test #6. Hence, any path dependency and coupling between these degrees of freedom appears to introduce negligible performance variations for this HDR bearing.

A similar comparison is made to understand the influence of adding pitch and roll or yaw to the bidirectional lateral input. In Figure 4.10d, Test #25, which had input in the H1 and H2 directions only, is compared with Test #29, which had input in the H1 and H2 directions plus concurrent pitch and roll input. The addition of pitch and roll caused a 6% decrease in effective lateral stiffness in the H1 direction and a 6% and 3% decrease in the positive and negative peak forces, respectively. The energy dissipated per cycle decreased by only 3% with the addition of pitch and roll. Test #30 had dynamic excitation in five degrees of freedom including the H1 and H2 directions, pitch, roll, and yaw. To isolate the effect of yaw, Test #30 is compared to Test #29, which had the same input as Test #30 minus the yaw input, in Figure 4.10e. The addition of yaw has a very minimal impact on the hysteretic response; the peak positive and negative forces only decreased by 1% and 2%, respectively, and the effective lateral stiffness in the H1 direction as well as the energy dissipated per cycle decreased by 1%. Figure 4.10f compares the test with input in only the H1 and H2 directions (Test #25) with the test with input in the H1 and H2 direction as well as all rotational degrees of freedom (Test #30), to assess the impact that excitation in all three rotational degrees of freedom has on horizontal bidirectional loading. It is found that compared to the test with bidirectional loading only (Test #25), the effective lateral stiffness in the H1 direction decreased by 7%, the peak positive and negative forces decreased by 8% and 5%, respectively, and the energy dissipated per cycle decreased by 4% when all three rotational degrees of freedom were introduced (Test #30). Overall, the addition of yaw, roll, and/or pitch had a negligible impact on the hysteretic shear force - shear strain response of the HDR bearing.

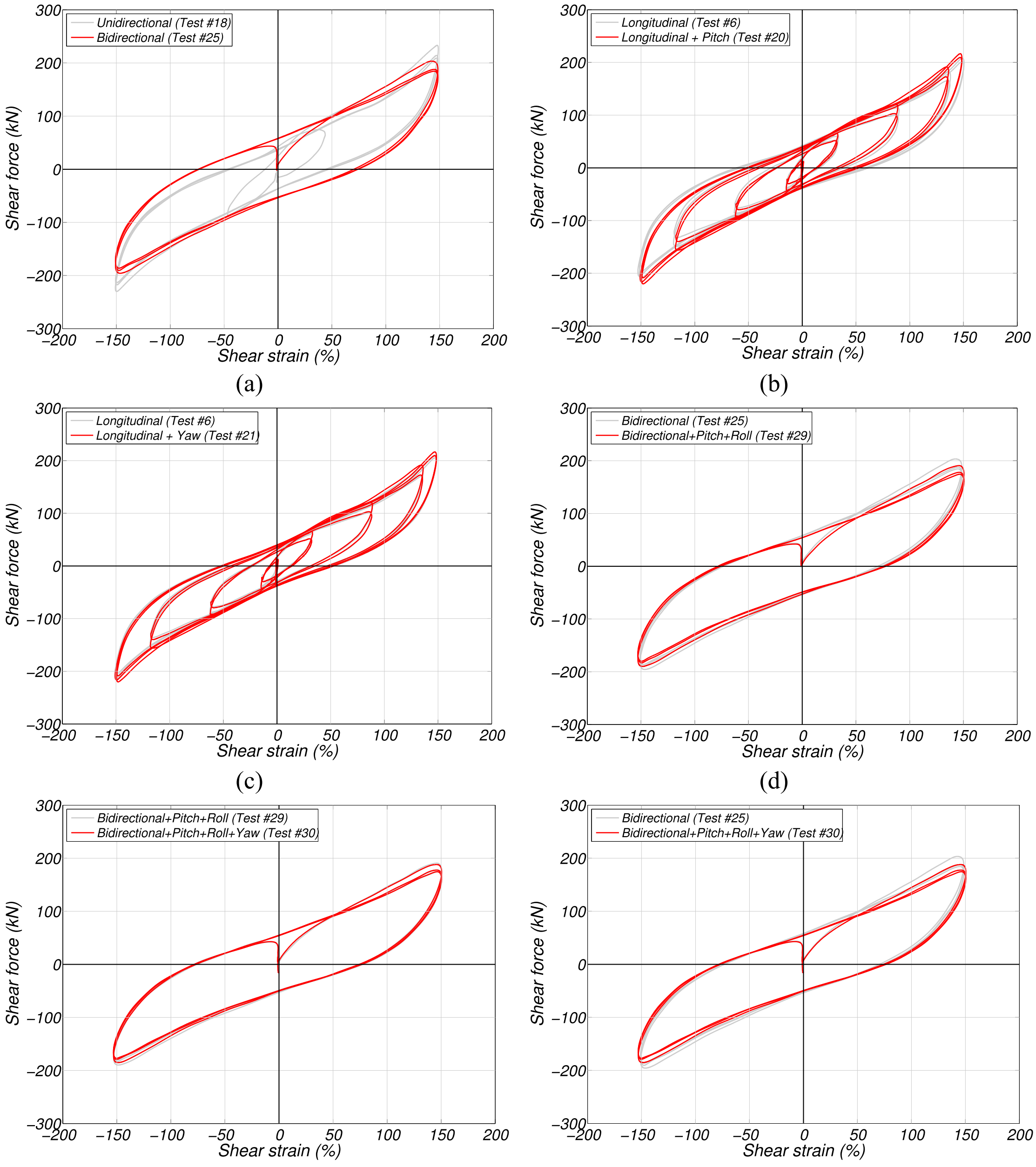

(a) (b)

(c) (d)

(e) (f)

Figure 4.10: Shear force-shear strain hysteretic response.

4.5.8 Lateral and Axial Testing

Prototype testing is typically performed under a prescribed axial load. A unidirectional test and a bidirectional test were performed under two different constant axial loads to understand the impact that axial load has on the bearing's performance. Figure 4.11a plots the hysteretic shear force - shear strain response from Tests #6 and #9, which differ only in the axial load. Test #6 was performed under a constant axial compressive load of 2.5 MN, corresponding to an axial compressive stress of 7.7 MPa, whereas Test #9 had a constant axial load of 0.78 MN (2.4 MPa). A reduction of 69% in axial load (Test #9 vs. Test # 6) resulted in a 14% increase in effective stiffness in the H1 direction as well as a 15% and 12% increase in the peak positive and negative forces, respectively. The energy dissipated per cycle, however, decreased by 17% with a 69% decrease in axial load (Test #9 vs. Test # 6).

Figure 4.12 plots the shear force - shear strain response of the part of the two unidirectional tests with the maximum and minimum axial loads (Test #6 and Test #9) from zero shear strain to the peak shear force. Using equilibrium in the deformed configuration of the bearing allows the P-Δ effects to be calculated and disaggregated from the overall response. If the rubber compound behaved linearly, the shear stress - shear strain relationships after disaggregation should be identical for the two cases, which is not the case.

Test #25 and Test #28 both had bidirectional lateral loading and differed only in the axial compressive load imposed. The hysteretic shear force-shear strain response during Test #25, with 2.5 MN constant axial load, or 7.7 MPa of axial pressure, is compared with Test #28, which had a 0.78 MN constant axial load, or 2.4 MPa of axial pressure, in Figure 4.11b. With a 69% reduction in axial load (Test #28), the bearing had a 17% higher effective stiffness in the H1 direction, and a 15% and 14% higher peak positive and negative force, respectively, and 16% less energy dissipated per cycle than with a greater axial load (Test #25). Similar experiments were reported by Aiken et al. (1992), which determined that varying the constant axial load affected both the effective lateral stiffness and energy dissipated per cycle. Decreasing the axial load by 69%, from

2.5 MN to 0.78 MN, impacted the unidirectional and bidirectional test results in a similar way – the effective stiffness increased while the energy dissipated per cycle decreased. The range of axial loads expected in design will impact the magnitude of these differences.

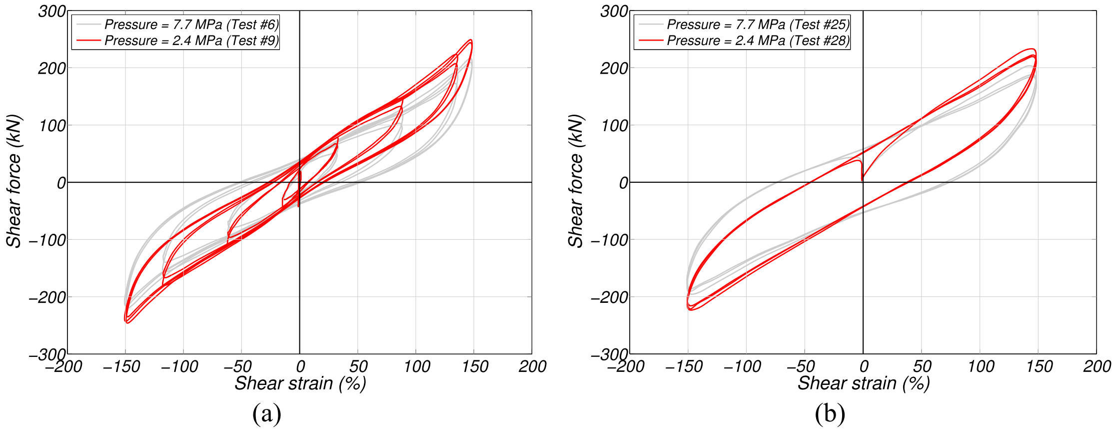

(a) (b)

Figure 4.11: Shear force-shear strain hysteretic response.

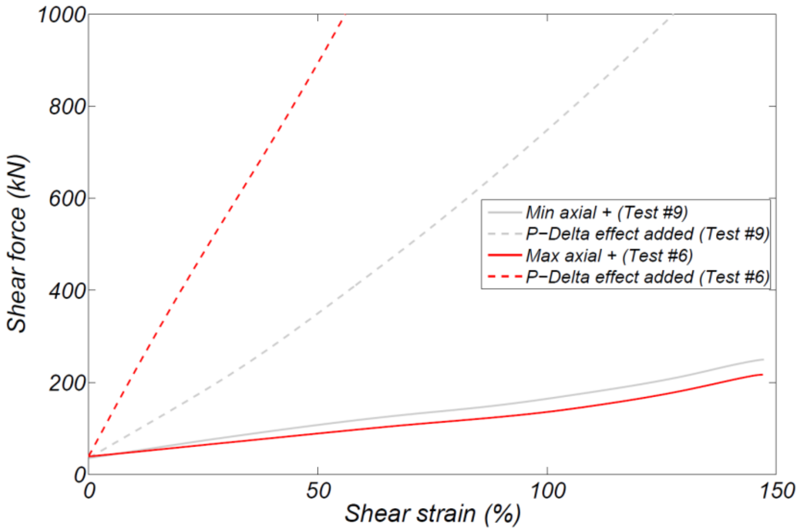

Figure 4.12: P-Delta effect removed from shear strain – shear force response.

4.5.9 Coupled Six Degree of Freedom Testing

While the tests described above demonstrate how variation in the constant axial load impacts the performance of the bearing, it is also important to understand how varying the axial load dynamically will impact the hysteretic response. Test #31 included dynamic excitation in all six degrees of freedom simultaneously. The axial force reached a maximum of 2.5 MN (7.7 MPa axial pressure) at the peak positive shear strain and reached a minimum axial force of 0.78 MN (2.4 MPa axial pressure) at the peak negative shear strain. To isolate the effects of varying the axial load on the bearing response, Test #31 is compared with Test #30 in Figure 4.13a - the only difference between the tests being that one had a constant axial load of 2.5 MN (Test #30), while the other (Test #31) had a an axial load in varying between 0.78 MN and 2.5 MN, see Figure 4.6a, with peak positive shear force corresponding to the highest axial load. By varying the axial load (Test #31), the effective stiffness in the H1 direction increased by 17%, the peak positive shear force increased by 9% and the peak negative shear force increased by 23%, while the energy dissipated per cycle increased by only 2%. Since the largest discrepancy occurs at the peak negative force and shear strain, Test #31 is compared to Test #28 in Figure 4.13b, with a constant axial force of 0.78 MN, which is the same peak axial force during Test #31 at the peak negative longitudinal displacement and peak negative shear force. Compared to the response of the bearing with 0.78 MN axial load (Test #28), the peak negative shear force only increased by 2% during with the test with dynamic excitation in all 6 degrees of freedom (Test #31), which is negligible.

To observe the impact that excitation in all six degrees of freedom has on the hysteretic response to bidirectional motion and unidirectional motion, the six degree of freedom test (Test #31) is compared to the bidirectional test with input in the H1 and H2 directions (Test #25) and to the unidirectional test with input in the H1 direction (Test #18) in Figure 4.13c and Figure 4.13d, respectively. Compared to the response in the bidirectional test (Test #25), the stiffness is increased by 9%, the peak positive shear force is only increased by 1%, while the peak negative force is increased by 16% and the energy dissipated per cycle is decreased by 2% during the six degree of freedom test (Test #31). To summarize the total effects of multiaxial dynamic excitation, Test #31 is compared to the uniaxial Test #18. With the addition of excitation in five degrees of freedom, the effective stiffness in the H1 direction increased by 5%, the peak positive shear force increased by 12%, whereas the peak negative shear force only increased by 1%, and the energy dissipated per cycle increased by 31% compared to the unidirectional test (Test #18). From these comparisons, it is observed that the coupling effects had the greatest impact on the response when Test #31 is compared to the unidirectional test (#18), and the axial load variation had the greatest impact on the response of the bearing when Test #31 is compared to the bidirectional test (#25), which is expected from the results from previous tests.

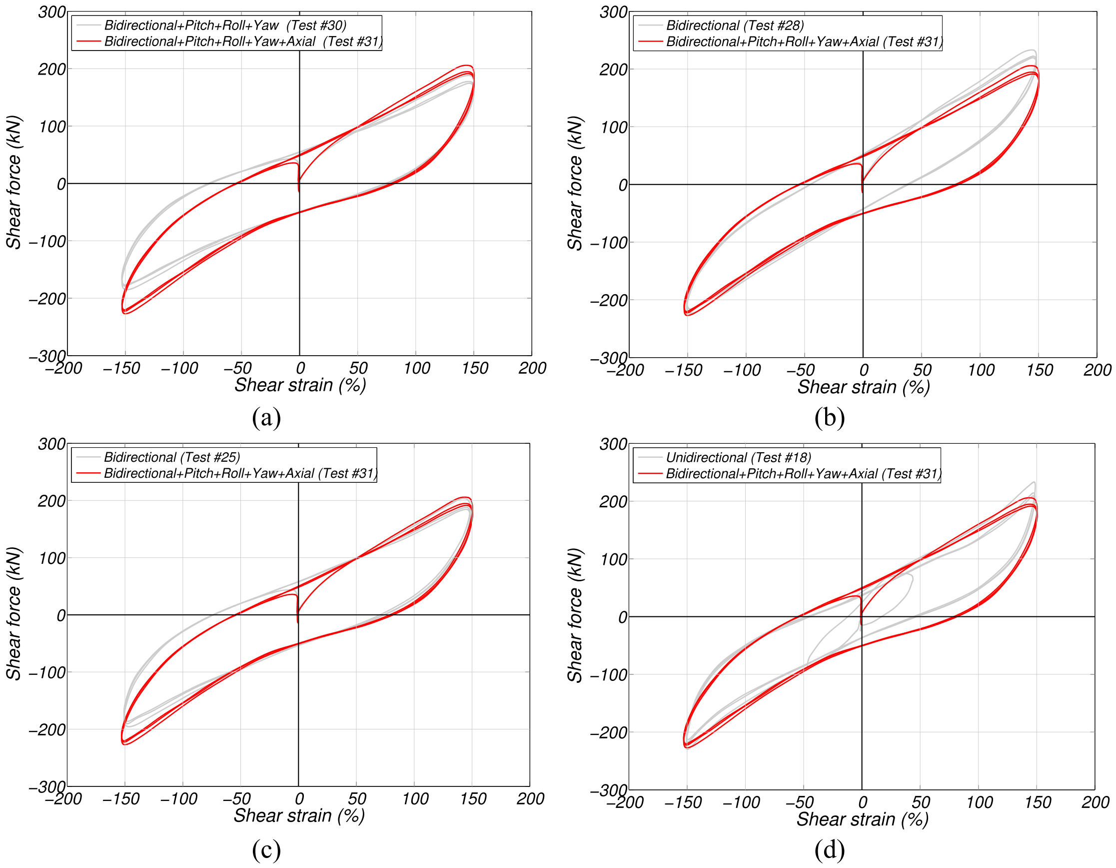

(a) (b) (c) (d)

Figure 4.13: Shear force-shear strain hysteretic response.

4.5.10 Shear Strain Rate Dependency

The shear strain rate dependency for unidirectional motion and bidirectional motion were assessed during Tests #6-8 and #25-27, respectively. Tabulated results can be found in Table 4.2 and Table 4.3. The peak instantaneous (lowpass filtered at 25 Hz) achieved shear strain rates for the unidirectional Tests #6, #7 and #8 were 315, 476, and 735 %/s, respectively, with peak to peak shear strain rates of 201, 300 and 483 %/s, respectively. The peak instantaneous achieved shear strain rate for the bidirectional Tests #25, #26, and #27 were around 313, 473, and 757 %/s, respectively, with peak to peak shear strain rates reaching 199, 302 and 477 %/s, respectively. For comparison with the shear strain rates from the shake table tests, the peak instantaneous shear strain rates for all test motions ranged from 146 %/s to 455 %/s. For the most intense shake table test, the peak to peak shear strain rate reached 165 %/s and 443 %/s. Figure 4.14a plots the hysteretic shear force-shear strain response for the unidirectional tests (Tests #6, #7 and #8). By increasing the peak shear strain rate by 51% (Test #7) and 133% (Test #8), the effective stiffness in the H1 direction decreased by 6% and by 8%, respectively, with respect to Test #6. The peak positive forces decreased by 8% for an increased peak shear strain rate of 51% and 133% (Tests #7 and #8) and the peak negative forces decreased by 3% and 4% for the increased peak shear strain rate of 51% and 133%, respectively, with respect to Test #6. Compared to Test #6, the energy dissipated per cycle decreased by 4% with a 51% increase in peak shear strain rate (Test #7) but increased by 7% with a 133% increase in peak shear strain rate (Test #8). For the bidirectional (input in both H1 and H2) tests, increasing the shear strain rate by 51% (Test #26) and by 142% (Test #27) caused an increase in effective stiffness in the H1 direction by 1% and 11%, respectively, in relation to Test #25, see Figure 4.14b. The peak longitudinal positive and negative shear forces increased slightly by 1% and 2%, respectively, for the 51% increased peak shear strain rate (Test #26), and increased by 16% and 13%, respectively, for the 142% increased peak shear strain rate (Test #27), when compared to Test #25. The energy dissipated per cycle also increased compared to Test #25, with 3% more energy dissipated per cycle with the 51% increased peak velocity (Test #26) and 15% with a 142% increased peak velocity (Test #27). Overall, it was found that the HDR bearing response was not heavily influenced by varying the shear strain rate, consistent with findings from experimental testing of HDR bearings reported by others (Aiken et al., 1992; Abe et al., 2004a; Yoshida et al., 2004; Constantinou et al., 2007), however, differing from findings by Morgan et al. (2001), which demonstrates the fact that results from specific bearings should not be generalized.

The shear force is plotted against the shear strain rate for the same tests discussed above in Figure 4.14c and Figure 4.14d, with an arrow indicating the direction of motion, and the peak positive and negative shear strain rates denoted with a color - coordinated circle, which also reflect the force at zero shear strain. As the shear strain rate increases, these peak values, tabulated in Table 4.3, are observed to be practically the same in the bearing; varying within 5% of the mean of maximum forces at peak velocities for the unidirectional tests with varying shear strain rates (Tests #6, #7 and #8), and within 16% of the mean for the bidirectional tests with varying shear strain rates (Tests #25, #26 and #27). From this observation, it can be concluded that there are no significant shear strain rate effects in this particular bearing.

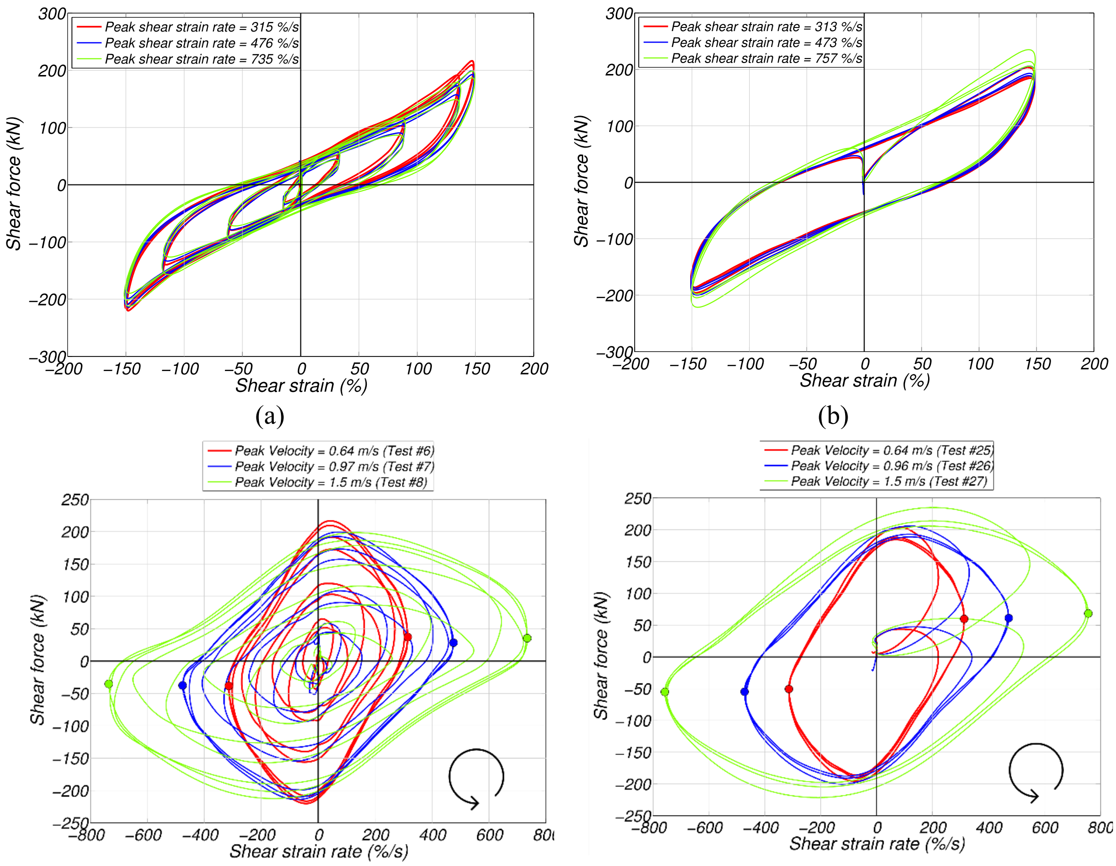

(a) (b)

(c) (d)

Figure 4.14 (a-b) Shear force-shear strain hysteretic response and (c-d) shear force-shear strain rate response.

Table 4.3: Peak shear strain rates and forces.

Test no.	Min shear strain rate (%/s)	Max shear strain rate (%/s)	Min force at peak shear strain rate (kN)	Max force at peak shear strain rate (kN)
6	-314	315	-38	37
7	-476	476	-38	28
8	-735	734	-35	35
25	-313	313	-51	60
26	-472	473	-55	61
27	-757	757	-55	68

4.5.11 Final Test to Failure

The final test in the program took the bearing to failure. The input motion dynamically took the bearing to 300% longitudinal shear strain, which was twice as much as the peak shear strain used for the other tests in this protocol, such as Test #32 – a reference test with a peak shear strain of 150%, plotted together in Figure 4.15. It is apparent that there is substantial hardening beyond 150% shear strain. Other testing protocols, which took high damping rubber bearings to failure, have been reported by Kelly (1991, 1992) and were performed monotonically. To determine when and where the bearing failed, video footage collected during the test was reviewed, see Figure 4.16. It is observed that the failure occurs near mid height of the bearing during the first loop before the bearing reaches the first positive peak shear strain. Bulging of the bearing was observed on the east side when the bearing was subjected to west loading (Figure 4.16a) and prior to the development of a mid-height crack between a steel plate – rubber layer interface, which occurred at 291% shear strain (Figure 4.16b). The crack widens as the bearing is subjected to east loading (Figure 4.16c) and continues to widen in the second cycle (Figure 4.16d). As the bearing approached the peak positive shear strain during the third loop (Figure 4.16e), the top and bottom half of the bearing completely separated (Figure 4.16f). Upon returning from this peak positive strain, the top and bottom half came in contact with each other, which required a very high force to overcome and reach the peak negative strain, causing a spike in the third loop.

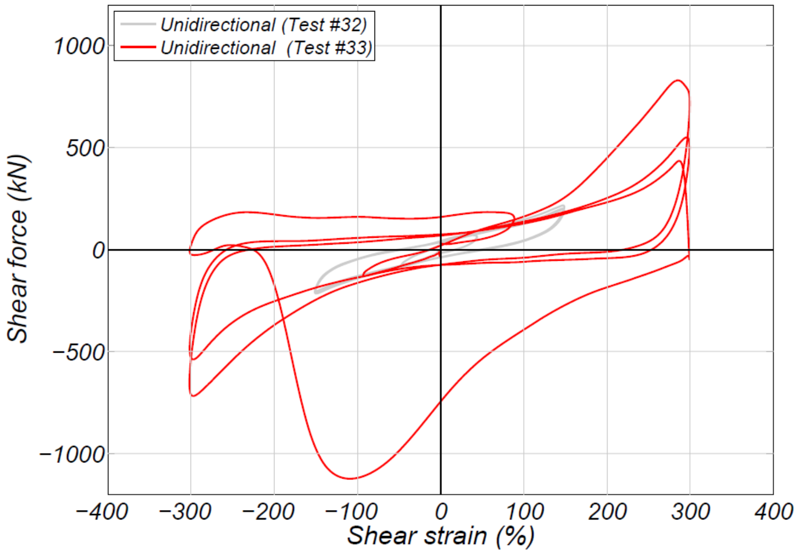

Figure 4.15: Shear force-shear strain hysteretic response for Tests #32 and #33.

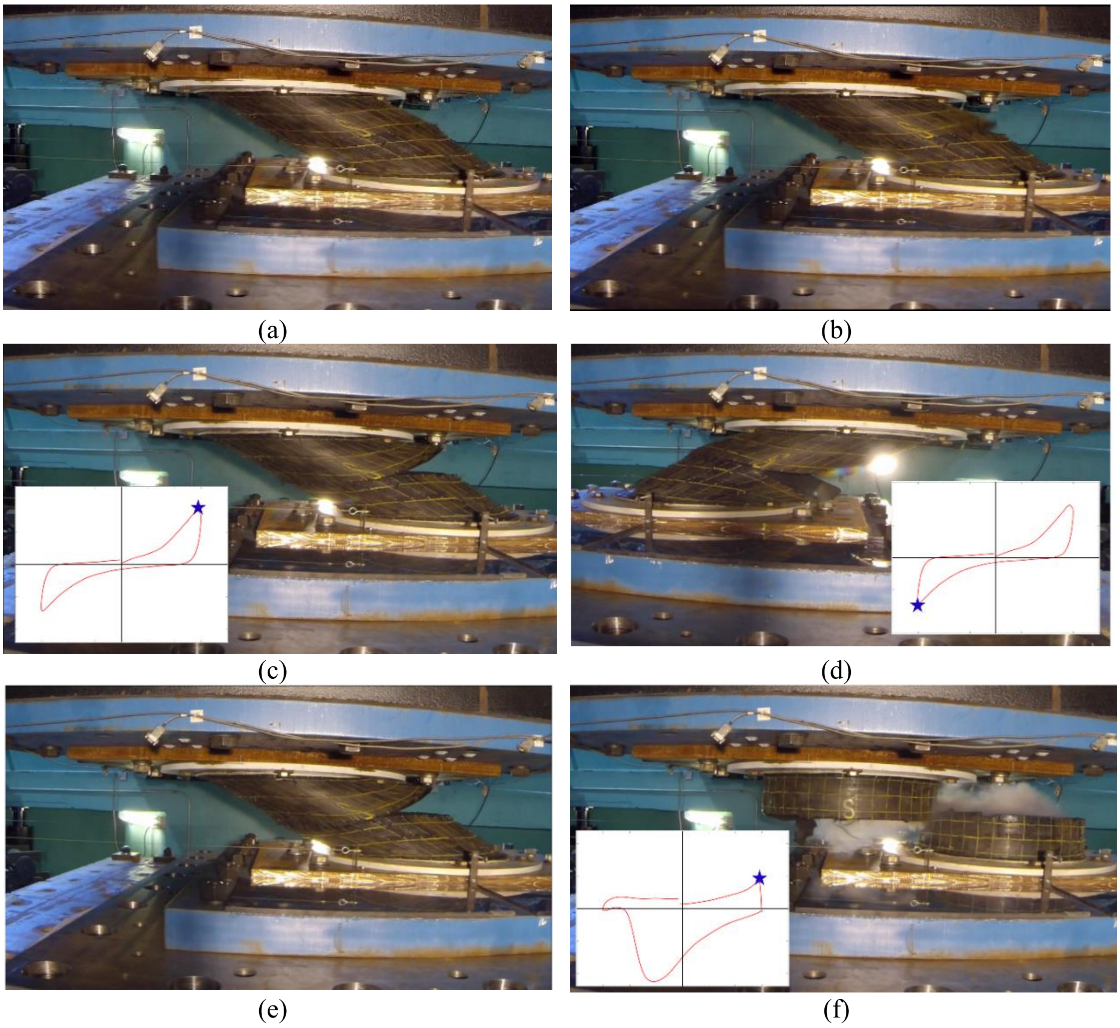
(a) (b) (c) (d) (e) (f)

Figure 4.16: Images from Test #33.

4.6 Conclusions

A full-scale high damping rubber bearing was subjected to an extensive experimental testing program. Performance parameters used in current design codes such as effective stiffness, energy dissipated per cycle, and peak forces are typically derived from unidirectional prototype testing. These test protocols were designed to assess the impact that shear strain rate, rotation, axial load, bidirectional motion, and multiaxial dynamic excitation have on the hysteretic response of a high damping rubber bearing and how the performance parameters (i.e. effective stiffness, energy dissipated per cycle, peak forces) are affected.

The test protocols started with uniaxial testing in each degree of freedom before coupling the inputs systematically until the bearing was tested with dynamic input in all six degrees of freedom. Consistent with previous experimental work, coupling between the two horizontal degrees of freedom was observed. With excitation in both horizontal degrees of freedom compared to unidirectional loading, the effective stiffness in the longitudinal direction and peak positive and negative shear forces decreased by an average of 12% and 14%, respectively, while the energy dissipated per cycle increased by 34%. The addition of dynamic excitation in the rotational degrees of freedom had less of an impact on the performance parameters, varying the properties by less than 10%. The axial load, however, did have a significant impact on the bearing’s shear force -shear strain hysteretic response for both unidirectional and bidirectional loading. For unidirectional loading, decreasing the constant axial load by 69% caused a 14% increase in effective stiffness in the longitudinal direction, an average of 13% higher peak forces, and a 17% decrease in energy dissipated per cycle. For bidirectional loading, the same decrease in axial load resulted in a 17% increase in effective stiffness in the longitudinal direction, an average of 14% increase in peak shear forces, and a 16% decrease in energy dissipated per cycle. Combining the inputs in each degree of freedom into a six degree of freedom test produced a response consistent with the expected impact from each degree of freedom individually on the unidirectional response. The greatest impact on the response was produced by the axial load and coupling effects from the bidirectional loading, however the effective stiffness in the longitudinal direction and peak forces did not differ from the unidirectional test nor the bidirectional test by more than 16%, whereas the energy dissipated per cycle increased by 31% compared to the unidirectional test and only decreased by only 2% compared to the bidirectional test.

For the final test, the target shear strain for the bearing was 300% which was twice as high as the peak shear strain achieved for previous tests. Significant hardening was observed beyond 150% shear strain, but the bearing failed before reaching a shear strain of 300%. The results presented in this chapter represent the response of a single bearing to a given test protocol. To generalize these results, many more test specimens would need to be tested and compared. The results can however be informative to design further experimental campaigns intended to assess performance modification factors and to validate numerical models under multiaxial dynamic excitations.

4.7 Acknowledgements

Component testing was partially supported by the National Science Foundation under IGERT Award #DGE-0966375, "Training, Research and Education in Engineering for Cultural Heritage Diagnostics". Support from the SRMD staff, Danny Innamorato and Ed Stovin, is greatly appreciated.

The work in this chapter has been prepared to be submitted for publication as Chen, M., Restrepo, J. I., and Benzoni, G. Response of a high damping rubber bearing to multiaxial excitation.

4.8 References

AASHTO (1999). Guide specifications for seismic isolation design. *American Association of State Highway and Transportation Officials*, Washington, D.C.

Abe, M., Yoshida, J., & Fujino, Y. (2004a). Multiaxial behaviors of laminated rubber bearings and their modeling. I: Experimental study. *J. Struct. Eng., 130*(8), 1119–1132.

Abe, M., Yoshida, J., & Fujino, Y. (2004b). Multiaxial behaviors of laminated rubber bearings and their modeling. II: Modeling. *J. Struct. Eng.*, *130*(8), 1133–1144.

Aiken, I., Kelly, J., Clark, P., Tamura, K., Kikuchi, M., & Itoh, T. (1992). Experimental studies of the mechanical characteristics of three types of seismic isolation bearings. *Proc, of the 10th World Conf. on Earthquake Engineering*.

Amin, A. F. M. S., Alam, M. S. & Okui, Y. (2002). An improved hyperelasticity relation in modeling viscoelasticity response of natural and high damping rubbers in compression: experiments, parameter identification and numerical verification. *Mechanics of Materials, 34*(2), 75-95.

Amin, A. F. M. S., Lion, A., Sekita, S., & Okui, Y. (2006). Nonlinear dependence of viscosity in modeling the rate-dependent response of natural and high damping rubbers in compression and shear: Experimental identification and numerical verification. *International Journal of Plasticity, 22*(9), 1610-1657.

ASCE/SEI. (2010). Minimum design loads for buildings and other structures*, SEI/ASCE 7-10,* American Society of Civil Engineers, Reston, VA.

ASCE/SEI. (2016). Minimum design loads for buildings and other structures*, SEI/ASCE 7-16,* American Society of Civil Engineers, Reston, VA.

Benzoni, G. & Casarotti, C. (2009). Effects of vertical load, strain rate and cycling on the response of lead-rubber seismic isolators. *Journal of Earthquake Engineering, 13*(3), 293-312.

Bhuiyan, A. R., Okui, Y., Mitamura, H., & Imai, T. (2009). A rheology model of high damping rubber bearings for seismic analysis: Identification of nonlinear viscosity. *International Journal of Solids and Structures*, *46*(7), 1778-1792.

Bouasse, H. & Carriére, Z. (1903). Sur les courbes de traction du caoutchouc vulcanisé. *Annales de la faculté des sciences de Toulouse 2e série*, *5*(3), 257-283.

Burtscher, S. L., & Dorfmann, A. (2004). Compression and shear tests of anisotropic high damping rubber bearings. *Engineering structures, 26*(13), 1979-1991.

Cantournet, S., Desmorat, R., & Besson, J. (2009). Mullins effect and cyclic stress softening of filled elastomers by internal sliding and friction thermodynamics model. *International Journal of Solids and Structures, 46*(11), 2255-2264.

Chaudhary, M. T. A., Abé, M., & Fujino, Y. (2001). Performance evaluation of base-isolated Yama-agé bridge with high damping rubber bearings using recorded seismic data. *Engineering Structures, 23*(8), 902-910.

Chen, M., Pantoli, E., Astroza, R., Ebrahimian, H., Mintz, S., Wang, X., Hutchinson, T., Conte, J., Restrepo, J., Meacham, B., Kim, J., & Park, H. (2013). BNCS report #1: full-scale structural and nonstructural building system performance during earthquakes and post-earthquake fire - specimen design, construction and test protocol. *Structural Systems Research Project Report Series, SSRP 13/9*. University of California San Diego, La Jolla, CA.

Chen, M., Pantoli, E., Wang, X., Astroza, R., Ebrahimian, H., Hutchinson, T., Conte, J., Restrepo, J., Marin, C., Walsh, K., Bachman, R., Hoehler, M., Englekirk, R., & Faghihi, M. (2016). Full-scale structural and nonstructural building system performance during earthquakes: part I – specimen description, test protocol and structural response. *Earthquake Spectra, 32*(2), 737-770.

Chen, M., Astroza, R., Restrepo, J. I., Conte, J. P., Hutchinson, T., & Bock, Y. (2017). Predominant period and equivalent viscous damping ratio identification for a full-scale building shake table test. *Earthquake Engineering and Structural Dynamics, 46*(14), 2459-2477.

Constantinou, M. C., Whittaker, A. S., Kalpakidis, Y., Fenz, D. M., & Warn, G. P. (2007). Performance of seismic isolation hardware under service and seismic loading. *MCEER-07-2012.*

Dall’Asta, A. & Ragni, L. (2006). Experimental tests and analytical model of high damping rubber dissipating devices. *Engineering Structures, 28*(13), 1874-1884.

Dall’Asta, A. & Ragni, L. (2008). Nonlinear behavior of dynamic systems with high damping rubber devices. *Engineering Structures, 30*(12), 3610-3618.

Diani, J., Fayolle, B., & Gilormini, P. (2009). A review on the Mullins effect. *European Polymer Journal, 45*(3), 601-612.

Drozdov, A. D. (2009). Mullins’effect in semicrystalline polymers. *International Journal of Solids and Structures, 46*(18), 3336-3345.

EN 15129 (2010), European standard for anti-seismic devices, European Committee for Standardization.

Govindjee, S. & Simo, J. (1992). Transition from micro-mechanics to computationally efficient phenomenology: carbon black filled rubbers incorporating Mullins' effect. *Journal of the Mechanics and Physics of Solids, 40*(1), 213-233.

Hwang, J. S. & Ku, S. W. (1997). Analytical modeling of high damping rubber bearings. *J. Struct. Eng., 123*(8), 1029-1036.

Hwang, J. S. & Wang, J. C. (1998). Seismic response prediction of HDR bearings using fractional derivative Maxwell model. *Engineering Structures, 20*(9), 849-856.

Hwang, J. S. & Hsu, T. Y. (2001). A fractional derivative model to include effect of ambient temperature on HDR bearings. *Engineering structures, 23*(5), 484-490.

Itoh, Y., Gu, H., Satoh, K., & Yamamoto, Y. (2006). Long-term deterioration of high damping rubber bridge bearing." *Doboku Gakkai Ronbunshuu A, 62*(3), 595-607.

Jacobsen, L. S. (1930). Steady forced vibrations as influenced by damping. *Trans. ASME, 52*(15), 169-181.

Kelly, J. M. (1991). Dynamic failure characteristics of Bridgestone isolation bearings." *Report No. UCB/EERC–91/04*, University of California, Berkeley.

Kelly, J. M. (1992). Technology transfer package on seismic base isolation – Vol. II: failure mechanisms in isolators. *Proceedings, Department of Energy short course on seismic base isolation*, Berkeley, California.

Kikuchi, M. & Aiken, I. (1997). An analytical hysteresis model for elastomeric seismic isolation bearings. *Earthquake Engineering and Structural Dynamics, 26*(2).

Laraba-Abbes, F., Ienny, P., & Piques, R. (2003). A new 'Tailor-made'methodology for the mechanical behaviour analysis of rubber-like materials: II. Application to the hyperelastic behaviour characterization of a carbon-black filled natural rubber vulcanizate. *Polymer, 44*(3), 821-840.

Lion, A. (1996). A constitutive model for carbon black filled rubber: experimental investigations and mathematical representation. *Continuum Mechanics and Thermodynamics, 8*(3), 153-169.

Lion, A. (1997). A physically based method to represent the thermos-mechanical behavior of elastomers. *Acta Mechanica,* 123, 1-25.

Lomiento, G., Bonessio, N., & Benzoni, G. (2012). Effects of loading characteristics on the performance of sliding isolation devices. *Proceedings, 15th World Conference on Earthquake Engineering.*

Morgan, T., Whittaker, A., & Thompson, A. (2001). Cyclic behavior of high-damping rubber bearings. *Proceedings, 5th World Congress on Joints, Bearings and Seismic Systems for Concrete Structures.*

Mullins, L. (1948). Effect of stretching on the properties of rubber. *Rubber chemistry and technology*, *21*(2), 281-300.

Mullins, L. (1969). Softening of rubber by deformation. *Rubber chemistry and technology*, *42*(1), 339-362.

Rigbi, Z. (1980). Reinforcement of rubber by carbon black. *Properties of Polymers*, 21-68.

Shortreed, J. S., Seible, F., Filiatrault, A., & Benzoni, G. (2001). Characterization and testing of the Caltrans seismic response modification device test system. *Philosophical Transactions: Mathematical, Physical and Engineering Sciences, 359*(1786), 1829-1850.

Violaine, T., Tam, N. Q., & Christophe, F. (2015). Experimental study on high damping rubber under combined action of compression and shear. *Journal of Engineering Materials and Technology, 137*(1), 011007.

Yamamoto, M., Minewaki, S., Yoneda, H., & Higashino, M. (2012). Nonlinear behavior of high-damping rubber bearings under horizontal bidirectional loading: full-scale tests and analytical modeling. *Earthquake Engineering and Structural Dynamics, 41*(13), 1845-1860.

Yoshida, J., Abe, M., & Fujino, Y. (2004). Constitutive model of high-damping rubber materials. *Journal of Engineering Mechanics*, *130*(2), 129-141.

Chapter 5

SEISMIC DESIGN FRAMEWORK FOR INERTIA-SENSITIVE NONSTRUCTURAL COMPONENTS IN BASE ISOLATED BUILDINGS

5.1 Abstract

Damage to nonstructural components and building systems during earthquakes can lead to significant economic losses, immediate evacuation, and long downtimes. Failure of these components can also threaten the safety of building inhabitants. Many regions in the world that have suffered from structural and nonstructural seismic damage have opted to incorporate base isolation in building designs to protect buildings and their contents from earthquake damage. As base isolation of buildings becomes more widespread, especially for hospitals, museums, emergency centers, and other buildings with critical functions and/or valuable contents, it is necessary to understand the response of nonstructural components and have a guide for designing these components within base isolated buildings.

In current design practice, there are no design provisions specific to nonstructural components within base isolated buildings. This chapter describes a framework to calculate the design force for nonstructural components within base isolated buildings that utilizes displacement damage limit states of the components and explains the process

with a case study that combines experimental structural responses with simulated nonstructural responses using inelastic floor response spectra.

5.2 Introduction

Nonstructural components and systems make up a large part of the overall building investment, comprising about 65-85% of a conventional building’s initial cost (Taghavi & Miranda, 2003; FEMA, 2012). Damage to these components often leads to costly repairs, loss of functionality of the facility, downtime, and can pose a threat to the safety of the building occupants. In recent earthquakes, repeatedly observed damage to nonstructural components has demonstrated that there is a need for improvement in the predicted response and the design of these components (Baird et al., 2014; Hutchinson et al., 2010; Miranda et al., 2012). Some regions that have experienced these losses are increasing the use of base isolation in building design to diminish the damage to the building system as well as its contents (namely, Chile, Ecuador, Italy, Japan, New Zealand, Peru, Turkey). Many of the base isolated buildings either contain sensitive contents and equipment that cannot be damaged, or are facilities that must remain operational after an earthquake, such as emergency centers and hospitals. In both cases, it is essential to prevent damage to nonstructural components, and/or retain functionality of the equipment. Current code requirements, however, do not have nonstructural design provisions specific to base isolated buildings; the design of these components is often based on standards established for conventional fixed base buildings.

In many countries, an emphasis is placed on classifying nonstructural components as either acceleration-sensitive or drift/deformation-sensitive (FEMA 1997). Following a code-based approach (such as ASCE7-16 or Eurocode 8), acceleration-sensitive nonstructural components are designed using accelerations in a forced-based design procedure, in which displacements are not checked. This can mislead engineers to believe that displacement demands of acceleration-sensitive nonstructural components are negligible. Results from analysis, shown in this chapter, indicate that the displacement demands for nonlinear nonstructural components can be significant, even in a base isolated building. To emphasize these findings (without redefining the causes of damage to nonstructural components outlined by FEMA, 2005), the authors propose a reclassification of nonstructural components as inertia-sensitive and racking-sensitive (to replace the terms “acceleration-sensitive” and “drift/deformation-sensitive,” respectively), where forces and deformations are addressed in the design of both groups. This chapter discusses the framework for the design of inertia-sensitive nonstructural components, which is based on known or estimated damage displacement limit states of the nonstructural components. The framework is then applied to a case study using nonlinear floor displacement response spectra results with experimental data from a building base isolated with high damping rubber bearings and tested at UC San Diego’s large high performance outdoor shake table (Van den Einde et al., 2004).

5.3 Literature Review

There is a limited amount of research on the seismic response of nonstructural components within a base isolated building. A majority of this research focuses on predicting the peak floor responses of base isolated buildings and comparing the responses to fixed base buildings. Analyses using experimental results and simulated results to predict the performance of nonstructural components attached to base isolated structures have confirmed that, while some base isolation systems are more effective than others, base isolated buildings in general are effective at reducing the response of nonstructural components when compared to fixed base buildings (Kelly & Sackman, 1979; Sackman & Kelly, 1980; Kelly & Tsai, 1985; Tsai & Kelly, 1988; Tsai & Kelly, 1989; Fan & Ahmadi, 1990; Ahmadi & Su, 1992, Fan & Ahmadi, 1992; Juhn & Constantinou, 1992; Hernried & Lei, 1993; Inaudi & Kelly, 1993; Hernried & Lei, 1995; Kelly, 1999; Wolff & Constantinou, 2004; Politopoulos, 2008; Huang et al. 2010; Isakovic et al., 2011; Politopoulos & Pham, 2011; Engelen et al., 2014; Kelly & Marisco, 2015).

Acceleration response spectra for linear response has often been used to estimate the response of equipment attached to base isolated buildings (Sackman & Kelly, 1980). Moreover, experimental programs, carried out by Kelly and Tsai (1985; Tsai & Kelly 1989), concluded that the attenuated building response eliminated the need to include inelastic response of the high frequency components. Kelly and Tsai cautioned that equipment forces that may introduce higher mode contributions, can increase with the inclusion of energy dissipation devices, which was also concluded through floor acceleration response spectra for linear response by: Kelly (1999), Kelly and Marisco (2015), Yang et al. (2010), Isakovic et al. (2011), and Politopoulos and Pham (2011), all of which proposed solutions for mitigating this issue. Experimental programs by Wolff and Constantinou (2010) focused on comparing the peak responses from different isolation systems as well as a fixed base system, concluding that isolation systems with higher nonlinearity were not in fact detrimental to the equipment response.

5.4 Proposed General Framework

A proposed framework for the design of nonstructural components within a base isolated building is outlined in this section and in a flowchart in Figure 5.1. This framework is a general guideline for the overall process, identifying the key parameters necessary in the method. The method will be calibrated using a case study of an experimental building with a high damping rubber base isolation system as well as simulated nonlinear nonstructural component responses later in the chapter.

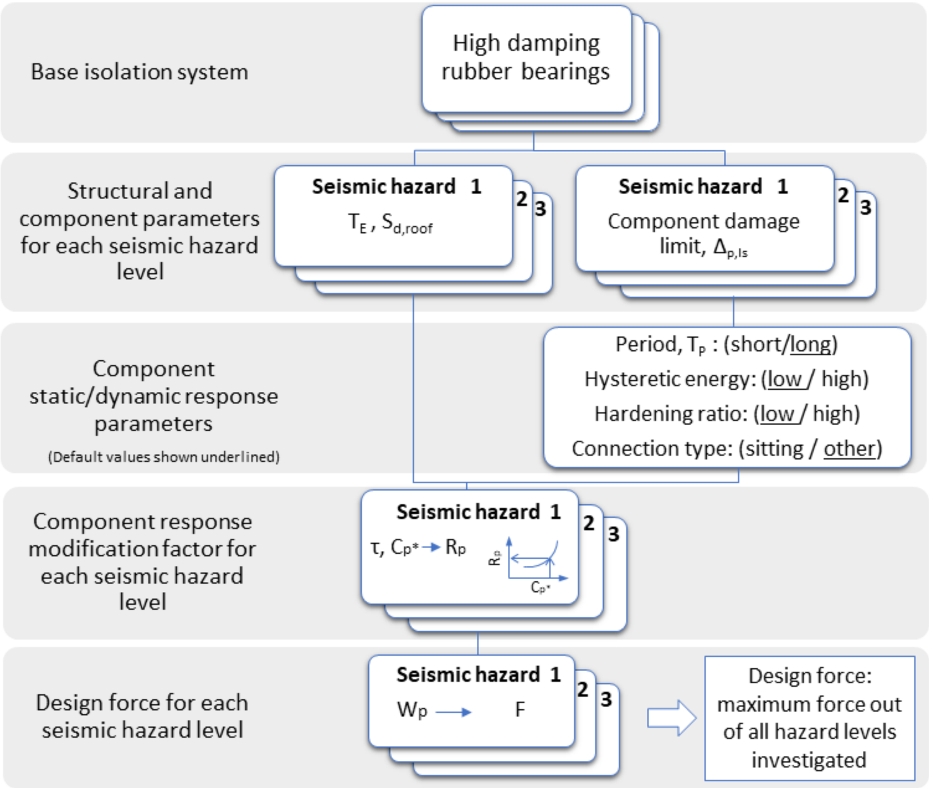

Figure 5.1: Design guideline flowchart.

It is necessary to first define the type of base isolation system that the building will utilize, since different types of base isolation systems can result in different floor spectral acceleration and spectral displacement demands (Skinner, 1993). The framework results in a design force, which is not based on an initial component response modification factor, R_p, for a given nonstructural component, as it is in the ASCE 7-16 (2016) standard (or importance and behavior factors as it is in Eurocode 8 [2003]). Instead, the framework starts with defining key structural parameters corresponding to the various seismic hazard levels, including the building's predominant or effective period, T_E, as well as the expected peak roof displacement, $S_{d,roof}$.

For the nonstructural component, a displacement damage limit state, $\Delta_{p,ls}$, must be defined for each seismic hazard level considered. An allowable displacement is an intuitive value to estimate, as opposed to accelerations and forces; the designers of the nonstructural components must predict what amount of movement is considered acceptable for a given seismic hazard level.

Next, the response modification factor for the nonstructural component, R_p, is calculated using the key structural and nonstructural parameters for a specific seismic hazard level. The equations for the R_p factor are calibrated using the floor displacement response spectra for inelastic response. This factor, R_p, is a function of the damage limit state of the nonstructural component, $\Delta_{p,ls}$, the peak roof displacement, $S_{d,roof}$, and the ratio of the predominant period of the component, T_p, to the effective period of the building, T_E.

Additional information about the nonstructural component can also be incorporated into the calibration process to obtain component-specific response parameters, however, default values can be used if specific information is unknown. Parameters investigated that impact the floor displacement response spectra for inelastic response at very short periods include: the period of the component, T_p, the hysteretic energy dissipation response characteristics of the component, and the post-elastic hardening ratio of the component's hysteretic response. Moreover, if the component sits on the floor (instead of hanging), then a reduced gravitational force may be relied upon for hysteretic energy dissipation via friction, which will limit the value of R_p, as shown later.

After the component response modification factor, R_p, is calculated, the nonstructural component lateral design force, F_p, is evaluated. This design force is a function of the R_p factor for the component, the effective period of the building, T_E, the peak roof displacement, $S_{d,roof}$, and the operating weight of the component, W_p. To determine the governing design force of the nonstructural component, this process is repeated for all the seismic hazard levels considered.

5.5 Case Study

5.5.1 UC San Diego Five-Story Building Shake Table Test Program

A case study is investigated using data recorded from a full-scale five-story building shake table test program conducted at the University of California, San Diego large high performance outdoor shake table. Details on the building and test program are found in Chen et al. (2016; 2017). This case study makes use of acceleration data recorded during the base isolation testing phase, which involved subjecting the building to a series of earthquake ground motions of increasing intensity, while the building was base isolated using high damping rubber isolators (Chen et al., 2016). It is noted that any structural-nonstructural component interaction is ignored for this analysis. While analysis results for this chapter are based on structural response data from this experimental test program in conjunction with simulated data for nonstructural component hysteretic responses, the calibration process can be repeated for any similar set of experimental data and/or data from computational simulations.

The shake table test protocol for the base isolated building consisted of seven ground motions with varying intensity. For this chapter, the first (BI1), fourth (BI4), and last (BI7) ground motions are be investigated. The spectral accelerations and spectral displacements of these motions for a linear response are shown in Figure 5.2 for a 12% equivalent viscous damping ratio (which was used in the design of this building-isolation system). The predominant or effective period, T_E, of the building-isolation system is found by Chen et al. (2017) for the motions investigated. The initial effective period, found from ambient vibration, is 0.85s (Astroza et al., 2016; Chen et al., 2017). During BI1, the isolators reached a peak shear strain, γ, of 46%, calculated as the ratio of the peak relative displacement of the isolators to the total rubber height (204 mm), and the effective period during this test was found to be T_E = 2.42s. The peak shear strain in BI4 was 69%, with an effective period of 2.70s. For the final motion, BI7, the peak shear strain was 155% and the effective period reached 3.16s.

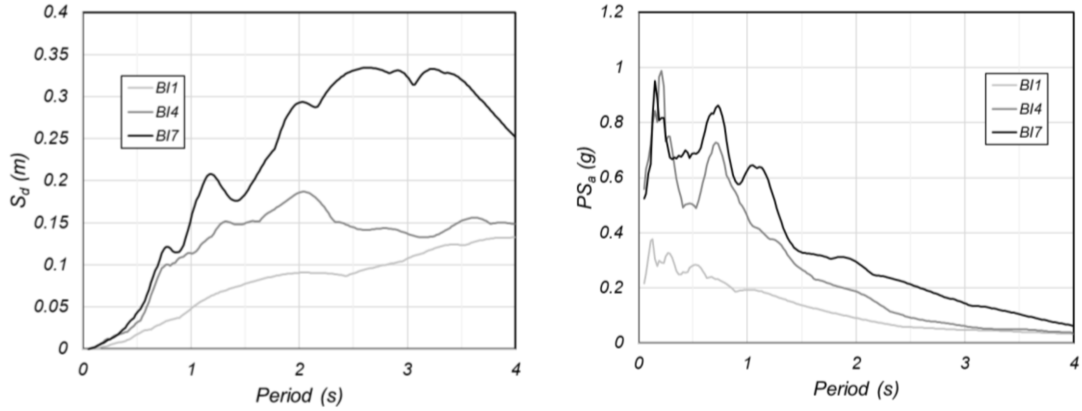

(a) (b)

Figure 5.2: (a) Spectral displacement and (b) pseudo spectral acceleration for linear response to input ground motions for ζ = 12%.

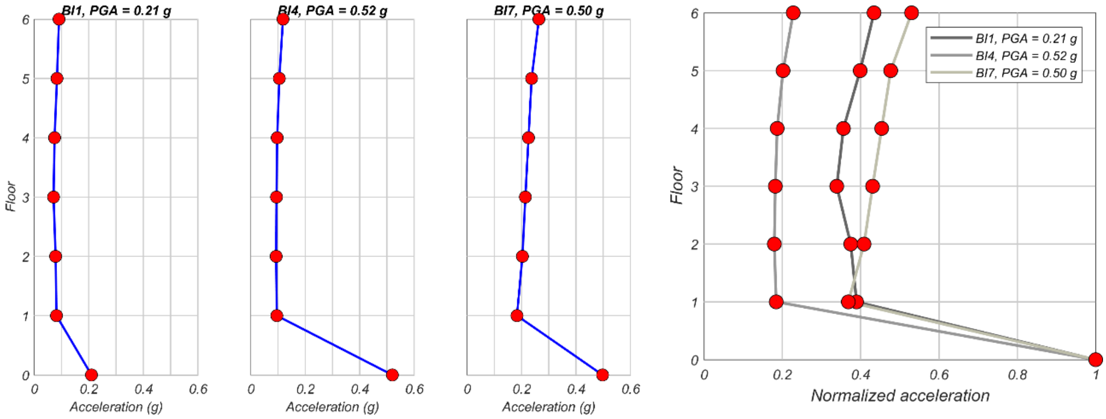

(a) (b)

Figure 5.3: (a) Peak floor accelerations for earthquake ground motions BI1, BI4, BI7 and (b) normalized by the peak ground accelerations.

The ground or input acceleration time histories are shown along with the floor acceleration responses for the first, third and roof levels in Figure 5.4. An inset at the roof level shows the response for 15 seconds in each motion at the same scale to illustrate the elongation of T_E. It is observed that much of the high frequency content is not transmitted above the isolation plane and that the floor accelerations are only a fraction of the accelerations at the ground level. This is further illustrated in Figure 5.3a-b, which shows the peak ground and floor accelerations, as well as the peak accelerations, normalized by the peak ground acceleration for each earthquake motion. It is observed that between the ground level and the first floor, the acceleration is attenuated to 20-40% of the peak ground acceleration, and that the peak floor response is nearly constant from the first floor to the roof, with the exception of BI7, which has some amplification at the higher levels.

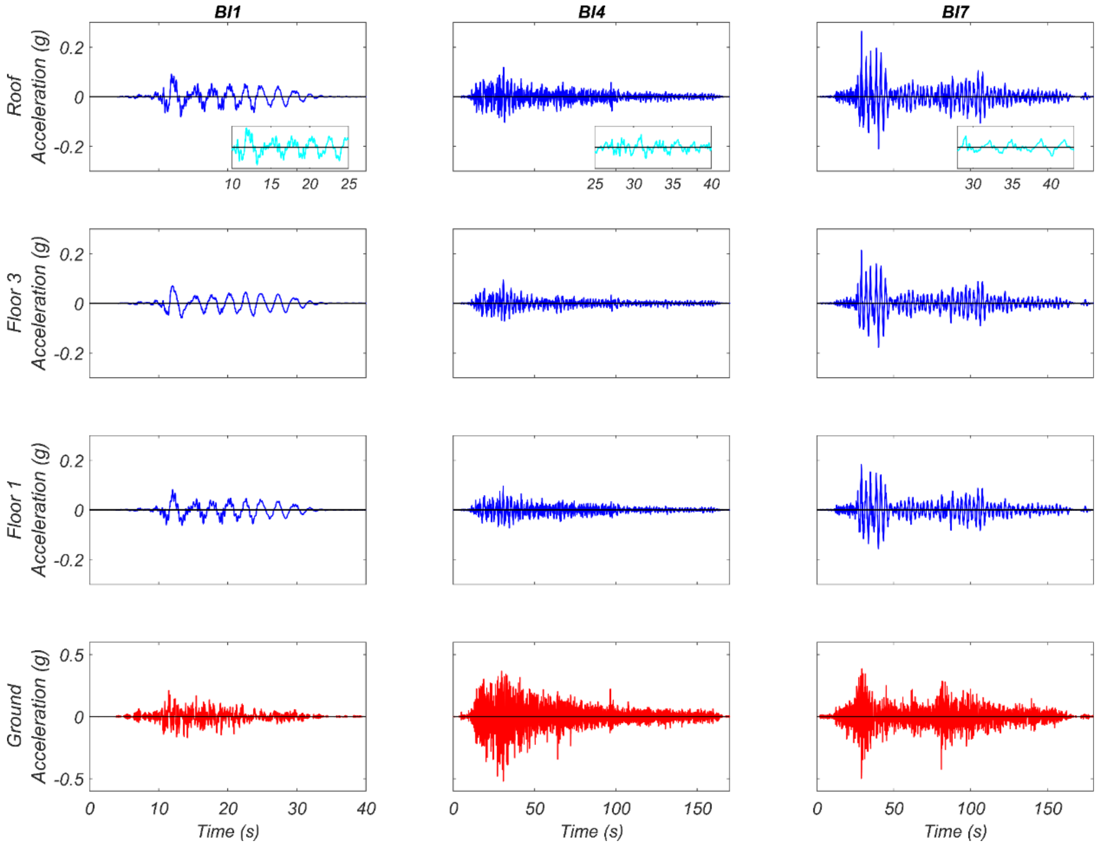

Figure 5.4: Ground and floor accelerations for earthquake ground motions BI1, BI4, and BI7.

5.5.2 Displacement Response Spectra Results

The programs used to generate the displacement response spectra are described in detail in Velasquez (2011), with contributions from the author. Three types of nonlinear oscillators with different hysteretic responses are used to compute the inelastic responses: the bilinear, the slack, and the Clough (1966) hysteretic oscillator. The force-displacement relationship for these rules are shown in Figure 5.5 for three different oscillators, each with a constant post-elastic hardening ratio of r = 0.1, a response modification factor of $R_p = 12$, and a damping ratio of $\zeta = 2\%$.

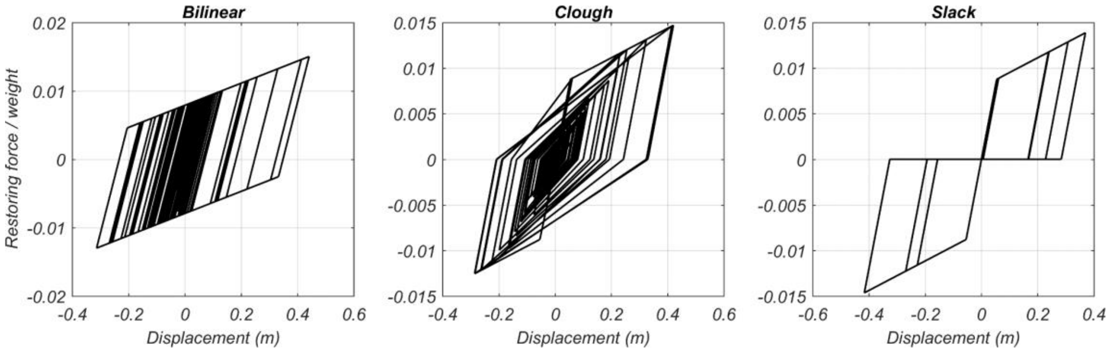

Figure 5.5: Nonlinear oscillators with three different hysteretic responses to BI7 roof acceleration. Post-elastic hardening ratio, r = 0.1, $\zeta = 2\%$ and $R_p = 12$.

Some notable effects of base isolating a building include elongating the predominant period of the building and filtering out some of the high frequency energy generated by an earthquake ground motion. The base isolated building's displacement response is dominated by the first mode; in the period range of interest for nonstructural components and systems, however, the floor displacement response spectra for components, S_{dp}, are dominated by higher modes. Most commonly, nonstructural components have a very low fundamental period, ranging from $T_p = 0.1$s to $T_p = 0.5$s. For this reason, the focus of the results will be on this period range.

Figure 5.6 shows the displacement response spectra for components, S_{dp}, for linear response to the roof acceleration during BI7 from the period ratio $T_p/T_E = 0$ to $T_p/T_E = 0.5$ (with the period range of interest for nonstructural components shaded) for the recorded motion; the response filtered with a steep (1000th order) lowpass FIR filter with a passband frequency of 1 Hz (or a period of 1s and a period ratio equal to 0.32) and a stopband frequency of 1.1 Hz (or a period of 0.91s and a period ratio equal to 0.29); as well as the response filtered with a minimum-order highpass FIR filter with a stopband frequency of 0.9 Hz (or a period of 1.1s and a period ratio equal to 0.35) and a passband frequency of 1 Hz (or a period of 1s and a period ratio equal to 0.32). It is observed from this plot that the displacement response spectra for linear response is dominated by higher modes in the period range of interest for nonstructural components and that the first translational mode controls the spectra beyond $T_p/T_E = 0.35$.

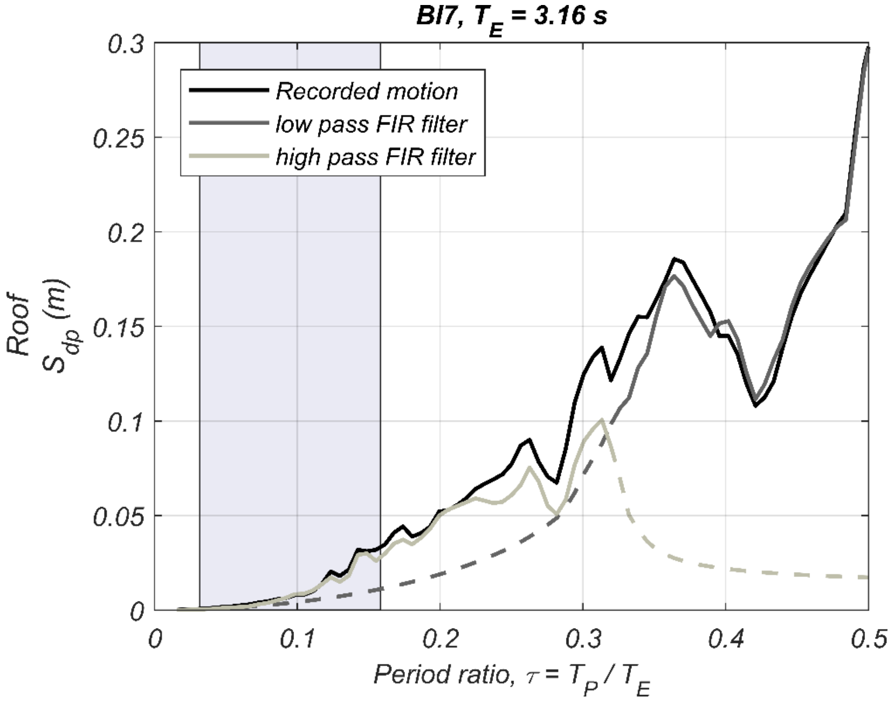

Figure 5.6: Displacement response spectra for linear component response to BI7 roof acceleration: recorded motion, and response filtered with a low pass and high pass filter for $\zeta = 2\%$ with period range of interest shaded.

Figure 5.7 shows the displacement response spectra for elastic response (where $R_p = 1$) and the displacement response spectra for inelastic response determined using component response modification factors $R_p = 1.5$, 3, 6 and 12, for the ground level (input motion below the isolator plane), floor 1, floor 3 and roof for tests BI1, BI4 and BI7 with an elastoplastic oscillator response with a damping ratio of $\zeta = 2\%$. The displacement response spectra for elastic and inelastic responses are plotted against the period ratio of the building for each ground motion. A peak at the period ratio, τ, of around 1 (less than 1 for BI4) is visible in the floor displacement response spectra above the isolator level for $R_p = 1$ and $R_p = 1.5$ (and somewhat visible for $R_p = 3$), indicating a maximum component response for an elastic or nearly elastic response when the component fundamental period, T_p, is equal or close to the predominant period of the building, T_E. The displacement response spectrum with $R_p = 6$ is similar to the displacement response spectrum with $R_p = 12$ (and $R_p \geq 12$, not shown in the plots) for each of the three motions, indicating that the response is saturated for responses with $R_p \geq 6$. The spectral displacement response for the lower R_p values start close to 0 at the shortest period ratios and increase slowly to the peaks near a period ratio of 1. The spectral displacement response with higher R_p values, however, ramp up steeply at a short period ratio and then reach a plateau before intersecting with the spectral displacement response for lower R_p values at a period ratio of around 85% of their peaks, which is a period ratio that will be utilized as an anchor later in the design procedure. As expected from the response of base isolated buildings, the floor displacement response spectra for the component do not appear to differ greatly from the first floor to the roof. For this reason, the chapter hereafter will focus on the results from the roof.

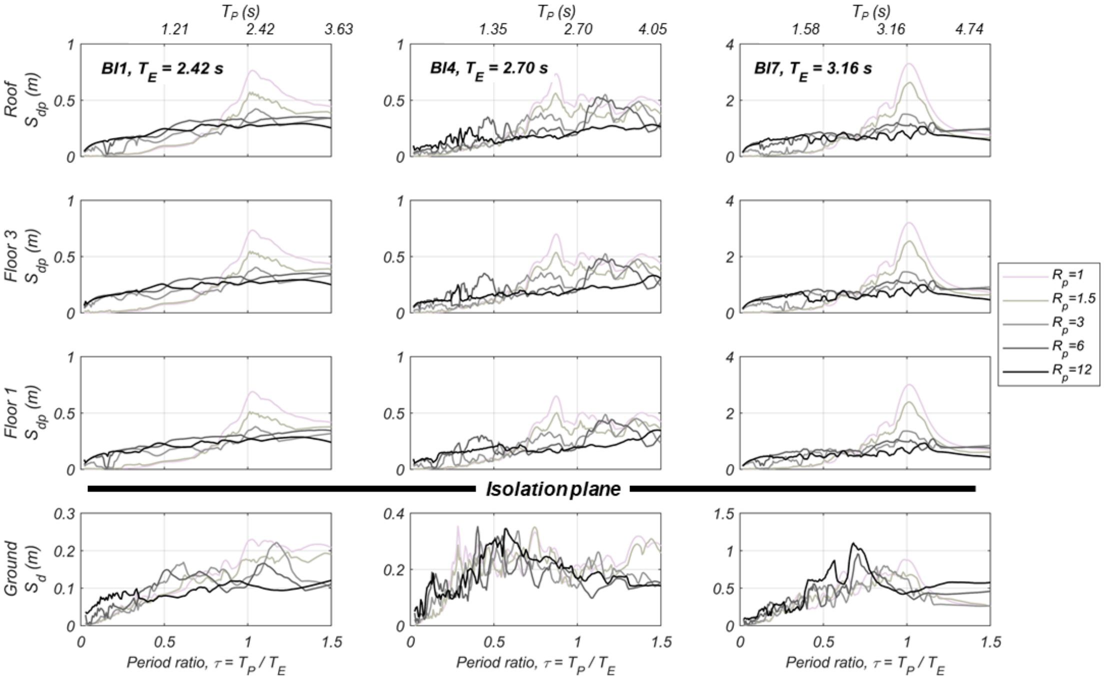

Figure 5.7: Ground level and floor displacement response spectra for a nonlinear oscillator characterized by an elastoplastic hysteretic response using various R_p factors and ζ = 2% for earthquake ground motions BI1, BI4 and BI7.

The roof displacement spectra for elastic response (R_p = 1) and for inelastic response for BI7 with R_p = 1.5, 3, 6 and 12 are plotted in Figure 5.8 for a nonlinear oscillator characterized by a bilinear hysteretic response, a slack hysteretic response, and a Clough hysteretic response with a post-elastic hardening ratio of r = 0, r = 0.05 and r = 0.1 for the first, second, and third columns, respectively. It is evident that the displacement response spectra are dependent on both the hysteretic response type of the oscillator as well as the post-elastic hardening ratio, and that these parameters appear to be coupled with each other as well as with R_p. Apart from the nonlinear oscillator characterized by a slack hysteretic response, the response with a post-elastic hardening ratio of r = 0 is the most critical for all R_p values, especially in the lower period range. It is observed that while there is a slight difference between the oscillator responses with r

= 0.05 and r = 0.1 (and higher r values, not shown in this chapter), it is not as significant as the difference between r = 0 and r = 0.05.

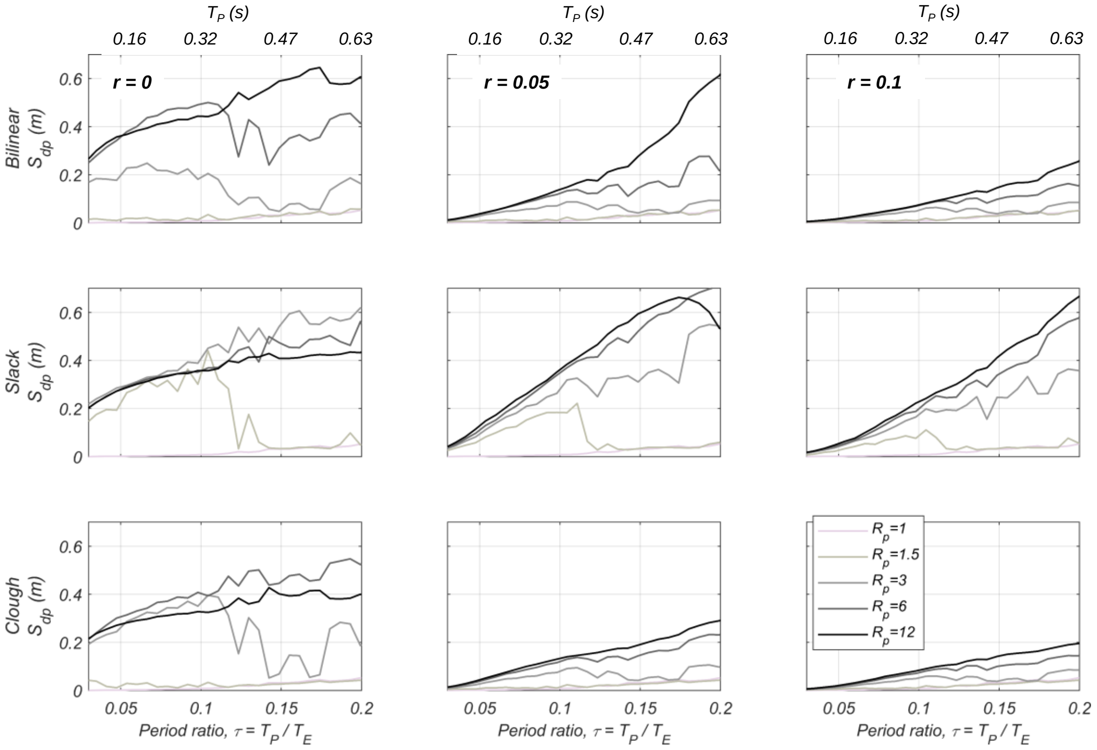

Figure 5.8: BI7 roof displacement response spectra for nonlinear oscillators characterized by a bilinear, slack and Clough hysteretic response with post-elastic hardening ratio r = 0, 0.05 and 0.1, with ζ = 2%.

5.6 Calibration of Estimated Response Spectra

Since the roof displacement response spectra for inelastic component response are highly variable in the period range of interest, calibrating an equation for simplified design is not possible. To simplify the process, the nonlinear oscillator characterized by a bilinear hysteretic response with a post-elastic hardening ratio equal to r = 0 (elastoplastic) is used for calibration, and factors are later introduced to account for different hardening ratios and different hysteretic models. As mentioned in the section above, the displacement response spectra for elastic and inelastic response with the various R_p factors intersect at a period ratio, $\tau = T_P/T_E$, in the range between 0.65 - 0.85

(0.85 will be used for simplicity), see Figure 5.9a. It is interesting that the displacement response spectra for harmonic input (Chopra, 2007) also intersects the displacement response spectra for elastic and inelastic response around this period ratio, which will be used later as an anchor period ratio and an additional boundary condition. The displacement response spectrum for harmonic input is practically insensitive to damping in the period range of interest, which will be further addressed later in this section.

The displacement response for harmonic input is found as the peak floor displacement (in this case the peak roof displacement, $S_{d,roof}$, is used), multiplied by an amplification factor, R_d (Chopra, 2007), where the peak roof displacement can be estimated as the product of the expected displacement of the isolator (peak shear strain multiplied by the total rubber height) and the contribution factor (the product of the modal participation factor and the mode shape for the first mode; a default of 1.1 can be used if this value is unknown). The equation for the amplification factor is reproduced below in equation (5.1), however, since the response in the period range of interest is rather insensitive to damping, the second term in the denominator can be eliminated. Since $T_p \leq 0.85*T_E$ for the cases considered, the terms can be rearranged into the final form of equation (5.1):

$$R_d = \frac{1}{\sqrt{[1-\left(\frac{T_E}{T_P}\right)^2]^2+\cancel{[2*\zeta*\left(\frac{T_E}{T_P}\right)]^2}}} = \frac{1}{\left(\frac{1}{\tau}\right)^2-1} \tag{5.1}$$

At a period ratio of $\tau = 0.85$, this equation gives an amplification factor equal to $R_d = 2.6$. Using this boundary condition, the calibrated equation using the recorded data to estimate the displacement response spectra for components is:

$$S_{dp} = 2.6 * S_{d,roof}\left(\frac{\tau}{0.85}\right)^{\left(\frac{1}{2n}\right)} \tag{5.2}$$

where

$$n = 0.25 + 4\left(1 - \left(\frac{1}{R_P}\right)^{0.3}\right) * \Gamma_r * \Gamma_h \qquad (5.3)$$

and where Γ_r and Γ_h are factors accounting for the post-elastic hardening ratio and the type of hysteretic oscillator, respectively. These factors will be discussed in the following sections. Using default values of $\Gamma_r = 1$ and $\Gamma_h = 1$ corresponding to an oscillator characterized by an elastoplastic hysteretic response, the curves in Figure 5.9b are generated for a range of R$_P$ values. The short and moderately short period ranges defined later in the design procedure are shaded in this plot.

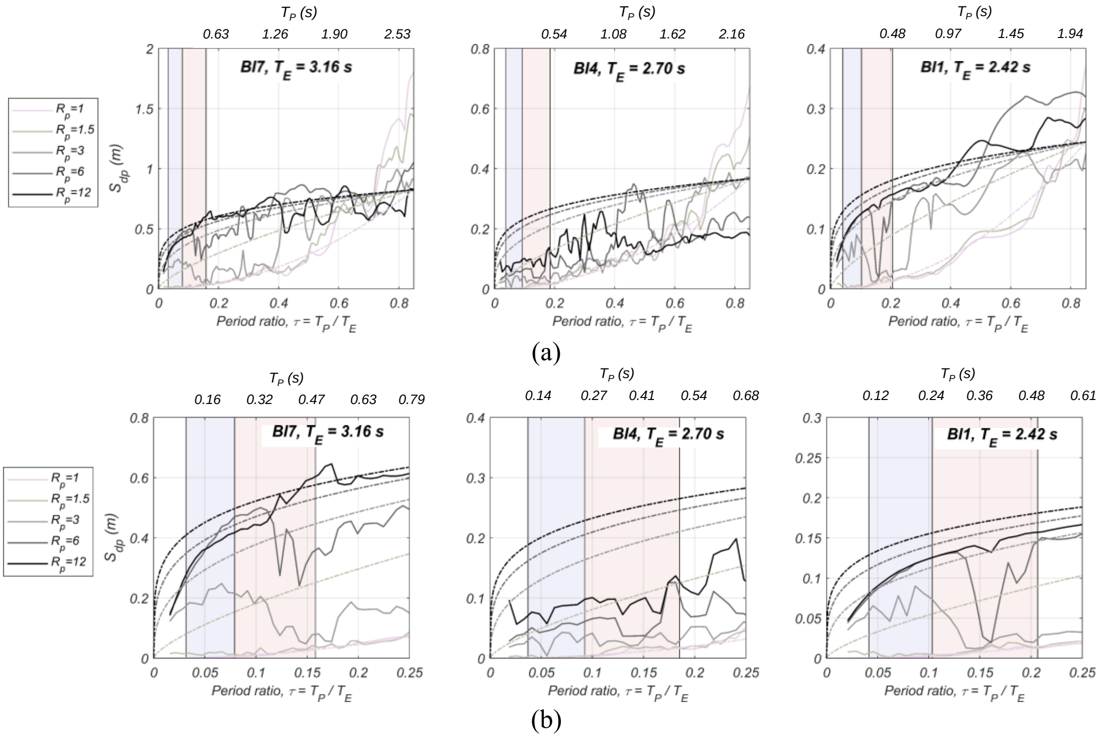

(a)

(b)

Figure 5.9: Roof displacement response spectra for elastic and inelastic component response and predicted curves (a) for a period ratio range up to 0.85 and (b) for a period ratio range up to 0.25 (with the period range of interest shaded) for ζ = 2%.

The post-elastic hardening ratio factor, Γ_r, and hysteretic factor, Γ_h, are obtained using the data from the recorded roof accelerations from BI7. The hysteretic factor, Γ_h, is calibrated by obtaining the ratio of the spectral displacements of a nonlinear oscillator characterized by a Clough hysteretic response to the spectral displacements of a nonlinear oscillator characterized by a bilinear hysteretic response, averaged over 0.1s T_p intervals and for a damping ratio of $\zeta = 2\%$. This obtained for a range of R_p factors from 1 to 12, post-elastic hardening ratios of $r = 0$, 0.05 and 0.1 (Figure 5.10a) and then repeated for the ratio of the spectral displacements of a nonlinear oscillator characterized by a slack hysteretic response to the spectral displacements of a nonlinear oscillator characterized by a bilinear hysteretic response (Figure 5.10b). The bold line at $\Gamma_h = 1$ in the plots represents the nonlinear oscillator characterized by a bilinear hysteretic response. Some values of R_p are not shown because they were much different than the points with higher R_p values. Overall, the results for the nonlinear oscillator characterized by a Clough hysteretic response are close to one, meaning that the response does not differ greatly from the response of the nonlinear oscillator characterized by a bilinear hysteretic response. The results for the nonlinear oscillator characterized by a slack hysteretic response are generally greater than one, meaning that the spectral displacements for this oscillator are higher than for the nonlinear oscillator characterized by a bilinear response. The Γ_h results for the nonlinear oscillators with Clough and slack hysteretic responses averaged over the period intervals are tabulated in Table 5.1. For design purposes, a factor of $\Gamma_h = 1$ would be used as a default value unless further information about the component's hysteretic response is known. Using the analyzed data, a factor of $\Gamma_h = 2.5$ could be proposed for use with components that have a high hysteretic energy dissipation characteristic (i.e. the oscillator characterized by a slack hysteretic response) and $\Gamma_h = 1$ for components with average or low hysteretic energy dissipation characteristics (i.e. the oscillators characterized by a bilinear or Clough hysteretic response).

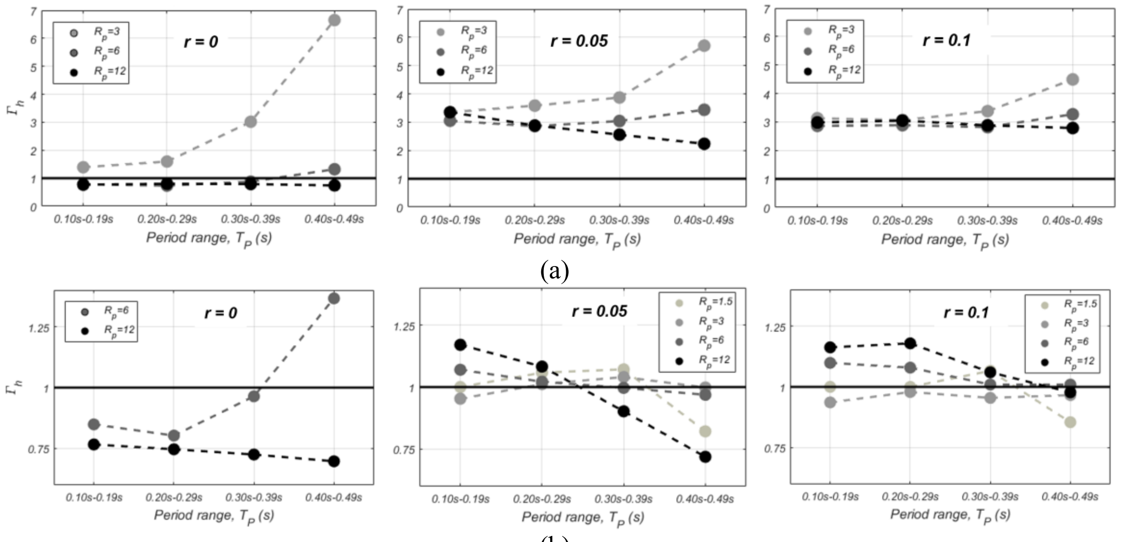

(a)

(b)

Figure 5.10: Hysteretic factor Γ_h: ratio of spectral displacement for a nonlinear oscillator with (a) Clough hysteretic response or (b) slack hysteretic response to spectral displacement for a nonlinear oscillator with a bilinear hysteretic response for post-elastic hardening ratios of r = 0, 0.05 and 0.1 and ζ = 2%.

Table 5.1: Average Γ_h.

Nonlinear oscillator - Clough hysteretic response				
Post-elastic hardening ratio, r	Average Γ_h $R_p = 12$	Average Γ_h $R_p = 6$	Average Γ_h $R_p = 3$	Average Γ_h $R_p = 1.5$
0	0.73	1.0	1.8	1.2
0.05	0.97	1.0	1.0	0.99
0.10	1.1	1.1	0.96	0.98
0.20	1.1	1.1	0.96	0.99
Average	0.98	1.0	1.2	1.0

Nonlinear oscillator - slack hysteretic response				
Post-elastic hardening ratio, r	Average Γ_h $R_p = 12$	Average Γ_h $R_p = 6$	Average Γ_h $R_p = 3$	Average Γ_h $R_p = 1.5$
0	0.78	0.93	3.2	13.0
0.05	2.8	3.1	4.1	7.9
0.10	2.9	3.0	3.5	4.4
0.20	2.2	2.1	2.1	2.0
Average	2.2	2.3	3.2	6.8

The post-elastic hardening ratio factor, Γ_r, is obtained by taking the ratio of the inelastic spectral displacements of a nonlinear oscillator for a range of post-elastic hardening ratios to the spectral displacements of a nonlinear oscillator with a hardening ratio of r = 0 for T_p values ranging from T_p = 0.07s - 0.5s. It is noted that spectral displacements below 100mm are not used for this calibration. The ratios were found for R_p = 3, 6 and 12 for the nonlinear oscillator characterized by bilinear, slack and Clough hysteretic responses using a damping ratio of 2%, shown in Figure 5.11a, b, and c, respectively. For each post-elastic hardening ratio considered, the median and 85th percentile values are calculated and indicated on the plot with a '+' and an 'x', respectively. It is observed that this factor is coupled with the R_p value as well as the type of the hysteretic oscillator. Using the median values for each hysteretic model and the boundary conditions that at r = 0, $\Gamma_r = 1$, and at r = 1, $\Gamma_r = 0$, a curve is calibrated for each R_p value considered. The equation takes the form:

$$\Gamma_r = [1 - r^k]^{\left(1/(m*k)\right)} \tag{5.4}$$

where k and m are factors that depend on the hysteretic model as well as R_p, and are tabulated in Table 5.2. The curves using equation (5.4) are plotted with dashed lines along with the ratios in Figure 5.11. For design purposes, a default factor of $\Gamma_r = 1$ could be used unless further information about the post-elastic hardening ratio, r, of the hysteretic response is known. Using the data analyzed from this case study, the results can be simplified such that $\Gamma_r = 1$ if r < 0.1 and $\Gamma_r = 0.5$ if r ≥ 0.1 for components characterized by high hysteretic energy dissipation (i.e. the nonlinear oscillator characterized by a slack hysteretic response). For components characterized by average or low hysteretic energy dissipation (i.e. nonlinear oscillator characterized by a bilinear or Clough hysteretic response), $\Gamma_r = 1$ if $r < 0.025$ and $\Gamma_r = 0.5$ if $r \geq 0.025$. For the next section, default values of $\Gamma_h = 1$ and $\Gamma_r = 1$ will be used in the calibrated results, and additional equations will be presented in Appendix C for alternative Γ_h and Γ_r factors.

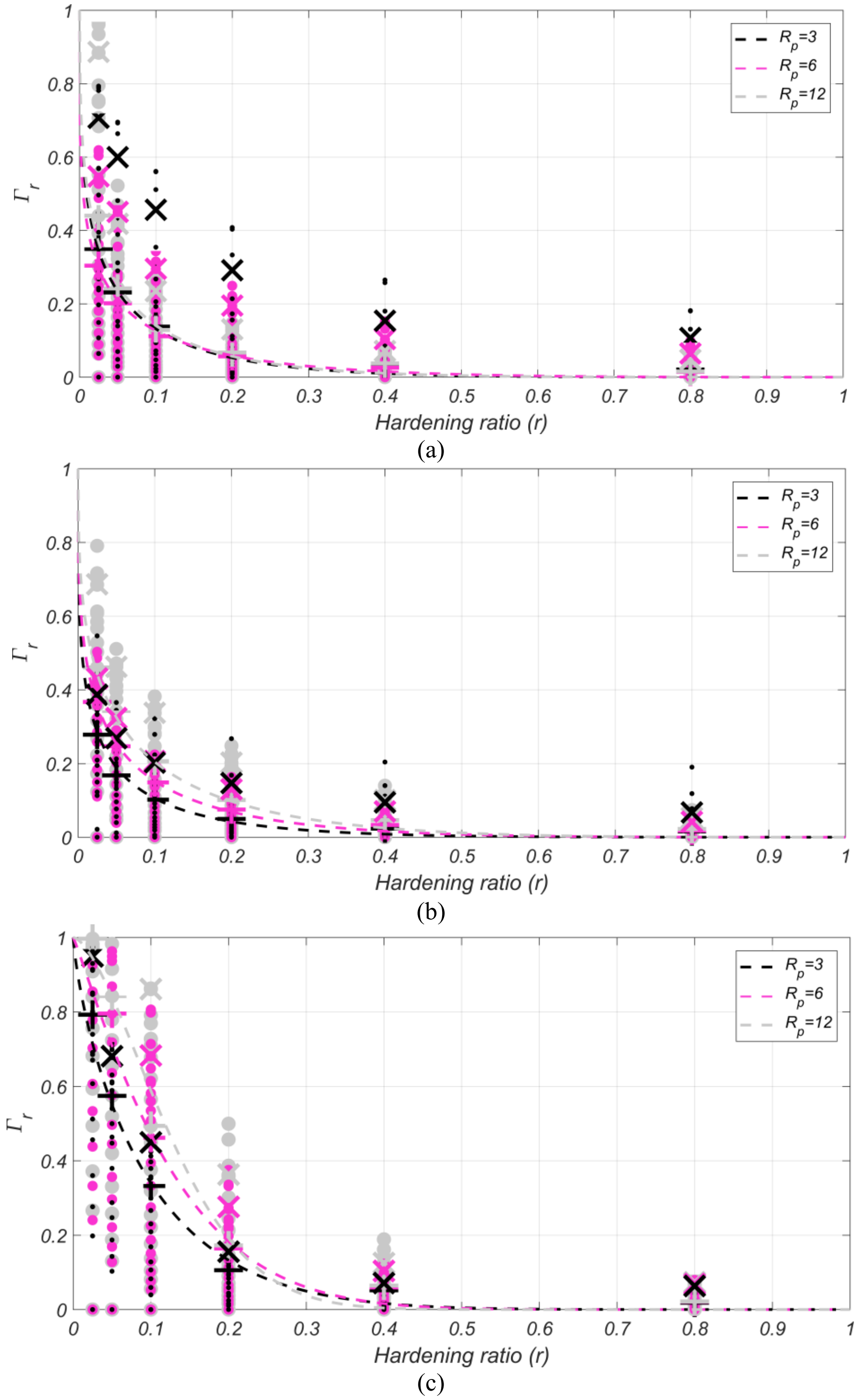

(a)

(b)

(c)

Figure 5.11: Hardening ratio factor Γ_r for T_p=0.07s-0.5s and ζ=2%: ratio of spectral displacement for oscillator with (a) bilinear, (b) Clough and (c) slack hysteretic response for a range of r to spectral displacement with hardening ratio r=0. Median and 85th percentile values denoted with a + and an x, respectively.

Table 5.2: Coefficients for Γ_r equation.

Nonlinear oscillator (bilinear)		
R_p	k	m
3	0.38	0.7
6	0.29	1.2
12	0.4	0.65

Nonlinear oscillator (Clough)		
R_p	k	m
3	0.33	0.85
6	0.35	0.9
12	0.4	0.8

Nonlinear oscillator (slack)		
R_p	k	m
3	0.8	0.2
6	1.1	0.1
12	1.6	0.03

5.7 Design Procedure Calibrated for Seismic Isolation with High Damping Rubber Bearings

A set of simplified design equations is proposed for the case study investigated based on the equations calibrated for seismic isolation with high damping rubber bearings. A design strategy used is to not consider a continuum of periods of the component, but to instead create bins, since the T_P value is not always readily available. For example, a bin with $T_P = 0.25$s for short periods where $0 \leq T_P \leq 0.25$s, and with $T_P = 0.5$s (which can be used as the default T_P) for moderately short periods where $0.25\text{s} < T_P \leq 0.5$s. These bins are not specific to the isolation system used. Using the appropriate T_P (0.25s or 0.5s) for a given nonstructural component, and T_E (for a specific hazard level) for the building-isolation system, the period ratio, $\tau = T_P/T_E$, can be determined.

Using the calibrated results from the case study described in this chapter, a response modification factor for the nonstructural component, R_P, can be determined using a bilinear estimation:

$$R_p = 2.5(C_p^{*}) + 1 \qquad if\ C_p^{*} \leq 0.8 \qquad (5.5a)$$

$$R_p = 45(C_p^{*}) - 33 \qquad if\ C_p^{*} > 0.8 \qquad (5.5b)$$

where

$$C_p{}^* = \frac{\left(\frac{\Delta_{p,ls}}{3.6 * S_{d,roof} * \tau^2}\right) - 1}{0.75\left(\frac{1}{\tau}\right)^{1.8} - 1} \tag{5.6}$$

and where $\Delta_{p,ls}$ is the displacement limit state, τ is the period ratio T_p/T_E, and $S_{d,roof}$ is the peak roof displacement. Alternatively, R_p can be defined using a power function estimation as:

$$R_p = 9(C_p{}^*)^{11} + 2C_p{}^* + 1 \tag{5.7}$$

where $R_{p,min} = 3$ for all R_p equations (equations 5 and 7) if the component is sitting on the floor, since some of the gravitational force (a friction coefficient of 1/3 has been conservatively chosen) can be relied upon to aid in energy dissipation as a Coulomb damper. Using the R_p value from either equation (5.5) or (5.7), the design force for the nonstructural component is then defined as:

$$F_p = \frac{1}{R_p}\left(\frac{2\pi}{T_E}\right)^2 \frac{S_{d,roof}}{g}(W_p) \tag{5.8}$$

where g is the gravitational constant in the same units as $S_{d,roof}$, W_p is the operating weight of the nonstructural component, and T_E is the effective period of the building-isolation system. Using these equations, a design example is shown in Appendix D.

5.8 Conclusions

Base isolation is often chosen for building designs to not only protect the structure but also to protect the nonstructural components from seismic damage, however, currently there are no code provisions specifically for designing nonstructural components within a base isolated building. This chapter describes a framework for designing nonstructural components for use in a base isolated building. Starting with an allowable displacement for the nonstructural component, and then defining key parameters of the building-isolation system and the nonstructural component, a critical design force can be calculated for the seismic hazards considered. A case study, using experimental data for the structural response in conjunction with simulated data from inelastic floor displacement response spectra for the nonstructural response, is utilized to describe the design process and present the calibrated equations.

5.9 Acknowledgements

The work in this chapter has been prepared to be submitted for publication as Chen, M., Restrepo, J. I., and Blandon, C. Seismic design framework for inertia-sensitive nonstructural components in base isolated buildings.

5.10 Appendix C – Alternative Design Equations

Alternative design equations using calibrated results are presented in this Appendix for combinations of different Γ_h and Γ_r factors. Equations 5.5a, 5.5b, 5.6 and 5.7 are rewritten in general terms, with variables corresponding to different combinations of Γ_h and Γ_r factors, listed in the Table below, where case 2 corresponds to the default case used in the body of the chapter.

Generic equations:

$$R_p = \boldsymbol{a}({C_p}^*) + 1 \qquad if\ {C_p}^* \le \boldsymbol{d} \tag{5.5a}$$

$$R_p = \boldsymbol{b}({C_p}^*) - \boldsymbol{c} \qquad if\ {C_p}^* > \boldsymbol{d} \tag{5.5b}$$

where

$$C_p{}^* = \frac{\left(\frac{\Delta_{p,ls}}{3.6 * S_{d,roof} * \tau^2}\right) - 1}{\boldsymbol{j}\left(\frac{1}{\tau}\right)^{\boldsymbol{k}} - 1} \tag{5.6}$$

$$R_p = \boldsymbol{m}(C_p{}^*)^{\boldsymbol{n}} + (11 - \boldsymbol{m})C_p{}^* + 1 \tag{5.7}$$

Table 5.3: Factors for use in equations 5.5-5.7 for alternative cases where case 2 corresponds to the default case.

Case	Γ_r	Γ_h	a	b	c	d	j	k	m	n
1	0.5	1	3.75	40	28	0.8	0.77	1.6	9	6
2	1	1	2.5	45	33	0.8	0.75	1.8	9	11
3	0.5	2.5	2.5	45	33	0.8	0.75	1.8	9	11
4	1	2.5	2.2	90	78	0.9	0.73	1.9	9	22

Equations 5.5-5.7 are shown below with appropriate variables for each case in the next section. The plots used for calibration are also shown for each case for a range of period ratios (plotted in grey) corresponding to building periods, T_E, between 2s and 4s.

Case 1:

$$R_p = 3.75(C_p{}^*) + 1 \qquad if\ C_p{}^* \leq 0.8 \tag{5.5a}$$

$$R_p = 40(C_p{}^*) - 28 \qquad if\ C_p{}^* > 0.8 \tag{5.5b}$$

where

$$C_p{}^* = \frac{\left(\frac{\Delta_{p,ls}}{3.6 * S_{d,roof} * \tau^2}\right) - 1}{0.77\left(\frac{1}{\tau}\right)^{1.6} - 1} \tag{5.6}$$

$$R_p = 9(C_p{}^*)^6 + 2C_p{}^* + 1 \tag{5.7}$$

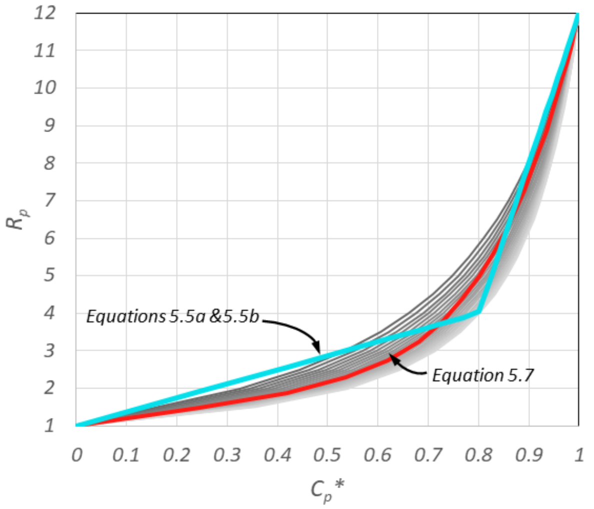

Figure 5.12: Curves used for calibration of equations 5.5 and 5.7 for case 1.

Case 2:

$$R_p = 2.5(C_p{}^*) + 1 \qquad if\ C_p{}^* \leq 0.8 \qquad (5.5a)$$

$$R_p = 45(C_p{}^*) - 33 \qquad if\ C_p{}^* > 0.8 \qquad (5.5b)$$

where

$$C_p{}^* = \frac{\left(\frac{\Delta_{p,ls}}{3.6 * S_{d,roof} * \tau^2}\right) - 1}{0.75\left(\frac{1}{\tau}\right)^{1.8} - 1} \qquad (5.6)$$

$$R_p = 9(C_p{}^*)^{11} + 2C_p{}^* + 1 \qquad (5.7)$$

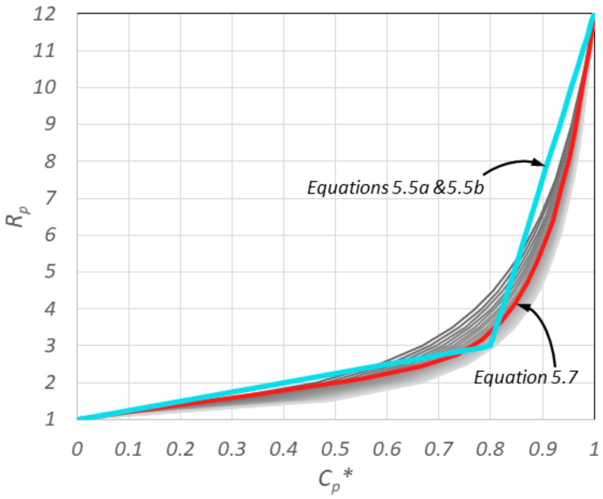

Figure 5.13: Curves used for calibration of equations 5.5 and 5.7 for case 2 (default case).

Case 3:

$$R_p = 2.5(C_p{}^*) + 1 \qquad if\ C_p{}^* \leq 0.8 \qquad (5.5a)$$

$$R_p = 45(C_p{}^*) - 33 \qquad if\ C_p{}^* > 0.8 \qquad (5.5b)$$

where

$$C_p{}^* = \frac{\left(\frac{\Delta_{p,ls}}{3.6 * S_{d,roof} * \tau^2}\right) - 1}{0.75\left(\frac{1}{\tau}\right)^{1.8} - 1} \qquad (5.6)$$

$$R_p = 9(C_p{}^*)^{11} + 2C_p{}^* + 1 \qquad (5.7)$$

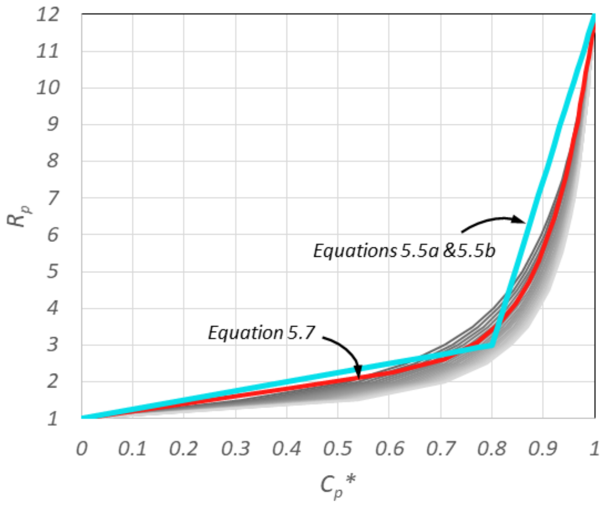

Figure 5.14: Curves used for calibration of equations 5.5 and 5.7 for case 3.

Case 4:

$$R_p = 2.2(C_p{}^*) + 1 \qquad if\ C_p{}^* \leq 0.9 \qquad (5.5a)$$

$$R_p = 90(C_p{}^*) - 78 \qquad if\ C_p{}^* > 0.9 \qquad (5.5b)$$

where

$$C_p{}^* = \frac{\left(\frac{\Delta_{p,ls}}{3.6 * S_{d,roof} * \tau^2}\right) - 1}{0.73\left(\frac{1}{\tau}\right)^{1.9} - 1} \qquad (5.6)$$

$$R_p = 9(C_p{}^*)^{22} + 2C_p{}^* + 1 \tag{5.7}$$

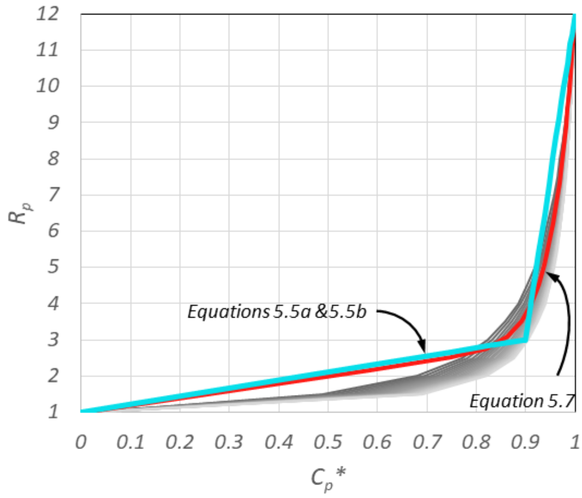

Figure 5.15: Curves used for calibration of equations 5.5 and 5.7 for case 4.

5.11 Appendix D – Design Example

5.11.1 Design Example of a Hanging Projector from Top Floor Ceiling for a Life Safety Seismic Hazard Level

Given information for building - isolation system:

- Base isolation type: high damping rubber bearings
- Building system effective period (for life safety hazard level), $T_E = 3.16$ s
- Peak roof displacement (for life safety hazard level), $S_{d,roof} = 0.34$ m

Given information for nonstructural component:

- Damage limit (for life safety hazard level), $\Delta_{p,ls} = 0.025$ m
- Component period, T_p range = short (0.25 s)

- Hysteretic energy dissipation capabilities: low; Γ_h = 1.0 (default)
- Hardening ratio, r = 0.02; Γ_r = 1.0 (default)
- Connection: hanging from ceiling = other (not sitting on ground, therefore no minimum R_p value)

Calculations to find component design force (for life safety hazard level):

Using the given information to find the period ratio:

$$\tau = T_p/T_E = 0.25\text{ s} / 3.16\text{ s} = 0.08$$

equation (5.6):

$$C_p{}^* = \frac{\left(\frac{\Delta_{\mathrm{p,ls}}}{3.6 * S_{d,roof} * \tau^2}\right) - 1}{0.75\left(\frac{1}{\tau}\right)^{1.8} - 1} = \frac{\left(\frac{0.025\ m}{3.6 * 0.34\ m * 0.08^2}\right) - 1}{0.75\left(\frac{1}{0.08}\right)^{1.8} - 1} = 0.032 \leq 0.8$$

equation (5.5a):

$$R_p = 2.5\ (C_p{}^*) + 1 = 2.5(0.032) + 1 = 1.08$$

equation (5.8):

$$F_p = \frac{1}{R_p}\left(\frac{2\pi}{T_E}\right)^2 \frac{S_{d,roof}}{g}\left(W_p\right) = \frac{1}{1.08}\ \left(\frac{2\pi}{3.16s}\right)^2 \frac{0.34\ m}{9.81\ m/s^2}\left(W_p\right) = 0.13(W_p)$$

5.12 References

Ahmadi, G. & Su, L. (1992). Equipment response spectra for base-isolated shear beam structures. *Nuclear engineering and design, 132*(3), 287-308.

ASCE/SEI. (2010). Minimum design loads for buildings and other structures. *SEI/ASCE 7-10, American Society of Civil Engineers*, Reston, VA.

ASCE/SEI. (2016). Minimum design loads for buildings and other structures. *SEI/ASCE 7-16, American Society of Civil Engineers*, Reston, VA.

Astroza, R., Ebrahimian, H., Conte, J. P., Restrepo, J. I., & Hutchinson, T. C. (2016). System identification of a full-scale five-story reinforced concrete building tested on the NEES-UCSD shake table. *Structural Control and Health Monitoring, 23*(3), 535-559.

Baird, A., Tasligedik, A. S., Palermo, A., & Pampanin, S. (2014). Seismic performance of vertical nonstructural components in the 22 February 2011 Christchurch earthquake. *Earthquake Spectra, 30*(1), 401-425.

Chen, M., Pantoli, E., Astroza, R., Ebrahimian, H., Mintz, S., Wang, X., Hutchinson, T., Conte, J., Restrepo, J., Meacham, B., Kim, J., & Park, H. (2013). BNCS report #1: full-scale structural and nonstructural building system performance during earthquakes and post-earthquake fire - specimen design, construction and test protocol. *Structural Systems Research Project Report Series, SSRP 13/9*. University of California, San Diego, La Jolla, CA.

Chen, M., Pantoli, E., Wang, X., Astroza, R., Ebrahimian, H., Hutchinson, T., Conte, J., Restrepo, J., Marin, C., Walsh, K., Bachman, R., Hoehler, M., Englekirk, R., & Faghihi, M. (2016). Full-scale structural and nonstructural building system performance during earthquakes: part I – specimen description, test protocol and structural response. *Earthquake Spectra, 32*(2), 737-770.

Chen, M., Astroza, R., Restrepo, J. I., Conte, J. P., Hutchinson, T., & Bock, Y. (2017). Predominant period and equivalent viscous damping ratio identification for a full-scale building shake table test. *Earthquake Engineering and Structural Dynamics, 46*(14), 2459-2477.

Chopra, A.K. (2007). Dynamics of Structures: Theory and Applications to Earthquake Engineering, 3rd Edition, Prentice Hall, Englewood Cliffs, New Jersey.

Clough, R. W. (1966). Effect of stiffness degradation on earthquake ductility requirements. *Rept. No. SEMM 66-16, University of California, Berkeley*, Berkeley, California.

Eurocode 8 (2003). Design of structures for earthquake resistance – part I: general rules, seismic actions and rules for buildings. Brussels.

Fan, F. G. & Ahmadi, G. (1990). Floor response spectra for base-isolated multi-storey structures. *Earthquake engineering and structural dynamics, 19*(3), 377-388.

Fan, F. G. & Ahmadi, G. (1992). Seismic responses of secondary systems in base-isolated structures. *Engineering Structures*, *14*(1), 35-48.

Federal Emergency Management Agency (FEMA 274) (1997). NEHRP commentary on the guidelines for the seismic rehabilitation of buildings. *Prepared by the Applied Technology Council for the Federal Emergency Management Agency*, Washington, D.C.

Federal Emergency Management Agency (FEMA 74-FM) (2005). Earthquake hazard mitigation for nonstructural elements. *Prepared by WJE Associates as a* *subcontractor to URS Corp. for the Federal Emergency Management Agency,* Washington, D.C.

Federal Emergency Management Agency (FEMA E-74) (2012). Reducing the risks of nonstructural earthquake damage: a practical guide, Fourth Edition. *Prepared by the Applied Technology Council for the Federal Emergency Management Agency,* Washington, D.C.

Hernried, A. G., & Lei, K. M. (1993). Parametric studies on the response of equipment in resilient-friction base isolated structures subjected to ground motion.*Engineering Structures, 15*(5), 349-357.

Hernried, A. G., & Lei, K. M. (1995). Semi-analytical techniques for the determination of the dynamic response of equipment in structures supported on coulomb friction elements. *Earthquake engineering and structural dynamics, 24*(6), 801-810.

Huang, Y. N., Whittaker, A. S., & Luco, N. (2010). Seismic performance assessment of base-isolated safety-related nuclear structures. *Earthquake Engineering and Structural Dynamics, 39*(13), 1421-1442.

Hutchinson, T., Hoehler, M., Gastelum, A., Watkins, D., & Wood, R. (2010). Observations from the Sierra El Mayor earthquake (Northern Baja California Earthquake), EERI: Report on Nonstructural Damage, Baja California Earthquake, Magnitude 7.2 on April 4, 2010.

Inaudi, J. A., & Kelly, J. M. (1993). Optimum damping in linear isolation systems. *Earthquake engineering and structural dynamics, 22*(7), 583-598.

Isaković, T., Zevnik, J., & Fischinger, M. (2011). Floor response spectra in isolated structures subjected to earthquakes weaker than the design earthquake—Part I: Isolation with high-damping rubber bearings. *Structural Control and Health Monitoring, 18*(6), 635-659.

Juhn, G., Manolis, G. D., Constantinou, M. C., & Reinhorn, A. M. (1992). Experimental study of secondary systems in base-isolated structure. *Journal of Structural Engineering, 118*(8), 2204-2221.

Kelly, J. M. (1999). The role of damping in seismic isolation. *Earthquake engineering and structural dynamics, 28*(1), 3-20.

Kelly, J. M., & Tsai, H. C. (1985). Seismic response of light internal equipment in base-isolated structures. *Earthquake Engineering and Structural Dynamics, 13*(6), 711-732.

Kelly, J. M., & Marsico, M. R. (2015). The influence of damping on floor spectra in seismic isolated nuclear structures. *Structural Control and Health Monitoring, 22*(4), 743-756.

Miranda, E., Mosqueda, G., Retamales, R., & Pekcan, G. (2012). Performance of nonstructural components during the 27 February 2010 Chile earthquake. *Earthquake Spectra 28*(S1), S453–S471.

Politopoulos, I. (2008). A review of adverse effects of damping in seismic isolation. *Earthquake Engineering and Structural Dynamics, 37*(3), 447-465.

Politopoulos, I., & Pham, H. K. (2011). Floor spectra of mixed base isolated structures. *Bulletin of Earthquake Engineering, 9*(4), 1115-1135.

Sackman, J. L. & Kelly, J. M. (1979). Seismic analysis of internal equipment and components in structures. *Engineering Structures, 1*(4), 179-190.

Sackman, J. L. & Kelly, J. M. (1980). Equipment response spectra for nuclear power plant systems. *Nuclear Engineering and Design*, *57*(2), 277-294.

Skinner, R. I., Robinson, W. H., & McVerry, G. H. (1993). An introduction to seismic isolation. John Wiley & Sons.

Tsai, H. C. & Kelly, J. M. (1988). Non-classical damping in dynamic analysis of base-isolated structures with internal equipment. *Earthquake Engineering and Structural Dynamics, 16*(1), 29-43.

Tsai, H. C. & Kelly, J. M. (1989). Seismic response of the superstructure and attached equipment in a base-isolated building. *Earthquake Engineering and Structural Dynamics, 18*(4), 551-564.

Van den Einde, L., Restrepo, J. I., Conte, J. P., Luco, E., Seible, F., Filiatrault, A., Clark, A., Johnson, A., Gram, Marty, Kusner, D., & Thoen, B. (2004). Development of the George E. Brown Jr. network for earthquake engineering simulation (NEES) large high performance outdoor shake table at the University of California, San Diego. *Proceedings, 13th World Conference on Earthquake Engineering*.

Van Engelen, N. C., Konstantinidis, D., & Tait, M. J. (2014). Seismic performance of attached equipment in a base isolated building. *Proceedings, tenth U.S. National Conference on Earthquake Engineering, Anchorage, Alaska.*

Velasquez Bedoya, J. F. (2011). Floor response spectra for the design of acceleration-sensitive light nonstructural systems in buildings, (Master's thesis).

Wolff, E. D., & Constantinou, M. C. (2004). Experimental study of seismic isolation systems with emphasis on secondary system response and verification of accuracy of dynamic response history analysis methods. *MCEER-04-0001,* Buffalo, New York.

Yang, T. Y., Konstantinidis, D., & Kelly, J. M. (2010). The influence of isolator hysteresis on equipment performance in seismic isolated buildings. *Earthquake Spectra, 26*(1), 275-293.